Metallic Nanoparticles: Analytical Properties of the Acoustic Vibrations and Applications

by

Jian Wu
B.Eng., Wuhan University, 2010
M.A.Sc., University of Chinese Academy of Sciences, 2013

A Dissertation Submitted in Partial Fulfillment
of the Requirements for the Degree of

DOCTOR OF PHILOSOPHY

in the Department of Electrical and Computer Engineering

University of Victoria

Supervisory Committee

Metallic Nanoparticles: Analytical Properties of the Acoustic Vibrations and Applications

by

Jian Wu
B.Eng., Wuhan University, 2010
M.A.Sc., University of Chinese Academy of Sciences, 2013

Supervisory Committee

Dr. Reuven Gordon, (Department of Electrical and Computer Engineering)
Supervisor

Dr. Tao Lu, (Department of Electrical and Computer Engineering)
Departmental Member

Dr. Fraser Hof, (Department of Chemistry)
Outside Member

Abstract

Supervisory Committee

Dr. Reuven Gordon, (Department of Electrical and Computer Engineering)

Supervisor

Dr. Tao Lu, (Department of Electrical and Computer Engineering)

Departmental Member

Dr. Fraser Hof, (Department of Chemistry)

Outside Member

This thesis focuses on the analytical properties of the acoustic vibrations and applications of metallic nanoparticles. With regard to the analytical properties of the acoustic vibrations, we focus on nanoparticle acoustic resonance enhanced four-wave mixing (FWM) as an in situ characterization technique for characterizing nanoparticles' shape, size, and size distribution. The nonlinear optical response of metallic nanoparticles is resonantly driven by the electrostriction force which couples to the acoustic vibrations of nanoparticles. Information about nanoparticles' shape, size, and size distribution can be obtained by analyzing the resonant peak position and linewidth in the FWM signal which carries the information about the vibrational modes. We characterize different nanoparticle solutions of different materials, shapes, and sizes using this FWM technique. Information obtained from the FWM characterization agrees well with the scanning electron microscopic examination, indicating the FWM technique can serve as an in situ nanoparticle characterization tool. We also demonstrate the FWM technique can be used for monitoring nanoparticle growth in situ.

With regard to the applications of metallic nanoparticles, we focus on quantification of an exogenous cancer biomarker Acetyl Amantadine using surface-enhanced Raman scattering (SERS). Raman spectroscopy can provide unique fingerprint information of molecules, which can be used as a chemical detection and identification technique. The intrinsically weak Raman signal caused by the small scattering cross section presents a barrier for trace chemical detection. Localized surface plasmon resonance of metallic nanoparticles can provide large local field enhancement, which can be utilized to enhance the intrinsically weak Raman signal. In order to achieve higher local field enhancement, we focus on using the gap structures formed between nanoparticles instead of using discrete nanoparticles. Molecules should locate within the hot spots of the gap structures to experience the largest enhancement. This requires that molecules should be extracted from volume onto the metallic surface. Based on these guidelines, two SERS platforms are designed using gold nanoparticles (nanorods and nanospheres) combined with different surface functionalization techniques. The performance of these two platforms are characterized by investigating the sensitivity and limit of detection (LOD). 16 ng/mL and 0.4 ng/mL LODs are achieved for nanorod and nanosphere platforms, respectively.

Table of Contents

List of Tables

List of Figures

Acknowledgements

I would like to express my great gratitude to my supervisor, Dr. Reuven Gordon, for his meticulous supervision on my PhD projects, his generosity of supporting my research, and his inspirational leadership, aptitude, and enthusiasm for scientific research.

I would like to thank the other dissertation committee members, Dr. Tao Lu, Dr. Fraser Hof, as well as the outside examiner, for providing valuable comments and suggestions for improving my dissertation.

I would like to thank all my colleges I have been working with in the nano-plasmonics research lab for providing insightful discussion and assistance on my research work.

I also would like to thank Dr. Elaine Humphrey for helping me in nanofabrication and nanoimaging.

To my parents, I am very much grateful for their unconditional love and support all along.

Dedication

To my parents,

and

everyone offered the help

along the way.

Glossary

List of symbols:

$\mathbf{E_0}$	electric field
Φ	electric potential
P_l	Legendre Polynomials of order l
Φ_{in}	potential inside the sphere
Φ_{out}	potential outside the sphere
$\mathbf{p}$	dipole moment
α	polarizability
k	wave vector
σ_{abs}	absorption cross section
σ_{scatt}	scattering cross section
σ_{ext}	extinction cross section
Γ	homogeneous linewidth
T_2	dephasing time
γ_{b}	bulk damping
Γ_{rad}	radiation damping
$\Gamma_{\mathrm{interface}}$	damping due to electron surface scattering
h	Plank constant
κ_{rad}	radiation damping constant
V	nanoparticle volume
S_{A}	surface scattering constant
v_{F}	Fermi velocity
L_{eff}	effective path length of the electrons
$\upsilon_{\mathrm{ext,r}}$	nanorod extensional mode frequency
$\upsilon_{\mathrm{br,r}}$	nanorod breathing mode frequency
E	Young's modulus
ρ	density of gold
v_l	longitudinal sound velocity in gold
$\upsilon_{\mathrm{ext,s}}$	nanosphere extensional mode frequency
$\upsilon_{\mathrm{br,s}}$	nanosphere breathing mode frequency
$\upsilon_{\mathrm{prism}}$	nanoprism vibrational frequency
$V_{l,silver}$	longitudinal speed of sound in silver
L_{prism}	edge length of nanoprisms
$\upsilon_{\mathrm{octahedro}}$	nano-octahedron vibrational frequency
$L_{octahedr}$	edge length of nano-octahedrons
I_{Raman}	Raman intensity
C_{AcAm}	AcAm concentration

Abbreviations:

CW	continuous-wave
FWM	four-wave mixing
SERS	surface-enhanced Raman scattering
AcAm	Acetyl Amantadine
SSAT	Spermidine/Spermine N1 Acetyl-transferase
LCMS	liquid chromatography with tandem mass spectrometery
LSPR	localized surface plasmon resonance
LOD	limit of detection
SPP	surface plasmon polariton
LSP	localized surface plasmon
UV-vis-NIR	UV-visible-near-infrared
SEM	scanning electron microscopy
TEM	transmission electron microscopy
EDXA	energy-dispersive X-ray analysis
XPS	X-ray photoelectron spectroscopy
DBRL	distributed Bragg reflector laser
PC	polarization controller
FC	fiber coupler
OSA	optical spectrum analyzer
BR	blocker
FPC	fiber-port collimator
PR	polarize
OC	optical chopper
IRS	iris
APD	avalanche photodetector
BS	beam splitter
MR	mirror
VOA	variable optical attenuator
ECL	external cavity laser
FWHM	full width at half maximum
FEM	finite element method

Chapter 1 Introduction

1.1 Motivation

Metallic nanoparticles have been extensively studied and used in sensing, imaging, medicine, catalysis, photovoltaics, and nonlinear optics [1-6]. The morphology of nanoparticles is of great importance in these applications. The study of the acoustic vibrations of metal nanoparticles has been of great interest since the acoustic vibrations can provide insight into mechanical properties of nanoparticles due to the dependency of the acoustic vibrations on the size, shape and elastic properties of materials [7-9]. The acoustic vibrations of metallic nanoparticles have been extensively studied by the time-resolved pump-probe spectroscopy [10-13]. In a typical pump-probe experiment, an ultrafast laser is required to provide the pump pulses to excite the acoustic vibrations of the sample. After a controlled delay, the optical response of these vibrational modes is measured by recording the extinction or transmission change of the probe pulses. It is believed that high peak power of the pump laser is crucial for vibrational modes excitation and appreciable optical response detection. Our previous report on the acoustic vibrations of individual dielectric nanoparticles and proteins in an optical trapping setup shows that large response can be obtained even using relatively weak continuous-wave (CW) lasers [14]. This suggests that the acoustic vibrations of metal nanoparticles could also be studied without ultrafast lasers. Therefore, we investigate a four-wave mixing (FWM) setup using CW lasers to probe the acoustic vibrations of metallic nanoparticles in aqueous solution. By analyzing the resonant peak position and linewidth in the FWM signal, information about nanoparticle's shape, size, and size distribution can be obtained. Investigation of the FWM setup's effectiveness and accuracy on characterizing different metallic nanoparticles and in situ monitoring nanoparticle growth constitutes the first part of this work.

In the second part of this work, we focus on the direct application of metallic nanoparticles in surface-enhanced Raman scattering (SERS) for quantification of an exogenous cancer biomarker Acetyl Amantadine (AcAm). The action of the enzyme Spermidine/Spermine N1 Acetyl-transferase (SSAT) acetylates Am into AcAm in human bodies. SSAT's activities are significantly up-regulated in a variety of cancer cells (e.g., lung cancer), which makes AcAm an exogenous biomarker for cancer screening [15-18]. The current clinical method to quantify AcAm in urine uses liquid chromatography with tandem mass spectrometery (LCMS) [19]; a process which is of long analytical time, high instrument cost, and high per-sample cost. These disadvantages of LCMS present a barrier to its widescale clinical usage for AcAm quantification. Therefore, a faster and lower-cost method with comparable sensitivity with LCMS is highly desired.

SERS, a technique with fingerprint effect and ultra-high sensitivity, has been considered as one of the most powerful optical tools for trace chemical detection [20-22]. Similar to the conventional Raman spectroscopy, SERS provides specific fingerprint information by which molecules can be identified. Moreover, SERS enhances the conventional Raman's intrinsic low signal (caused by a small scattering cross section, typically 10^{-30} to 10^{-25} cm^{-2} per molecule [23]) by exciting the localized surface plasmon resonance (LSPR) on metallic nanostructures to form hot spots [24-26]. Therefore, SERS can significantly improve the sensitivity in quantitative analysis [27, 28].

Developing appropriate SERS substrates and sample preparation methods are the main challenges to achieve high sensitivity and low limit of detection (LOD). Cost (including substrate fabrication cost, instrumental cost, and time cost) should also be considered for practical usage. Based on these considerations, metallic (especially gold and silver) nanoparticles are one suitable option to meet the requirement due to the low material cost and high enhancement features. The other issue is how to extract molecules or analytes from volume onto metal surfaces since effective enhancement only occurs within hot spots. This requires appropriate surface functionalization based on analyte's specific affinity properties to other materials. Therefore, increasing SERS substrate field enhancement and increasing surface affinity to analytes are the two main issues to be investigated in this work.

1.2 Outline

The study of metallic nanoparticles' analytical properties of the acoustic vibrations and applications is the topic of this work. It comprises two major parts: nanoparticle acoustic resonance enhanced FWM for nanoparticle characterization and in situ growth monitoring and nanoparticle-based surface-enhanced Raman spectroscopy for trace cancer biomarker quantification.

Chapter 1 introduces the motivation and the outline of the thesis.

Chapter 2 serves as the background chapter, discussing different nanoparticle synthesis methods, localized surface plasmon resonance of metallic nanoparticles, different characterization methods, and surface-enhanced Raman spectroscopy.

Chapter 3 investigates the performance of the FWM setup on characterizing gold nanorod samples with different aspect ratios. The FWM signal shows an extensional vibration of gold nanorods which combines an expansion along the long axis with a contraction along the short axis. We also observed the extensional vibration of gold nanospheres as byproducts of the gold nanorod synthesis. Theoretical calculation of the nanoparticle size and distribution based on the vibrational frequencies agrees well with the experimental results obtained from the scanning electron microscopic examination, indicating the FWM technique can provide in situ nanoparticle characterization.

Chapter 4 investigates the performance of the FWM setup on characterizing silver nanoprisms and gold nano-octahedrons in aqueous solution. The nonlinear optical response shows two acoustic vibrational modes: an in-plane mode of nanoprisms with vertexial expansion and contraction; an extensional mode of nano-octahedrons with longitudinal expansion and transverse contraction. The experimental mode frequencies agree with theoretical approximations, which show an inverse dependence of the mode frequency on the edge length, for both nanoprisms and nano-octahedrons. The nanoparticles were also analyzed with electron microscopy and the acoustic resonance frequencies were then calculated by the finite element analysis, showing good agreement with experimental observations.

Chapter 5 investigates the performance of the FWM setup on monitoring in situ gold nanoparticle growth in aqueous solution. We observed two acoustic vibrational modes of gold nanoparticles from the nonlinear optical response: an extensional mode with longitudinal expansion and transverse contraction; and a breathing mode with radial expansion and contraction. The mode frequencies, which show an inverse dependence on the nanoparticle diameter, allow monitoring the nanoparticle size and size distribution during synthesis. The information about the nanoparticle size and size distribution calculated based on the mode frequencies agrees well with the results obtained from the electron spectroscopy analysis, validating the four-wave mixing technique as an accurate and effective tool for in situ monitoring of colloidal growth.

Chapter 6 summarizes the work towards developing nanoparticle-based SERS platforms step by step to achieve high sensitivity and low LOD. We investigate different commercial SERS substrates and discuss their advantages and disadvantages as the first step. Then we combine different nanoparticles (nanorods and nanospheres) with different surface functionalization agents (polystyrene and beta-cyclodextrin) to develop our own SERS substrates to achieve the high sensitivity and low LOD (below 1 ng/mL) goal.

Chapter 7 summarizes the works in the thesis and outlines the possible future works.

1.3 Publications and Contributions

This section summarizes the publications during the PhD program and states the specific contributions to each work.

(1). Characterizing gold nanorods in aqueous solution by acoustic vibrations probed with four-wave mixing [29], in which J. Wu conducted the FWM measurement on the gold nanorod samples, the SEM characterization and extinction measurement of the gold nanorod samples, and the data analysis. The manuscript was written by J. Wu and revised by R. Gordon. D. Xiang provided useful guidance and suggestions on the FWM measurement. Chapter 3 is based on this paper.

(2). Probing the acoustic vibrations of complex-shaped metal nanoparticles with four-wave mixing [30], in which J. Wu conducted the FWM measurement, the SEM characterization, the extinction measurement, and the related data analysis. G. Hajisalem synthesized the silver nanoprisms. F.C. Lin and C.H. Kuo synthesized the gold nanooctaherons. The manuscript was written by J. Wu and revised by R. Gordon and J.S. Huang. D. Xiang provided useful guidance and suggestions on the FWM measurement. Chapter 4 is based on this paper.

(3). Monitoring Gold Nanoparticle Growth in Situ via the Acoustic Vibrations Probed by Four-Wave Mixing [31], in which J. Wu conducted the gold nanoparticle synthesis, the FWM in-situ monitoring, the SEM characterization, the extinction measurement, and the related data analysis. The manuscript was written by J. Wu and revised by R. Gordon. D. Xiang provided useful guidance and suggestions on the FWM measurement. Chapter 5 is based on this paper.

(4). Trace cancer biomarker quantification using polystyrene-functionalized gold nanorods [32], in which J. Wu conducted the sample preparation, the extinction measurement, the Raman measurement, and the related data analysis. W. Li synthesized AcAm. G. Hajisalem conducted the dark-field scattering measurement of the gold nanorod samples. A. Lukach synthesized the polystyrene-functionalized gold nanorods. The manuscript was written by J. Wu and revised by R. Gordon. F. Hof and E. Kumacheva provided useful comments on the manuscript. Chapter 6 is mainly based on this paper.

(5). Threshold for Terahertz Resonance of Nanoparticles in Water [33], in which D. Xiang conducted the FWM measurement and the related data analysis. J. Rottler conducted the molecular dynamics simulation. The manuscript was written by D. Xiang and revised by R. Gordon. J. Wu helped with the FWM measurement.

(6). Coulomb Blockade Plasmonic Switch [34], in which D. Xiang conducted the sample fabrication, the transmission measurement, the FDTD simulation, and related data analysis. The manuscript was written by D. Xiang, and revised by R. Gordon. J. Wu helped with the wet etching process and the self-assembly monolayer deposition.

Chapter 2 Background

This chapter introduces the background information with regard to different nanoparticle synthesis methods, localized surface plasmon resonance of metallic nanoparticles, different characterization methods, and surface-enhanced Raman spectroscopy.

2.1 Synthesis of Colloidal Metallic Nanoparticles

Metallic nanoparticles can be generated by physical (top-down, e.g., laser ablation [35]) and chemical approaches. Here, we focus on chemical synthesis of colloidal metallic nanoparticles. The chemical reduction of metal salts is the fundamental process. This chemical reduction method involves two steps: nucleation and successive growth [36]. If the nucleation and successive growth are completed in the same process, it is called in situ synthesis; otherwise it is called seed-growth method. The seed-growth method is beneficial for size and morphology control.

2.1.1 In Situ Synthesis

In general, the synthesis of metallic nanoparticles by chemical reduction contains two major parts: reduction and stabilization. Different agents can be used in the two processes, such as citrate as both reducing and stabilizing agent [37,38], citrate as the stabilizing agent only and $NaBH_4$ or tannic acid as the reducing agent [39,40], $NaBH_4$ as the reducing agent and cetyltrimethylammonium bromide (CTAB) or Tetraoctylammonium bromide (TOAB) as the stabilizer [41,42]. The in situ synthesis is a simple method for synthesizing metallic nanoparticles. However, it is difficult to perform size and shape control.

2.1.2 Seed-Mediated Growth Method

The seed-mediated growth method is another popular method for metallic nanoparticle synthesis. Compared with the in situ method, the seed-mediated method grows nanoparticles step by step and it is easier to control the size and morphology. The seed-mediated method consists of two steps: the seed growth and the successive growth. In the seed growth, the seed nanoparticles are generated by reducing metal salts using suitable reducing agents. In the subsequent successive growth, the seed nanoparticles are added to the growth solution containing the same or different metal salts and milder reducing agents. Since the reducing agents in the growth solution are milder, the reduced metal ions can only assemble on the seed surface due to the need of metal seeds as catalysts. Moreover, the growth speed is slower than the seed growth. Thus, it is easy to perform size and morphology control. Metallic nanoparticles with various shapes (e.g., spherical, rod-shaped, triangular, octahedral, cubic) have been synthesized using the seed-mediated growth method [43-47].

2.1.3 Photo-Induced Method

The photo-induced method uses UV irradiation of the metal seed solution in the presence of reducing agents to achieve shape-controlled reduction of metal salts. This method is commonly used for silver nanoprisms synthesis. During the irradiation, silver nanospheres gradually grow into nanoprisms and the irradiation time controls the lateral dimension of nanoprisms [48].

2.2 Localized Surface Plasmon Resonance of Metallic Nanoparticles

2.2.1 Surface Plasmon Polaritons vs. Localized Surface Plasmons

Surface plasmons are coherent oscillations of delocalized electrons at the interface of two materials where the real part of the permittivity changes sign across the interface (e.g., a metal-dielectric interface), consisting of propagating (surface plasmon polaritons, SPPs, at a planar interface) and non-propagating (localized surface plasmons, LSPs, on a closed surface) surface waves [49]. Figure 2.1 illustrates the difference between SPPs and LSPs. Figure 2.1(a) shows a SPP propagating in the x directions along the metal-dielectric interface and decaying evanescently in the z-direction. Figure 2.1(b) shows light interacts with metallic nanoparticles much smaller than the incident wavelength, leading to a plasmon oscillating locally around the particle with a frequency as localized surface plasmon resonance (LSPR).

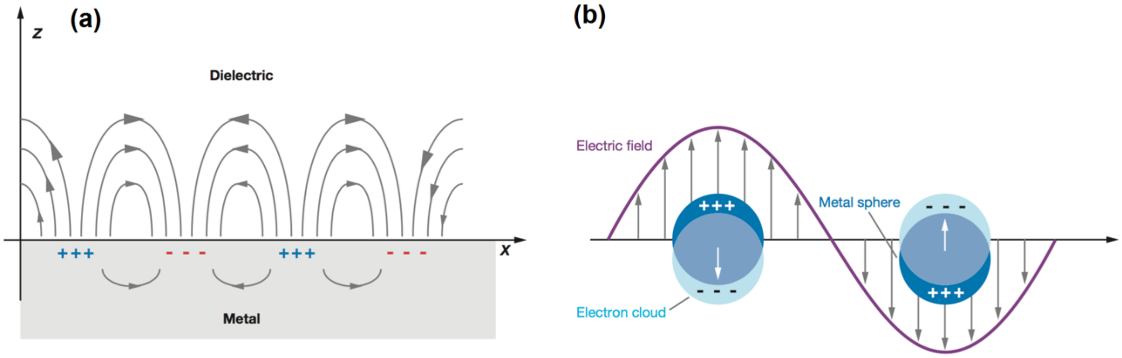

Figure 2.1 Schematic diagrams illustrating (a) a surface plasmon polariton (or propagating plasmon) and (b) a localized surface plasmon (non-propagating plasmon) [50].

2.2.2 Size and Shape Dependence

LSPR is sensitive to nanoparticle's size and shape. For example, Figure 2.2(a) shows the red shift of gold nanorod's longitudinal LSPR peak with increasing aspect ratio (length/width). Figure 2.2(b) shows the scattering spectra of individual silver nanoparticles with different shapes. The large LSPR difference indicates a strong shape dependence. However, for a spherical nanoparticle, the LSPR is not sensitive to the size. This will be discussed in the next two sections.

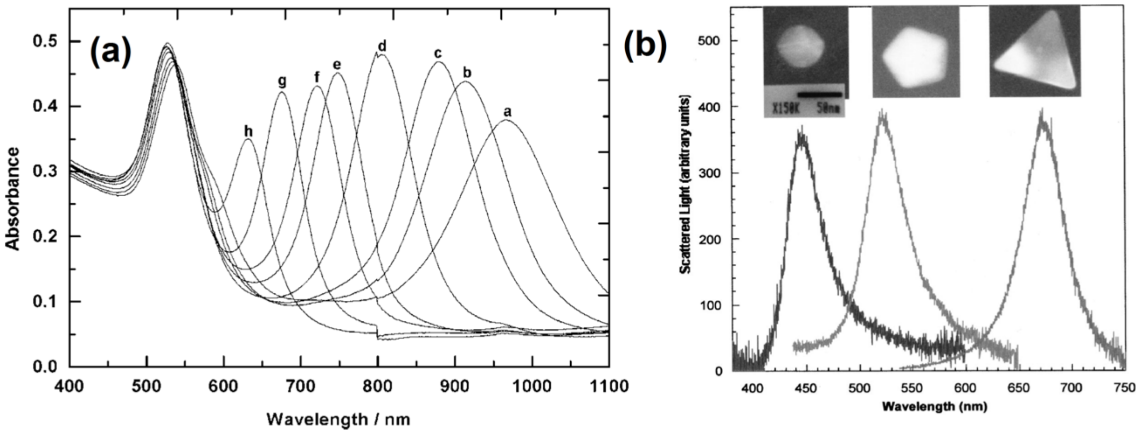

Figure 2.2 (a) Red shift of gold nanorod's longitudinal LSPR with increasing (from h to a) aspect ratio (length/width) [51]. (b) Scattering spectra of individual silver nanoparticles with different shapes. The large LSPR difference shows a strong shape dependence [52].

2.2.3 LSPR of a small spherical nanoparticle [49]

In this section, we analytically investigate the LSPR of a small spherical nanoparticle. The quasi-static approximation can be applied in this situation where the particle size is much smaller than the wavelength of the light in the surrounding medium [53]. This means that the phase of the harmonically oscillating electromagnetic field becomes constant over the particle's volume. Therefore, we can calculate the spatial field distribution by assuming that the particle is in an electrostatic field. After the spatial field distribution is obtained, we can then add the harmonic time dependence to the solution.

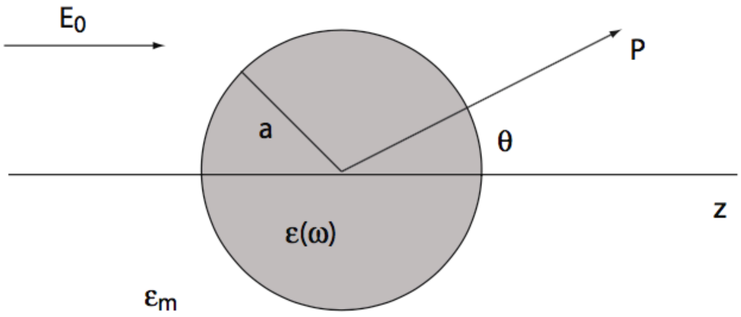

Figure 2.3 Sketch of a homogeneous spherical particle placed in an electrostatic field.

Figure 2.3 illustrates the simplest geometry: a homogeneous, isotropic sphere of radius a placed in a uniform, static field $\mathbf{E_0}$. In the electrostatic approach, we can first solve the Laplace equation for the potential $\nabla^2\Phi = 0$. Then we can calculate the electric field by $\mathbf{E} = -\nabla\Phi$. Due to the azimuthal symmetry of the configuration, the general solution can be expressed in the form of

$$\Phi(r,\theta) = \sum_{l=0}^{\infty}[A_l r^l + B_l r^{-(l+1)}]P_l(\cos\theta) \ , \tag{2.1}$$

where $P_l(\cos\theta)$ are the Legendre Polynomials of order l, and θ is the angle between the position vector $\mathbf{r}$ at point P and the z-axis shown in figure 2.3 [54]. Due to the requirement that the potential remains finite at the origin point ($r = 0$), the solution for the potentials inside the sphere Φ_{in} and outside the sphere Φ_{out} can be written as:

$$\Phi_{in}(r,\theta) = \sum_{l=0}^{\infty} A_l r^l P_l(\cos\theta), \tag{2.2}$$

$$\Phi_{out}(r,\theta) = \sum_{l=0}^{\infty} [B_l r^l + C_l r^{-(l+1)}] P_l(\cos\theta) . \tag{2.3}$$

The coefficients A_l, B_l, and C_l can be determined by the boundary conditions at $r \to \infty$ and at the sphere surface $r = a$. The boundary condition that when $r \to \infty$, $\Phi_{\text{out}} \to -E_0 z = -E_0 r \cos\theta$ requires that $B_1 = -E_0$ and $B_l = 0$ for $l \neq 1$. The boundary condition at the sphere surface $r = a$ requires the tangential components of the electric field equal and the normal components of the electric displacement field are equal inside and outside the sphere:

$$-\frac{1}{a}\frac{\partial \Phi_{in}}{\partial \theta}\bigg|_{r=a} = -\frac{1}{a}\frac{\partial \Phi_{out}}{\partial \theta}\bigg|_{r=a} , \tag{2.4}$$

$$-\varepsilon_0 \varepsilon \frac{\partial \Phi_{in}}{\partial r}\bigg|_{r=a} = -\varepsilon_0 \varepsilon_m \frac{\partial \Phi_{out}}{\partial r}\bigg|_{r=a} , \tag{2.5}$$

leading to $A_l = C_l = 0$ for $l \neq 1$. Therefore, we can calculate the remaining coefficients A_1 and C_1 and hence, the potentials:

$$\Phi_{in} = -\frac{3\varepsilon_m}{\varepsilon + 2\varepsilon_m} E_0 r \cos\theta , \tag{2.6}$$

$$\Phi_{out} = -E_0 r \cos\theta + \frac{\varepsilon - \varepsilon_m}{\varepsilon + 2\varepsilon_m} E_0 a^3 \frac{\cos\theta}{r^2} . \tag{2.7}$$

According to Equation 2.7, Φ_{out} is the superposition of the incident field and that of a dipole located at the particle center. Therefore, we can rewrite Φ_{out} by using the dipole moment **p** as:

$$\Phi_{out} = -E_0 r \cos\theta + \frac{\mathbf{p} \cdot \mathbf{r}}{4\pi\varepsilon_0 \varepsilon_m r^3} , \tag{2.8}$$

$$\mathbf{p} = 4\pi\varepsilon_0 \varepsilon_m a^3 \frac{\varepsilon - \varepsilon_m}{\varepsilon + 2\varepsilon_m} \mathbf{E}_0 . \tag{2.9}$$

We can see that the applied field introduces a dipole moment inside the sphere with magnitude proportional to $|\mathbf{E_0}|$. If we introduce the polarizability α by defining $\mathbf{p} = \varepsilon_0\varepsilon_\mathrm{m}\alpha\mathbf{E_0}$, we can obtain

$$\alpha = 4\pi a^3 \frac{\varepsilon - \varepsilon_m}{\varepsilon + 2\varepsilon_m}. \tag{2.10}$$

The distribution of the electric field $\mathbf{E} = -\nabla\Phi$ can be obtained from the potentials (Equations 2.6 and 2.7):

$$\mathbf{E}_{in} = \frac{3\varepsilon_m}{\varepsilon + 2\varepsilon_m}\mathbf{E}_0, \tag{2.11}$$

$$\mathbf{E}_{out} = \mathbf{E}_0 + \frac{3\mathbf{n}(\mathbf{n}\cdot\mathbf{p}) - \mathbf{p}}{4\pi\varepsilon_0\varepsilon_m}\frac{1}{r^3}. \tag{2.12}$$

It is apparent that the polarizability will experience a resonant enhancement under the condition that $|\varepsilon + 2\varepsilon_\mathrm{m}|$ is a minimum, which requires that

$$\mathrm{Re}[\varepsilon(\omega)] = -2\varepsilon_m. \tag{2.13}$$

It should be noted that the magnitude of α at resonance is not infinite and is limited by the incomplete vanishing of the denominator due to $\mathrm{Im}[\varepsilon(\omega)] \neq 0$. The resonance in α also implies a resonance enhancement of both the internal and dipolar fields according to Equations 2.11 and 2.12.

The scattering cross section of the spherical particle can be obtained by dividing the total radiated power of the sphere's dipole by the intensity of the exciting plane wave, which leads to

$$\sigma_{scatt} = \frac{k^4}{6\pi}|\alpha|^2 = \frac{8\pi}{3}k^4 a^6 \left|\frac{\varepsilon - \varepsilon_m}{\varepsilon + 2\varepsilon_m}\right|^2, \tag{2.14}$$

where k is the wave vector in the surrounding medium.

The power dissipated by a point dipole can be determined as [55]:

$$P_{abs} = \frac{\omega}{2}\,\mathrm{Im}[\mathbf{p}\cdot\mathbf{E}_0^*]. \tag{2.15}$$

Using $\mathbf{p} = \varepsilon_0\varepsilon_m\alpha\mathbf{E_0}$ and the expression for the intensity of the incident plane wave in the surrounding medium ($I = cn\varepsilon_0\,|\mathbf{E_0}|^2/2$), we can obtain the absorption cross section:

$$\sigma_{abs} = k\,\mathrm{Im}[\alpha] = 4\pi k a^3\,\mathrm{Im}\left[\frac{\varepsilon-\varepsilon_m}{\varepsilon+2\varepsilon_m}\right]. \tag{2.16}$$

According to Equations 2.15 and 2.16, σ_{abs} scales with a^3 while σ_{scatt} scales with a^6. Therefore, for small particles, the extinction is dominated by absorption, whereas for larger particles, the extinction is dominated by scattering. For a sphere of volume V and dielectric function $\varepsilon = \varepsilon_1 + i\varepsilon_2$, the extinction cross section can be expressed by:

$$\sigma_{ext} = \sigma_{abs} + \sigma_{scatt} = 9\frac{\omega}{c}\varepsilon_m^{2/3}V\frac{\varepsilon_2}{[\varepsilon_1+\varepsilon_m]^2+\varepsilon_2^2}. \tag{2.17}$$

Figure 2.4 compares the extinction cross section of a silver sphere in two different surrounding media calculated using Equation 2.17. The dielectric data is taken from [56].

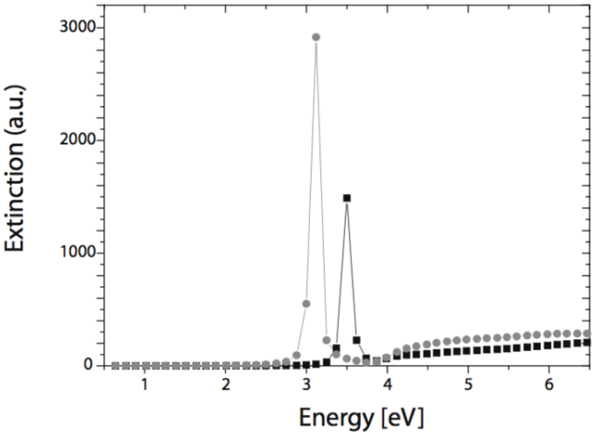

Figure 2.4 Extinction cross section of a silver sphere in air (square) and in silica (dot) calculated using Equation 2.17 [57].

2.2.4 Beyond the Quasi-Static Approximation [49]

The previous section analyzes the extinction cross section of a sphere under the quasi-static approximation which requires the size of the sphere is much smaller than the wavelength of the excitation plane wave. However, as the size of particle increases (e.g., > 100 nm), the quasi-static approximation becomes inapplicable due to the non-negligible phase change of the excitation wave over the particle volume. The Mie theory is a rigorous electrodynamic approach to understand the scattering and absorption of electromagnetic wave by a sphere by expanding the internal and scattered fields into a set of normal modes described by vector harmonics [58]. The expansion of the first TM mode of Mie theory yields the expression for the polarizability of a sphere of volume V [59]:

$$\alpha_{sphere} = \frac{1-(\frac{1}{10})(\varepsilon+\varepsilon_m)x^2+O(x^4)}{(\frac{1}{3}+\frac{\varepsilon_m}{\varepsilon-\varepsilon_m})-\frac{1}{30}(\varepsilon+10\varepsilon_m)x^2-i\frac{4\pi^2\varepsilon_m^{3/2}}{3}\frac{V}{\lambda_0^3}+O(x^4)}V, \quad (2.18)$$

where $x = \pi a/\lambda_0$ is the size parameter involving the radius to the free space wavelength. Compared to Equation 2.10, a number of additional terms appear in the numerator and denominator in Equation 2.18. The quadratic term of x in the numerator is caused by the effect of retardation of the excitation field over the volume of the sphere, while the quadratic term of x in the denominator is caused by the retardation of the depolarization field inside the sphere [60]. Both the quadratic terms can cause an energy shift of the resonance. For Drude and the noble metals, the overall shift is towards the lower energy side: the spectral position of the dipole resonance red-shifts with increasing the size of the sphere. Figure 2.5 shows the extinction efficiency of a gold sphere with different diameters ranging from 2.5 to 100 nm (from bottom to top) [67]. The ~40-nm red-shift is not significant compared to the large size change. Therefore, the LSPR of a spherical nanoparticle is not very sensitive to its size. If we want to monitor spherical nanoparticle growth, we need a better method which should have higher sensitivity on nanoparticle's size.

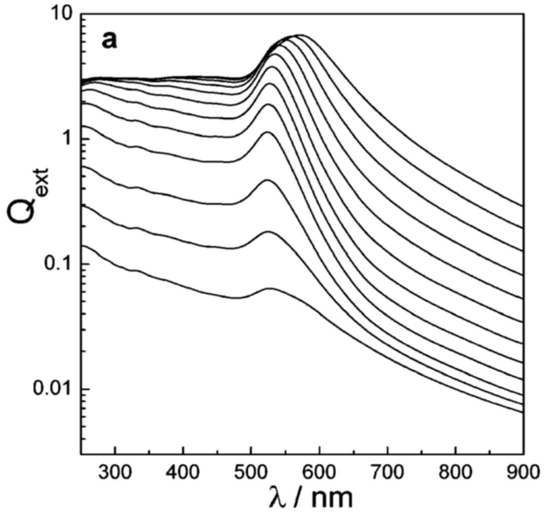

Figure 2.5 Calculated extinction efficiency in dependence of wavelength for gold particle diameters of 2.5, 5, 10, 20, 30, 40, 50, 60, 70, 80, 90, and 100 nm (from bottom to top).

2.2.5 Linewidth of LSPR

If we only consider Equation 2.17, we would intuitively conclude that the linewidth of LSPR would behave like the Dirac delta function. However, in reality, the linewidth of LSPR is broadened in a single nanoparticle and also in an ensemble of nanoparticles with size and shape variations. The linewidth broadening in a single nanoparticle can be attributed to homogenous or intrinsic broadening. The linewidth broadening in nanoparticle ensembles is a combination of homogenous broadening and inhomogeneous broadening which comes from the shape and size variations. This section we mainly focus on the homogenous broadening.

The linewidth of LSPR is closely related to the lifetime of the surface plasmon oscillation. Narrower linewidth corresponds to slower dephasing time of the coherent plasmon oscillation and therefore longer lifetime, while broader linewidth corresponds to faster dephasing time and therefore shorter lifetime. The homogeneous linewidth Γ is related to the dephasing time T_2 of the coherent plasmon oscillation by [61]:

$$\Gamma = \frac{2}{T_2}. \tag{2.19}$$

The dephasing time T_2 is limited by elastic and inelastic decay processes, where the latter is dominant for nanoparticle plasmons and involves the decay of a plasmon into the excitation of electron-hole pairs through intraband and interband transitions [62].

The homogeneous linewidth Γ can also be expressed as a sum of several plasmon damping terms [62]:

$$\Gamma = \gamma_b + \Gamma_{\text{rad}} + \Gamma_{\text{e-surf}} + \Gamma_{\text{interface}}, \tag{2.20}$$

where γ_{b}, Γ_{rad}, $\Gamma_{\text{e-surf}}$, and $\Gamma_{\text{interface}}$ correspond to bulk damping, radiation damping, damping due to electron surface scattering, and damping due to interfacial effects, respectively.

The bulk damping term γ_{b} comes from the electron scattering in the metal. It is described by the complex permittivity of the metal and is hence frequency dependent. For gold nanoparticles, the linewidth increases with increasing the plasmon resonance energy, and additional plasmon broadening occurs at the onset of interband transitions at higher energies [63].

Γ_{rad} denotes the energy loss mechanism due to coupling of the plasmon oscillation to the radiation field, known as the radian damping. Γ_{rad} is especially important for large particles. Γ_{rad} scales with the nanoparticle volume by:

$$\Gamma_{\mathrm{rad}} = \frac{h\kappa_{\mathrm{rad}}V}{\pi}, \tag{2.21}$$

where h is the Plank constant, κ_{rad} is the radiation damping constant ranging from 4×10^{-7} to 12×10^{-7} fs/nm, and V is the nanoparticle volume [64].

When the nanoparticle size becomes shorter than the electron mean free path, damping from electron surface scattering $\Gamma_{\text{e-surf}}$ must be included [65]. $\Gamma_{\text{e-surf}}$ can be expressed by:

$$\Gamma_{\text{e-surf}} = \frac{S_{\mathrm{A}}v_{\mathrm{F}}}{L_{eff}}, \tag{2.22}$$

where S_{A} is the surface scattering constant, v_{F} is the Fermi velocity, and L_{eff} is the effective path length of the electrons. L_{eff} can be described by the particle volume V and the surface area S as $L_{\mathrm{eff}} = 4V/S$. For example, L_{eff} of a nanosphere simply equals to its radius.

$\Gamma_{\mathrm{interface}}$ describes the damping from the interfacial effects. It is believed that energy or electrons which transfer to surface bond molecules creates an additional relaxation pathway for nanoparticle surface plasmons, leading to shorter lifetimes and hence broader linewidth [66]. The interface damping is relatively weak compared to other damping mechanisms.

2.3 Characterization of Metallic Nanoparticles

2.3.1 Common Characterization Methods

Characterization of metallic nanoparticles commonly includes assessment of dimensionality, morphology, and composition. Multiple techniques are often used in tandem for comprehensive characterization. Commonly used characterization techniques include UV-visible-near-infrared (UV-vis-NIR) spectroscopy for extinction measurement [67], scanning electron microscopy (SEM) and transmission electron microscopy (TEM) for direct imaging [68,69], energy-dispersive X-ray analysis (EDXA) and X-ray photoelectron spectroscopy (XPS) for surface composition analysis [70,71].

2.3.2 Acoustic Vibration Characterization Methods

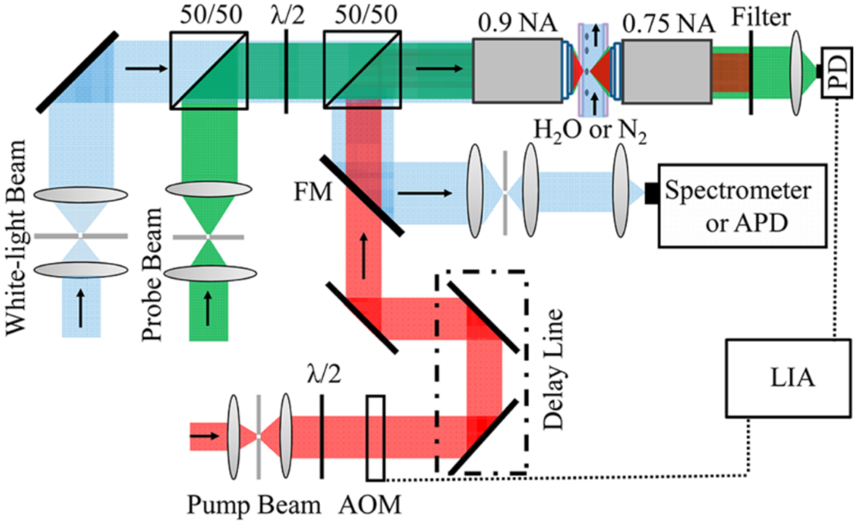

Figure 2.6 Schematic of the time-resolved transmission setup, consisting of femtosecond pulsed pump and probe beams with a variable delay. AOM: acousto-optical modulator; DM: dichroic mirror; PD: photodiode; F: optical filters [7].

Investigating acoustic vibrations of metallic nanoparticles is another characterization technique since the acoustic resonance is dependent on size, shape and elastic properties of materials [7-9]. Acoustic vibrations of metallic nanoparticles with different shapes (e.g., spherical, rod-shaped, triangular, cubic) have been extensively studied by the time-resolved pump-probe spectroscopy [72-74]. The idea is to use a pump pulse to excite nanoparticles' acoustic vibrations and use another probe pulse to detect the transmission or extinction change caused by nanoparticle's deformation. Figure 2.6 shows a typical pump-probe setup for investigating nanoparticle's acoustic vibrations. Acoustic vibrations are excited with pulses from a Ti/sapphire laser and probed by the frequency-doubled output of an Optical Parametric Oscillator. The intensity of the pump beam is modulated by an acousto-optical modulator at a frequency around 400 kHz. The transmitted intensity of the probe beam is recorded with a fast Si-PIN (a semiconductor structure with an undoped intrinsic region between a p-type and an n-type region) photodiode, and a lock-in amplifier extracts the small change of the detected probe intensity δT at the modulation frequency. The vibration trace of the nanoparticle is obtained by recording δT(t) as function of the time delay t between pump and probe pulses, controlled by a mechanical delay stage. Fitting the curve with a sum of oscillating terms gives the frequency information of different vibrational modes.

The vibrational frequencies can be calculated by applying the macroscopic theory of elastic waves (e.g., the Lamb theory [75]) to nanoparticles. Here, we present the calculation of the eigenmodes of a sphere's acoustic vibrations. The eigenmodes can be obtained by solving the motion equation [76]:

$$v_l^2 \nabla \cdot (\nabla \cdot \boldsymbol{u}) - v_t^2 \nabla \times (\nabla \times \boldsymbol{u}) = -\omega^2 \boldsymbol{u}, \tag{2.23}$$

where $\boldsymbol{u}(\boldsymbol{r},t)=\boldsymbol{u}(\boldsymbol{r})e^{-i\omega t}$ is the displacement at position $\boldsymbol{r}$ and time t, ω is the angular mode frequency. After introducing two quantities, $\Lambda=\nabla\cdot\boldsymbol{u}$ and $\boldsymbol{\Gamma}=\nabla\times\boldsymbol{u}$, the motion equation can be expressed as:

$$\left(\nabla^2+Q^2\right)\boldsymbol{\Gamma}=\boldsymbol{0}, \tag{2.24}$$

$$\left(\nabla^2+q^2\right)\Lambda=0, \tag{2.25}$$

where $Q^2=\omega^2/v_t^2$ and $q^2=\omega^2/v_l^2$. v_t and v_l are the transverse and longitudinal sound velocity, respectively. The solution can be expressed in spherical coordinate as:

$$\boldsymbol{u}=-\frac{A}{q^2}\begin{pmatrix}\dfrac{\partial}{\partial r}j_l(qr)\\ 0\\ \dfrac{j_l(qr)}{r}\end{pmatrix}+\frac{1}{Q^2}\left[B\begin{pmatrix}\dfrac{l(l+1)}{r}j_l(Q_r)\\ 0\\ \dfrac{1}{r}\dfrac{\partial}{\partial r}[rj_l(Qr)]\end{pmatrix}-C\begin{pmatrix}0\\ Qj_l(Qr)\\ 0\end{pmatrix}\right], \tag{2.26}$$

where A, B, and C are coefficients evaluated by the initial conditions and j_l is the lth order spherical Bessel function. The force normal to the particle surface can be obtained by calculating the derivative of the displacement $\boldsymbol{u}$:

$$\begin{aligned}\boldsymbol{F}=A2v_t^2\rho&\begin{pmatrix}\dfrac{\partial^2}{\partial(qr)^2}[j_l(qr)]-\dfrac{v_l^2-2v_t^2}{2v_t^2}j_l(qr)\\ 0\\ \dfrac{\partial}{\partial qr}(\dfrac{j_l(qr)}{qr})\end{pmatrix}\\ -2v_t^2\rho&\left[B\begin{pmatrix}l(l+1)\dfrac{\partial}{\partial Qr}\left(\dfrac{j_l(Qr)}{Qr}\right)\\ 0\\ \dfrac{\partial}{\partial Qr}\left(\dfrac{1}{Qr}\dfrac{\partial}{\partial Qr}\left[Qrj_l(Qr)\right]\right)-\dfrac{1}{2}j_l(Qr)\end{pmatrix}-\frac{C}{2}\begin{pmatrix}0\\ Qr\dfrac{\partial}{\partial Qr}\left(\dfrac{j_l(Qr)}{QR}\right)\\ 0\end{pmatrix}\right],\end{aligned} \tag{2.27}$$

where ρ is the density of the nanoparticle. We apply the free boundary condition which requires that there is no force the particle surface on ***F*** to obtain:

$$l = 0: \frac{\tan(qa)}{qa} = \frac{1}{1-(v_l^2/4v_t^2)q^2a^2}, \tag{2.28}$$

$$\begin{aligned} l \neq 0: &-\frac{Q^2a^2}{2}(2l^2-l-1-\frac{Q^2a^2}{2})j_l(qa)j_l(Qa)+(l^3+2l^2-l-2-Q^2a^2)qaj_{l+1}(qa)j_l(Qa) \\ &+(l^3+l^2-2l-\frac{Q^2a^2}{2})Qaj_l(qa)j_{l+1}(Qa)+(2-l^2-l)qaQaj_{l+1}(qa)j_{l+1}(Qa)=0 \end{aligned} \tag{2.29}$$

where a is the radius of the nanosphere. Equations 2.28 and 2.29 establish the relation between the mode frequency and the nanoparticle size. For example, for a gold nanosphere with radius a, $v_l = 3240\,m/s$ and $v_t = 1200\,m/s$ [77], we can obtain the dependence for the breathing mode ($l = 0$) and the extensional mode ($l = 2$) as:

$$\omega_{l=0} = \frac{\eta v_l}{a}, \tag{2.30}$$

$$\omega_{l=2} = \frac{\xi v_l}{a}, \tag{2.31}$$

where $\eta = 2.945$ and $\xi = 0.985$ are coefficients obtained from Equations 2.28 and 2.29. Therefore, we can conclude the mode frequency of a nanoshpere has an inverse dependence on the size. Similar calculations have been performed on nanoparticles of different shapes (e.g., nanorods and nanoprisms [7,78]).

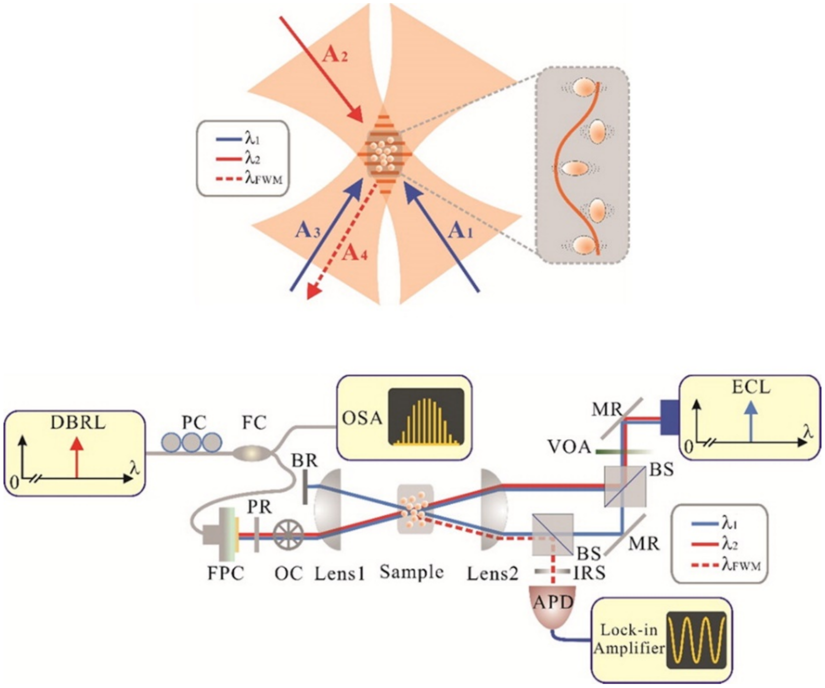

Figure 2.7 Experimental configuration of FWM. DBRL, distributed Bragg reflector laser; PC, polarization controller; FC, fiber coupler; OSA, optical spectrum analyzer; BR, blocker; FPC, fiber-port collimator; PR, polarizer; OC, optical chopper; IRS, iris; APD, avalanche photodetector; BS, beam splitter; MR, mirror; VOA, variable optical attenuator; ECL, external cavity laser [33].

For the pump-probe method to probe the acoustic vibrations of nanoparticles, it is believed that high peak power of the pump laser is crucial for vibrational modes excitation and appreciable optical response detection [7-13]. Our previous report on the acoustic vibrations of individual dielectric nanoparticles and proteins in an optical trapping setup showed that a large response can be obtained even using relatively weak continuous-wave (CW) lasers [14]. This suggests that the acoustic vibrations of metal nanoparticles could also be studied without ultrafast lasers. Therefore, we developed a four-wave mixing (FWM) setup using CW lasers to probe the acoustic vibrations of nanoparticles in aqueous solution as shown in Figure 2.7. We use an external cavity laser and a distributed Bragg reflector laser tuned to slightly different wavelengths to obtain non-degenerate response. The interference between the two counter-propagating beams (A_2 and A_3) imposes an electrostrictive force that stretches nanoparticles along the beam polarization. When the beat frequency of the two beams matches the acoustic resonance, the acoustic vibrations of nanoparticles will be resonantly excited, resulting a travelling periodic variation in refractive index of the medium which behaves as a moving Bragg grating. The FWM signal wave A_4 is then created as the beam A_1 diffracts from the Bragg grating.

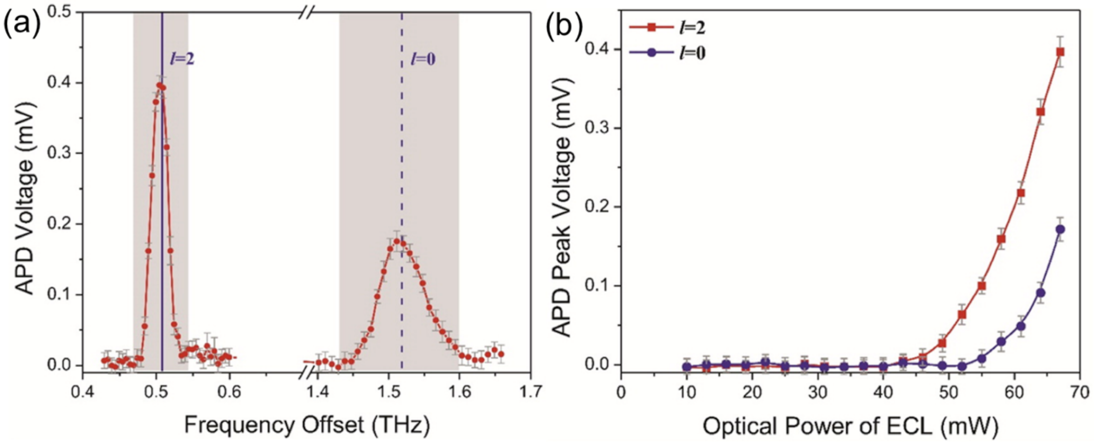

Figure 2.8 (a) FWM signal for 2 nm gold nanoparticles in water. Peaks at 504 GHz and 1.511 THz correspond to the $l = 2$ and $l = 0$ acoustic vibrations of 2 nm gold spheres. (b) Power dependence of the FWM signal for the $l = 2$ and $l = 0$ modes. A clear threshold is observed above which the nonlinear response "turns on" [33].

Figure 2.8(a) shows the FWM signal for 2 nm gold nanoparticles in water. Peaks at 504 GHz and 1.511 THz correspond to $l = 2$ (extensional) and $l = 0$ (breathing) acoustic vibrations of 2 nm gold spheres. The distribution with 8% dispersion in particle diameter is shown with gray shading. The experimentally observed linewidth of the resonant response is within the specified dispersion. This suggests that inhomogeneous broadening is the dominant factor in the observed linewidth.

Figure 2.8(b) shows the power dependence of the FWM signal. A clear threshold is observed: 43 mW for the $l = 2$ resonance and 55 mW for the $l = 0$ resonance. Below the threshold, there is negligible FWM signal. Above the threshold, the signal increases with the power of the external cavity laser. One possible explanation of the observed threshold is the formation of a cavity or bubble around the oscillating nanoparticles. When electrostriction force driving the particle motion is strong enough, the water molecules will be pushed away. Calculation shows that the collapse time for the bubble around the gold nanoparticle is larger than the oscillation period. This may be viewed as the threshold condition to obtain oscillation with low damping, that is, to maintain a stable bubble that does not collapse.

2.4 Metallic Nanoparticles in Surface-Enhanced Raman Spectroscopy

The direct application of metallic nanoparticles is in surface-enhanced Raman spectroscopy (SERS). It is important to characterize the nanoparticles thoroughly (e.g., using FWM) before applying them in SERS because the SERS intensity depends on the excitation of the LSPR [79] and the LSPR of the nanoparticles closely depends on the shape and size as described in section 2.2. This section introduces different methods of using metallic nanoparticles in SERS.

2.4.1 Metallic Colloids

A simple method is to use metallic nanoparticles in solution by mixing metallic colloids with the analyte solution. Molecules locating at nanoparticles’ hot spots due to the LSPR can experience large enhancement. This simple metallic colloidal method can achieve single molecule detection [80]. Different surface functionalization techniques (e.g., β-cyclodextrin, polymer) have been used to increase the surface adsorption for sensitivity improvement [81,82].

2.4.2 Planar Substrates

Planar SERS substrates can be created by transferring metallic nanoparticles from solution onto a planar substrate (glass, silicon, metals, papers, etc.). The simplest way is by drying colloidal solutions on planar substrates known as drop coating. Other novel methods such as inkjet printing and filter paper loading have been developed [83,84]. Planar substrates can be used simply by dipping in or dropping the analyte solution.

2.4.3 Nanogap Structures

Nanogaps are structures formed between nanoparticles brought closely to each other. Nanogaps usually provide larger field enhancement than single metallic nanoparticle. Analytes situate in nanogaps can experience large field enhancement. The gap distance is one of the crucial parameters that determines the local field enhancement. Controlled gap distance is desired for reproducibility in SERS experiment. Supramolecules such as cyclodextrins and cucurbit[n]urils have been used as rigid spacers to form nanogaps (~1nm) between nanospheres and nanorods [85-87].

2.5 Summary

In this chapter, we introduced the background information about the nanoparticle synthesis, the LSPR, different characterization methods and the SERS application. We mainly discussed the fundamentals of the nanoparticle LSPR and the acoustic vibration characterization. We showed the limitations of the common characterization methods (e.g., the insensitivity of the extinction measurement on nanospheres' size), which suggests that we should resort to the acoustic vibration characterization probed by FWM since the acoustic vibration shows larger sensitivity on nanoparticles' size. We also concluded that the shape and size characterization of the nanoparticles is important in the SERS application. Therefore, the development of a FWM setup to probe the acoustic vibrations for nanoparticle characterization and the application of the nanoparticles in SERS sensing compose the major work of the thesis.

Chapter 3 Characterizing Gold Nanorods in Aqueous Solution by Acoustic Vibrations Probed with Four-Wave Mixing

3.1 Introduction

In situ characterization of metallic nanoparticles in aqueous solution is of great importance for nanoparticle synthesis. The common characterization methods include the extinction measurement and the direct imaging by scanning or transmission electron microscopy (SEM, TEM) [88-91]. The extinction measurement can achieve in situ characterization. However, the extinction spectrum alone cannot provide the complete information about nanoparticle’s size and shape. For instance, gold nanorods have two localized surface plasmon resonance (LSPR) bands, corresponding to the longitudinal LSPR (along the long axis) band and the transverse LSPR (along the short axis) band [92]. The longitudinal band, which can be tuned from visible to near-infrared region, exhibits linear dependence on the aspect ratio (length/width) while the transverse band is insensitive to the size [93]. Therefore, the extinction spectrum which shows the LSPR bands can provide information about the aspect ratio only. SEM or TEM characterization is still needed for further determination of the length, width, and size distribution.

Acoustic vibrations can provide insight into mechanical properties of nanoparticles since the acoustic resonance is dependent on size, shape and elastic properties of materials [7-9]. Therefore, we use a four-wave mixing (FWM) setup to probe the acoustic vibrations of metallic nanoparticles in aqueous solution. The nonlinear optical response of metallic nanoparticles is resonantly enhanced by the electrostriction force which couples to the acoustic vibrations of nanoparticles. By analyzing the resonant peak position and linewidth of the FWM signal, information about nanoparticle's shape, size, and size distribution can be obtained. In this chapter, we investigate the performance of the FWM setup on characterizing gold nanorod samples with different aspect ratios.

3.2 Experimental Setup

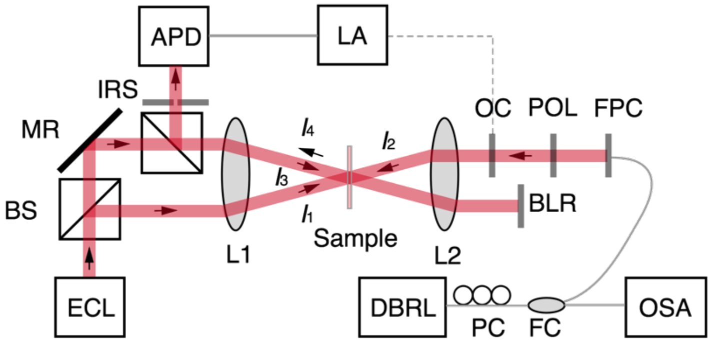

Figure 3.1. FWM experimental setup. ECL: external cavity laser; BS: beam splitter; MR: mirror; IRS: iris; APD: avalanche photodetector; LA: lock-in amplifier; L1: lens1 (20 cm focal length); L2: lens2 (4 cm focal length); DBRL: distributed Bragg reflector laser; PC: polarization controller; FC: fiber coupler; OSA: optical spectrum analyzer; BLR: blocker; OC: optical chopper; POL: polarizer; FPC: fiber-port collimator.

Figure 3.1 shows the FWM experimental setup. The sample placed in a quartz cuvette was illuminated by the counter-propagating optical beams composed of a continuous-wave (CW) tunable external-cavity laser (ECL) (DL100, Toptica Photonics) and a CW tunable distributed Bragg reflector laser (DBRL) (DBR852P, Thorlabs). The polarization of the DBRL beam was adjusted by a polarization controller and a polarizer to ensure co-polarized illumination. Weak focusing lenses were used with focal lengths of 20 cm (lens1) and 4 cm (lens2), respectively. The maximum power illuminated on the sample is

92 mW (67 mW from the ECL and 25 mW from the DBRL). If we assume a 100 μm beam diameter, the intensity would be 12 MW/m^2, which is relatively small compared to the peak intensity (4 GW/m^2) of the femtosecond laser used in the pump-probe experiment [7]. The angle between the two laser beams focused by the lens1 (I_1 and I_3) was adjusted around 4^o to allow the full coverage of the cuvette thickness (1 mm) as the light-matter interaction region. The interference between the two counter-propagating beams (I_2 at frequency ω_2 and I_3 at frequency ω_3) imposes an electrostrictive force that stretches nanoparticles along the beam polarization. When the beat frequency ($\omega_3 - \omega_2$) matches the acoustic resonance, the acoustic vibrations of nanoparticles will be resonantly excited, resulting a travelling periodic variation in refractive index of the medium which behaves as a moving Bragg grating. The FWM signal wave I_4 at frequency ω_4 ($\omega_4 = \omega_2$) is then created as the beam I_1 at frequency ω_1 ($\omega_1 = \omega_3$) diffracts from the Bragg grating. An optical chopper was used to modulate beam I_2. The FWM signal was measured by an avalanche photodetector (APD120A, Thorlabs) connected to a lock-in amplifier (SR510, Stanford Research Systems). The power of the ECL was set to 67 mW and the wavelength was fixed at 853.4 nm. The power of the DBRL was set to 25 mW and the wavelength (> 853.4 nm) was monitored by an optical spectrum analyzer (86142B, Agilent) during the wavelength tuning. The APD output voltage was recorded as a function of the frequency difference of the two lasers.

3.3 Results

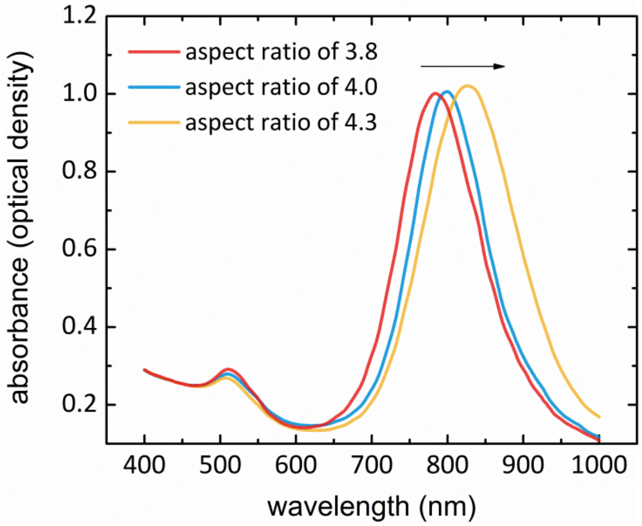

Figure 3.2. Extinction spectra of gold nanorods of three different aspect ratios in aqueous solution. The longitudinal LSPR peaks locate at 780, 800, and 830 nm for aspect ratios of 3.8, 4.0, and 4.3, respectively. The transverse LSPR peaks locate at 512 nm.

Figure 3.2 shows the extinction spectra of gold nanorods (Nanopartz) of three different aspect ratios in aqueous solution. The longitudinal LSPR peaks locate at 780, 800, and 830 nm while the transverse LSPR peaks locate at 512 nm. The longitudinal LSPR peak position has a linear correlation with the aspect ratio. According to the published results [93], gold nanorods with longitudinal LSPR peaks locating at 780, 800, and 830 nm have aspect ratios of 3.8, 4.0, and 4.3, respectively.

Figure 3.3(a) shows the SEM image of gold nanorods of 3.8 aspect ratio obtained at 2 kV and 700k× magnification. The spherical byproducts can be clearly seen in the image. We manually measured 32 nanorods and 32 nanospheres from the SEM image to obtain the size distribution. Histograms were fitted by Gaussian distribution. Results show that the nanorods have an average length of 38.2 ± 3.0 nm and an average width of 10.0 ± 1.0

nm. The aspect ratio is 3.82, which matches the value obtained from the extinction spectrum. The coexisting nanospheres have an average diameter of 14.0 ± 2.1 nm. The errors represent the standard deviation. We performed the same characterization on the other two aspect-ratio nanorod samples (see A.1). Table 3.1 summarizes the size information of the three different aspect-ratio samples based on SEM characterization.

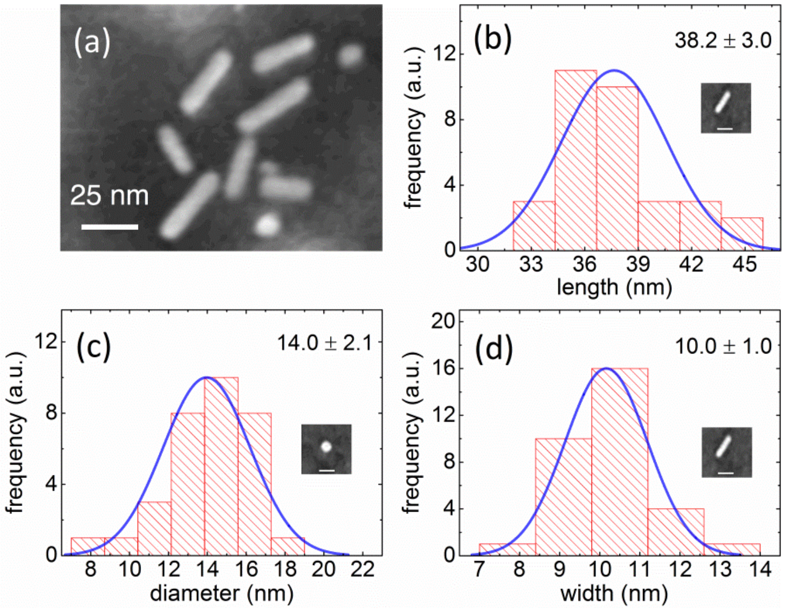

Figure 3.3. (a) SEM image of gold nanorods of 3.8 aspect ratio obtained at 2 kV and 700k× magnification. (b) Length distribution of gold nanorods. (c) Diameter distribution of gold nanospheres as the byproduct. (d) Width distribution of gold nanorods. Histograms were fitted by Gaussian distribution. The errors represent the standard deviation. The inset images are the SEM images of a single nanorod and nanosphere with a 25 nm scale bar.

	nanorods		coexsiting nanospheres
aspect ratio	length (nm)	width (nm)	diameter (nm)
3.8	38.2 ± 3.0	10.0 ± 1.0	14.0 ± 2.1
4.0	41.0 ± 3.3	10.2 ± 1.0	14.6 ± 2.2
4.3	45.1 ± 3.8	10.5 ± 1.1	15.5 ± 2.5

Table 3.1 Size information of three different aspect-ratio nanorod samples.

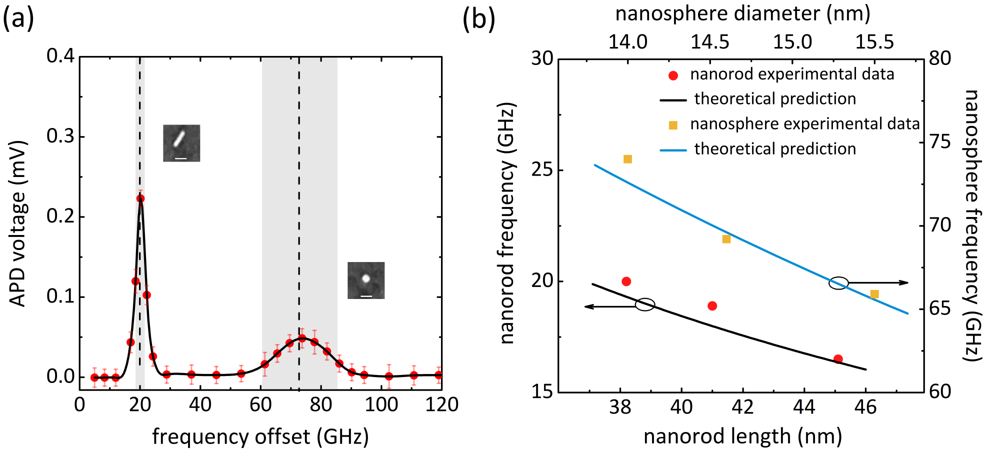

Figure 3.4. (a) FWM signal of the 3.8 aspect-ratio nanorod sample as a function of the beat frequency between the ECL and DBR lasers. The error bar stands for the standard deviation calculated by taking 148 data points at each beat frequency. The 20.0 and 74.0 GHz resonance peaks correspond to the frequencies of the extensional modes of gold nanorods and nanospheres, respectively. The dashed line indicates the calculated resonant frequencies of 19.3 and 72.6 GHz according to the SEM results. The grey area indicates the broadening (3.6 GHz for the nanorod extensional mode and 25.6 GHz for the nanosphere extensional mode) induced mainly by size distribution. The inset images are the SEM images of a single nanorod and nanosphere with a 25 nm scale bar. (b) Comparison of experimental data with theoretical predictions for different aspect-ratio gold nanorod samples.

Figure 3.4(a) shows the FWM signal of the 3.8 aspect-ratio nanorod sample collected by an APD as a function of the beat frequency between the ECL and DBR lasers. The background signal from Rayleigh scattering of the DBR laser was subtracted. Two acoustic resonance peaks were found at 20.0 GHz with a full width at half maximum (FWHM) of 4.0 GHz and 74.0 GHz with a FWHM of 20.0 GHz. The 20.0 GHz resonance corresponds to the frequency of the extensional mode of gold nanorods. For a cylindrical rod of a length L and a width W, the extensional and breathing mode frequencies in free space can be estimated by the following equations [7,94]:

$$\upsilon_{ext,r} = \frac{2n+1}{2L}\sqrt{\frac{E}{\rho}}, \tag{3.1}$$

$$\upsilon_{br,r} = \frac{\varphi v_l}{\pi W} \tag{3.2}$$

where the non-negative integer n is the extensional mode number (for the fundamental extensional mode, $n = 0$), E (42 GPa) is the Young's modulus along the long axis [95], ρ (19300 kg/cm^3) is the density of gold, v_l (3240 m/s) is the longitudinal sound velocity in gold [77], and φ (2.28 for the fundamental breathing mode) is an eigenvalue that depends on the transverse and longitudinal sound velocities in gold [96]. The calculated fundamental extensional mode frequency for a gold nanorod of a 38.2 nm length is 19.3 GHz, which is close to the experimental value 20.0 GHz. The size distribution of gold nanorods mainly contributes to the broadening of the resonance peak. The spectral linewidths of the lasers (DL100 Toptica Photonics and DBR852P Thorlabs) used are in the MHz range and so they contribute negligibly to the broadening. According to Equation 3.1 and assuming a Gaussian size distribution, FWHM can be calculated by:

$$\mathrm{FWHM} = \Delta\upsilon_{ext,r} = \frac{\Delta L}{L^2}\sqrt{\frac{E}{\rho}} = \frac{\Delta L}{L}\upsilon_{ext,r} \tag{3.3}$$

where ΔL = 2.355σ and σ is the standard deviation. The calculated FWHM is 3.6 GHz, which agrees well with the experimental FWHM of 4.0 GHz. The calculated fundamental breathing mode frequency for gold nanorods of 10.0 ± 1.0 nm width is 235.3 GHz with a FWHM of 55.4 GHz. However, we did not observe the breathing mode in that frequency range.

The 74.0 GHz resonance corresponds to the frequency of the extensional mode of gold nanospheres. For a sphere with a diameter *D*, the extensional and breathing mode frequencies in free space can be estimated by Lamb's theory [75]:

$$\upsilon_{ext,s} = \frac{\xi v_l}{\pi D}, \tag{3.4}$$

$$\upsilon_{ext,s} = \frac{\xi v_l}{\pi D} \tag{3.5}$$

where v_l (3240 m/s) is the longitudinal sound velocity in gold [77]. ξ (0.985 for the fundamental extensional mode) and η (2.945 for the fundamental breathing mode) are proportionality factors calculated by the equations derived in [76] under the free boundary condition. For gold nanospheres of 14.0 ± 2.1nm diameter, the calculated fundamental extensional mode frequency is 72.6 GHz with a 25.6 GHz FWHM, which agrees well with the experimental value of 74.0 GHz with a 20.0 GHz FWHM. We did not observe the breathing mode which should locate at 217.1 GHz with a 76.7 GHz FWHM based on Equation 3.5.

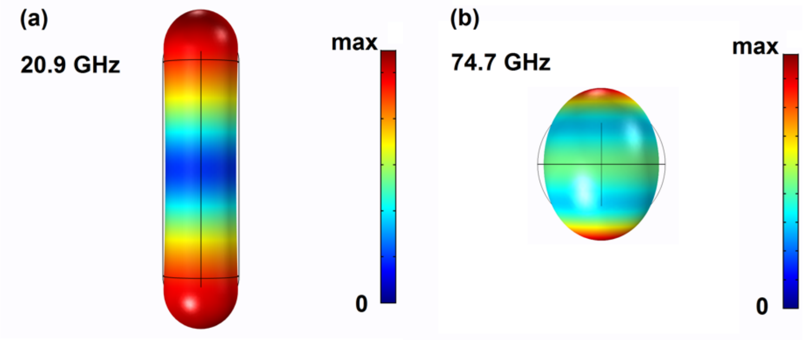

Figure 3.5 Displacements of the fundamental extensional modes. (a) Nanorod of 3.8 aspect ratio. (b) Nanosphere of 14 nm diameter.

We performed FWM measurements on different aspect-ratio gold nanorod samples (see A.2). Figure 3.4(b) shows the experimental data matches well with the theoretical predictions based on Equations 3.1 and 3.4. Numerical simulation for the extensional mode profiles were obtained by the finite element method (FEM) using a commercial FEM solver (COMSOL). Parameters used in the simulation are gold's Young's modulus of 42 GPa, Poisson's ratio of 0.43, density of 19300 kg/m^3 [77]. Figure 3.5 shows the displacements of the fundamental extensional modes of a single nanorod of 3.8 aspect ratio and a single nanosphere of 14 nm diameter, respectively. Tables 3.2 and 3.3 summarize the acoustic vibrational mode information of different nanorods and coexisting nanospheres, respectively. Calculations are based on the size information shown in Table 3.1.

	nanorod extensional mode (GHz)					nanorod breathing mode (GHz)	
	experiment		theory		simulation	theory	
aspect ratio	peak	FWHM	peak	FWHM	peak	peak	FWHM
3.8	20.0	4.0	19.3	3.6	20.9	235.3	55.4
4.0	18.9	5.7	18.0	3.4	19.4	230.6	53.3
4.3	16.5	4.2	16.3	3.2	17.6	224.1	55.3

Table 3.2. Fundamental acoustic vibrations of different aspect-ratio nanorods.

diameter (nm)	nanosphere extensional mode (GHz)					nanosphere breathing mode (GHz)	
	experiment		theory		simulation	theory	
	peak	FWHM	peak	FWHM	peak	peak	FWHM
14.0 ± 2.1	74.0	20.0	72.6	25.6	74.7	217.1	76.7
14.6 ± 2.2	69.2	23.5	69.6	24.7	71.6	208.1	73.8
15.5 ± 2.5	65.9	23.1	65.6	24.9	67.5	196.1	74.5

Table 3.3. Fundamental acoustic vibrations of coexisting nanospheres.

3.4 Discussion

The assignments of the FWM peaks to the corresponding vibrational modes were made based on best matches in theoretical analysis, and confirmed with SEM images. For 3.8 aspect-ratio nanorod sample, according to the resonant frequency and linewidth information from the FWM curve, calculations based on Equations 3.1 and 3.4 show that the nanorods have an average length of 36.9 ± 3.1 nm and the nanospheres have an average diameter of 13.7 ± 1.6 nm. Using the aspect ratio of 3.8 obtained from the extinction spectrum, the calculated width of the nanorods is 9.7 ± 0.8 nm. These values agree well with the experimental results shown in Table 3.1.

Disregarding nanoparticles of irregular shape in the sample, the relative concentrations of nanorods and coexisting nanospheres are around 80% and 20% of the total number of nanoparticles, respectively. The concentration difference may induce the intensity difference between the nanorod and the nanosphere extensional modes shown in Figure 3.4(a). Although the concentration ratio (nanorod/nanosphere) matches the FWM intensity ratio, we cannot exclude other factors that may cause the intensity difference, such as nanorod orientation in solution and LSPR difference.

Despite the small differences from the SEM imaging results, the FWM measurement shows the potential to acquire the size and distribution information of gold nanoparticles accurately. The FWM technique has its unique advantages, such as the ability of characterizing nanoparticles in solution compared to SEM or TEM which is difficult to image liquid samples. It should be noted that the reliance of the extinction spectrum to obtain the aspect ratio could be avoided if the nanorod breathing mode could be observed since the breathing mode provides the width information of nanorods. However, we did not observe the breathing mode in nanorods or coexisting nanospheres. The absence of the breathing mode might be caused by the failure of exciting the mode under current excitation condition. Higher laser power may be required to excite this breathing mode. However, we have maximized the laser power in the experiment. Therefore, we cannot prove our inference at the moment.

3.5 Summary

We used a FWM setup to investigate the acoustic vibrations of gold nanorods in aqueous solution. We obtained the size and distribution information based on the analysis of the vibrational modes. Good agreement was achieved between the calculated values and the experimental results obtained from SEM imaging, showing potential of the FWM method as an accurate and convenient tool for nanoparticle characterization in situ.

Chapter 4 Probing the Acoustic Vibrations of Complex-Shaped Metal Nanoparticles with Four-Wave Mixing

4.1 Introduction

Triangular and octahedral metallic nanoparticles have been used extensively in sensing, imaging, medicine, catalysis, photovoltaics, and non-linear optics [97 - 106]. The morphology of nanoparticles is of great importance in those applications. The study of the acoustic vibrations of metallic nanoparticles is crucial since it can provide information about nanoparticles' size, shape, and elastic properties [7-9]. The pump-probe spectroscopy is the typical technique used in the study [11-13]. In a pump-probe experiment, a pump pulse thermally excites the nanoparticles' vibrations and a probe pulse records the extinction change caused by the deformation of nanoparticles. High peak power of the pump laser is required for mode excitation and optical response detection. Nanoparticles of different shapes (e.g., spherical, rod-shaped, and cubic) and materials (gold and silver) have been studied using the pump-probe method [10,94,107].

Our reports on the acoustic vibrations of dielectric and metallic nanoparticles used four-wave mixing (FWM) to probe the acoustic vibrations and showed appreciable optical response and accuracy [29,33,108]. Hence, we use the FWM method to study triangular and octahedral nanoparticles' acoustic vibrations in this chapter. We observe two acoustic vibrational modes: an in-plane mode of nanoprisms with vertexial expansion and contraction; an extensional mode of nano-octahedrons with longitudinal expansion and transverse contraction. Numerical simulation has been performed to illustrate the mode profiles using the finite element method (FEM). We also investigate simple theoretical approximations, showing the inverse dependence of the mode frequency on the inverse of the edge length, for both nanoprisms and nano-octahedrons.

4.2 Experiments

4.2.1 Silver Nanoprisms Synthesis

Silver nanoprisms were synthesized by Ghazal Hajisalem following the photo-induced conversion method of silver nanospheres to nanoprisms [109]. As a typical synthesis process, an aqueous solution of silver nitrate (0.1 mM, 100 ml), (204390, Aldrich Chemicals), and trisodium citrate (0.3 mM), (S2990, ACP Chemicals Inc.), was prepared in presence of air with a moderate stirring rate (~120 rpm). Next, sodium borohydride solution (50 mM, 100 ml), (7420-1, Caledon Laboratories Ltd.), was injected to the system. Following this, Bis (p-sulfonatophenyl) phenylphosphine dehydrate dipotassium salt (BSPP) (5 mM, 2 ml), (698539, Aldrich Chemicals), was dropped into the solution over 2 min. BSPP was used as a stabilizer agent. The system was irradiated with a 24 W halogen lamp (ser. 700, Sunnex Inc.) for 60 h. During the synthesis process, we could observe the solution’s color change as an indicator. The clear initial solution of silver salt and citrate turned to yellow after the injection of the sodium borohydride, indicating the formation of silver nanospheres. During the irradiation process, the solution’s color turned to green and finally blue. The reaction was terminated after 60 h irradiation.

4.2.2 Gold Nano-Octahedrons Synthesis

Three different sizes of gold nano-octahedrons were synthesized. For gold nano-octahedrons with edge length larger than 50 nm, we used the method described in [110]. A volume of 10 mL of an aqueous solution containing 2.5×10^{-4} M hydrogen tetrachloroaurate trihydrate ($HAuCl_4{\cdot}3H_2O$, 99.9%, Aldrich) and 0.10 M cetyltrimethylammonium chloride (CTAC, 95%, TCI) was prepared. Concurrently, 10 mL of 0.02 M ice-cold sodium borohydride ($NaBH_4$, 98%, Aldrich) solution was made. To the $HAuCl_4$ solution was added 0.45 mL of the $NaBH_4$ solution with stirring. The resulting solution turned brown immediately, indicating the formation of gold particles. The seed solution was aged for 1 h at 30 ^oC. Two vials were labeled A and B. A growth solution was prepared in each of the two vials. First, 0.32 g of CTAC surfactant was added. The concentration of CTAC in the final solution was equal to 0.10 M. 9.47 mL deionized water was added to each vial. The vials were then kept in a water bath set at 30 ^oC. To both vials were added 250 μL of 0.01 M $HAuCl_4$ solution and 5 μL of 0.01 M KI. Finally, 220 μL of ascorbic acid was introduced for the synthesis of octahedrons. The total solution volume in each vial was 10 mL. The solution color turned colorless after the addition of ascorbic acid, indicating the reduction of Au^{3+} to Au^+ species. Next, 55 μL of the seed solution was added to the solution in vial A with shaking until the solution color turned light pink (~5 s). Then 55 μL of the solution in vial A was transferred to vial B with thorough mixing for ~10 s. The solution in vial B was left undisturbed for 15 min for particle growth and centrifuged three times at 3000 rpm for 10 min. The particles were concentrated to a 1 mL solution.

For nano-octahedrons with edge length smaller than 50 nm, we used the hydrothermal synthesis method [111] for shape maintaining. Briefly, 92 mL of ultrahigh purity water, 7.545 mL of 0.2 M cetyltrimethylammonium bromide (CTAB, Aldrich), 50 μL of 0.5 M $HAuCl_4$, and 0.1 M trisodium citrate ($Na_3C_6H_5O_7 \cdot 2H_2O$, Mallinckrodt) were added into a 350 ml glass container sealed with a cap. Then we added 630 and 690 μL of trisodium citrate to synthesize nano-octahedrons with side length of ~45 and ~35 nm, respectively.

Solutions are incubated in oven at 110 °C for 24 hours and cooled naturally down to room temperature. The cooled solutions were then centrifuged at 6000 rpm for 20 min to remove excess CTAB.

4.2.3 Instrumentation

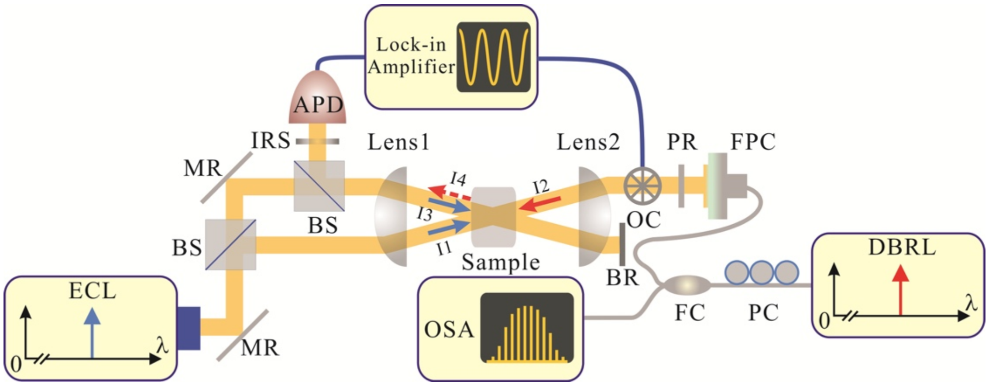

Figure 4.1. FWM experimental setup. ECL: external cavity laser; BS: beam splitter; MR: mirror; IRS: iris; APD: avalanche photodetector; DBRL: distributed Bragg reflector laser; PC: polarization controller; FC: fiber coupler; OSA: optical spectrum analyzer; BR: blocker; OC: optical chopper; PR: polarizer; FPC: fiber-port collimator.

Figure 4.1 shows the FWM experimental setup. The sample placed in a quartz cuvette was illuminated by the counter-propagating laser beams composed of a continuous-wave (CW) tunable external-cavity laser (ECL) (DL100, Toptica Photonics) and a CW tunable distributed Bragg reflector laser (DBRL) (DBR852P, Thorlabs). The setup has been fully described in section 3.2. Therefore, for simplicity, we do not give another description here.

4.3 Results and Discussion

4.3.1. Silver Nanoprisms Characterization with FWM

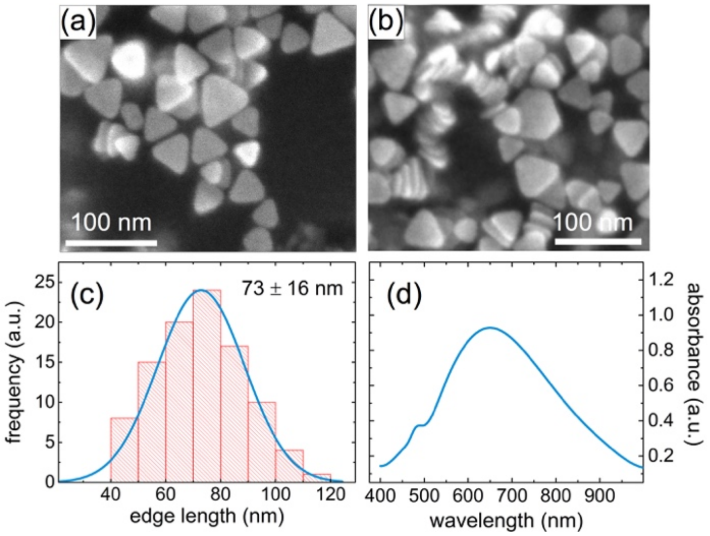

Figure 4.2. (a) SEM image of silver nanoprisms obtained at 300k× magnification. (b) SEM image of the nanoprism stacks for thickness estimation (~10 nm). (c) Nanoprisms' edge length distribution obtained by manually measuring 100 nanoprisms and fitted by Gaussian distribution. The error represents the standard deviation. (d) Extinction spectrum of silver nanoprisms in aqueous solution.

We first characterize the nanoprisms using SEM and extinction measurement. Figure 4.2(a) shows the SEM image of silver nanoprisms obtained at 2 kV and 300k× magnification. We manually measured the edge length of 100 nanoprisms from the SEM image to obtain the size distribution. The histogram was fitted by Gaussian distribution. The result shows that nanoprisms have an average edge length of 73 ± 16 nm. Figure 4.2(b) shows the SEM image of the nanoprism stacks for thickness estimation (~10 nm). Figure 4.2(d) shows the extinction spectrum of silver nanoprisms in aqueous solution. The extinction spectrum shows two localized surface plasmon resonance (LSPR) peaks: a

650 nm peak corresponding to the in-plane dipole plasmon resonance; a 490 nm peak corresponding to the in-plane quadrupole resonance [112].

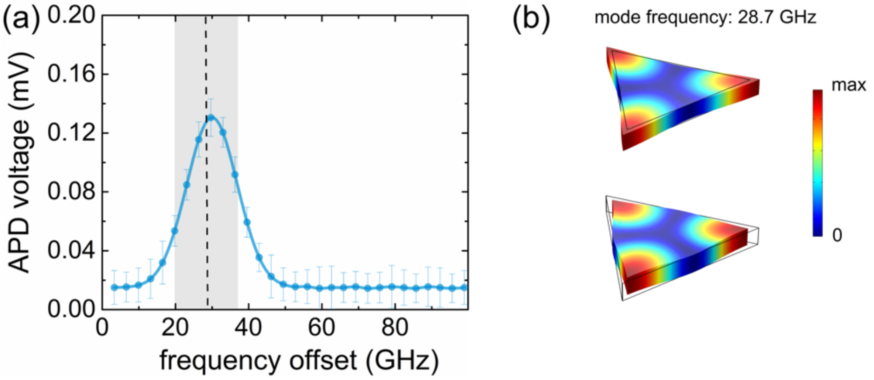

Figure 4.3. (a) FWM signal of the silver nanoprism sample as a function of the beat frequency between the ECL and DBR lasers. The error bar represents the standard deviation calculated by 148 data points at each beat frequency. The 29.7 GHz resonance peak corresponds to the frequency of the in-plane vibrational mode. The dashed line indicates the analytically calculated resonant frequency of 28.9 GHz according to the SEM result. The grey area indicates a 17.2 GHz broadening induced mainly by the size distribution. (b) Simulated mode profiles of maximal displacements with a mode frequency of 28.7 GHz within a vibrational cycle. The solid lines indicate the outlines of the undeformed nanoprisms.

Figure 4.3(a) shows the FWM signal of the silver nanoprism sample as a function of the beat frequency between the ECL and DBR lasers. The background signal from Rayleigh scattering of the DBR laser was subtracted. The spectrum shows one major acoustic resonance peak at 29.7 GHz with a full width at half maximum (FWHM) of 19.6 GHz. The resonant frequency of in-plane vibrational mode can be approximated by the equation [113]:

$$\upsilon_{prism} = \frac{V_{l,silver}}{\sqrt{3}L_{prism}} \tag{4.1}$$

where $V_{l,silver}$ (3650 m/s) is the longitudinal speed of sound in silver and L_{prism} is the edge length of nanoprisms. The calculated mode frequency for a silver nanoprism with a 73 nm edge length is 28.9 GHz, which is close to the experimental value (29.7 GHz). The size distribution mainly contributes to the broadening of the resonance peak. According to Equation 3.1 and assuming a Gaussian size distribution, FWHM can be calculated by:

$$\text{FWHM}=\Delta\upsilon_{prism} = \frac{\Delta L_{prism} V_{l,silver}}{\sqrt{3}L_{prism}^2} = \frac{\Delta L_{prism}}{L_{prism}}\upsilon_{prism}, \tag{4.2}$$

where $\Delta L_{prism} = 2.355\sigma_{prism}$ and σ_{prism} is the standard deviation of the edge length. The calculated FWHM is 17.2 GHz, which agrees well with the experimental FWHM of 19.6 GHz.

Figure 4.3(b) shows the mode profiles of maximal displacements within a vibrational cycle simulated by a commercial FEM solver (COMSOL). Parameters used in the simulation are silver's Young's modulus of 83 GPa, Poisson's ratio of 0.37, density of 10490 kg/m^3, edge length of 73 nm, and thickness of 10 nm [113]. The simulated mode frequency is 28.7 GHz, which is close to the experimental result (29.7 GHz). The mode profiles show an in-plane vibration with vertexial expansion and contraction.

4.3.2. Gold Nano-Octahedrons Characterization with FWM

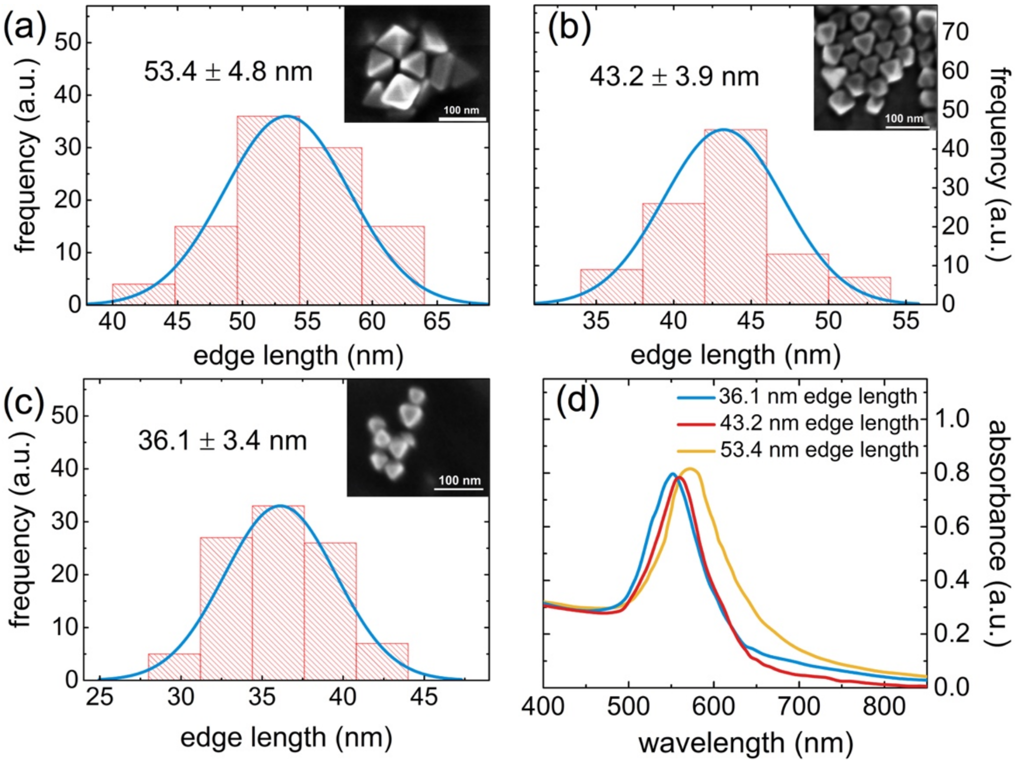

Figure 4.4. Edge length distribution of different size nano-octahedrons: (a) 53.4 nm average edge length. The inset shows the SEM image obtained at 350k× magnification; (b) 43.2 nm average edge length. The inset shows the SEM image obtained at 300k× magnification; (c) 36.1 nm average edge length. The inset shows the SEM image obtained at 300k× magnification. The edge length distribution is obtained by manually measuring 100 nano-octahedrons for each size and fitted by Gaussian distribution. The error represents the standard deviation. (d) Extinction spectra of different size nano-octahedrons in aqueous solution.

Figures 4.4(a)–(c) show the edge length distribution of nano-octahedrons with different sizes. We manually measured the edge length of 100 nano-octahedrons for each size from the SEM image to obtain the size distribution. The histogram was fitted by

Gaussian distribution. Figure 4.4(d) shows the extinction spectra of different size nano-octahedrons in aqueous solution. The extinction spectra show the major LSPR peaks at 551, 560, and 575 nm for 36.1, 43.2, and 53.4 nm nano-octahedrons, respectively. The LSPR corresponds to the in-plane (parallel to the symmetry plane that bisects the octahedron into two square pyramids) dipole resonance [114].

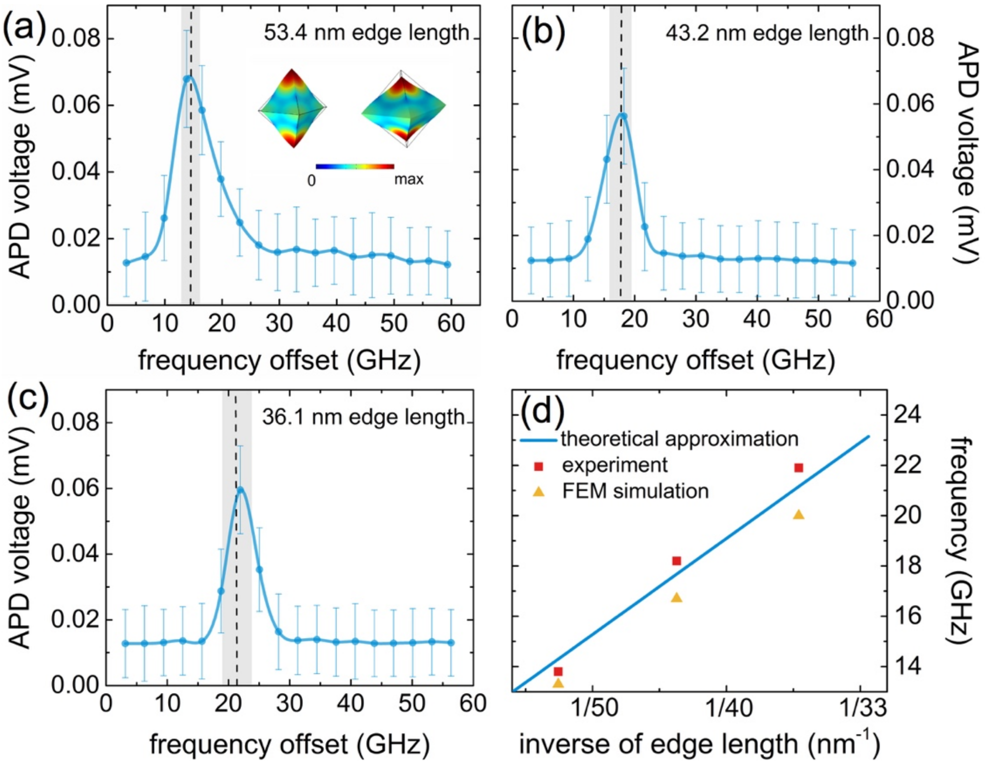

Figure 4.5. FWM signal of gold nano-octahedrons with different sizes: (a) 53.4 nm average edge length with a resonance at 13.8 GHz. The inset shows the simulated mode profiles of maximal displacements with a mode frequency of 13.3 GHz within a vibrational cycle. The solid lines indicate the outlines of the undeformed nano-octahedrons; (b) 43.2 nm average edge length with a resonance at 18.2 GHz; (c) 36.1 nm average edge length with a resonance at 21.9 GHz. The error bar represents the standard deviation calculated by 148 data points at each beat frequency. The dashed line indicates the theoretically calculated resonant frequency according to the SEM result. The grey

area indicates the broadening induced by the size distribution. (d) Inverse dependency of the mode frequency on the edge length.

Figure 4.5(a) shows the FWM signal of the gold nano-octahedron sample as a function of the beat frequency between the ECL and DBR lasers. The background signal from Rayleigh scattering of the DBR laser was subtracted. The spectrum shows an acoustic resonance peak at 13.8 GHz with a FWHM of 8.1 GHz. The resonant frequency of the vibrational mode can be approximated by the equation [115]:

$$\upsilon_{octahedron} = \frac{V_{l,gold}}{3\sqrt{2}L_{octahedron}} \tag{4.3}$$

where $V_{l,gold}$ (3240 m/s) is the longitudinal speed of sound in gold and $L_{octahedron}$ is the edge length of nano-octahedrons. The calculated mode frequency for a gold nano-octahedron with a 53 nm edge length is 14.4 GHz, which is close to the experimental value (13.8 GHz). Similar to Equation (4.2), the calculated FWHM is 3.2 GHz, which is much smaller than the experimental FWHM of 8.1 GHz. We also note that there is asymmetry in the lineshape. We do not have a suitable explanation for the increased linewidth and asymmetric lineshape observed. The inset shows the simulated mode profiles of maximal displacements within a vibrational cycle. Parameters used in the simulation are gold's Young's modulus of 42 GPa, Poisson's ratio of 0.43, density of 19300 kg/m^3, and edge length of 53 nm [7]. The simulated mode frequency is 13.3 GHz, which is close to the experimental result. The mode profiles show an extensional vibration of longitudinal expansion combined with transverse contraction and vice versa.

We also performed the FWM measurement on smaller nano-octahedrons as shown in Figures 4.5(b) and 4.5(c). The dashed line indicates the theoretically calculated resonant frequency according to the SEM result. The grey area indicates the broadening induced by the size distribution. We note that the asymmetry in the lineshape disappeared as the mode frequency increases. Figure 5(d) compares the experimental data with the theoretical approximation and the simulation result, validating the inverse dependency of the mode frequency on the edge length. The acoustic mode information of nano-octahedrons with different sizes is summarized in Table 4.1.

edge length (nm)	experiment (GHz)		theory (GHz)		FEM simulation (GHz)
	peak	FWHM	peak	FWHM	peak
53.4 ± 4.8	13.8	8.1	14.4	3.2	13.3
43.2 ± 3.9	18.2	5.9	17.7	3.7	16.7
36.1 ± 3.4	21.9	5.6	21.2	4.7	20.0

Table 4.1. Acoustic mode information of nano-octahedrons with different sizes

The FWM technique has two advantages over the extinction spectroscopy: more sensitive about the nanoparticle size and capable of providing the size distribution information. For example, with a 48% size change (36.1–53.4 nm) for nano-octahedrons, the FWM spectra show a 47% peak shift (21.2–14.4 GHz) compared to only a 4% peak shift (551–575 nm) in extinction spectra. The FWM linewidth can provide the size distribution information while the extinction linewidth cannot since the extinction linewidth (affected by nanoparticle's scattering and absorption) is mainly from the intrinsic homogeneous broadening. By contrast, the FWM linewidth is mainly from inhomogeneous broadening. Our previous FWM measurement on more homogeneous samples shows a much narrower linewidth [29]. Single nanoparticle acoustic vibrations have also been investigated using an optical tweezers setup and the result shows a very narrow linewidth as well [14]. These results imply that homogeneous broadening is negligible and the linewidth of the nanoparticle ensemble via FWM is from inhomogeneous broadening which is due to the size distribution.

4.4 Summary

In this chapter, we used the FWM setup to investigate the acoustic vibrations of nanoparticles of different shapes, sizes, and materials. We observed extensional modes of longitudinal expansion combined with transverse contraction from gold nanorods, gold nanospheres, and gold nano-octahedrons. We also observed silver nanoprisms’ in-plane vibrational mode with vertexial expansion and contraction. We illustrated the mode profiles by the FEM simulation. We investigated analytical approximations to the mode frequency. We found the linear dependence of the mode frequency on the inverse of nanoparticle’s dimension (e.g., rod’s length, sphere’s diameter, triangle and octahedron’s edge length).

Chapter 5 Monitoring Gold Nanoparticle Growth in situ via the Acoustic Vibrations Probed by Four-Wave Mixing

5.1 Introduction

This chapter investigates the performance of the four-wave mixing (FWM) setup on monitoring in situ gold nanoparticle growth in aqueous solution. Gold nanoparticles are commonly synthesized by the chemical reduction methods [37,116-118] (e.g., the citrate reduction method and the sodium borohydride reduction method). Parameters such as reaction temperature, reaction time, and reactant concentration need to be carefully controlled and adjusted in order to achieve fine tuning of nanoparticles' size and morphology [91,119-121]. The UV-vis spectroscopy, the scanning electron microscopy (SEM), and the transmission electron microscopy (TEM) are the common methods for nanoparticle characterization [122-124]. The UV-vis spectroscopy can achieve in situ monitoring the localized surface plasmon resonance (LSPR) band; however, the LSPR is strongly shape dependent with a much weaker size dependence [125]. For example, the LSPR remains at around 525 nm for gold spherical nanoparticles with diameter ranging from 5 to 25 nm [67]. Therefore, UV-vis spectroscopy is not favored to accurately monitor the nanoparticle size change during synthesis. Although SEM and TEM can accurately characterize nanoparticles, the instrumental limitations and cost present barriers to in situ monitoring of nanoparticles' size and morphology.

The acoustic vibrations of nanoparticles can provide information about the size, shape, and elastic properties [7-9]. Our previous works used four-wave mixing to probe the acoustic vibrations of dielectric and metallic nanoparticles [29,33,108]. The mode frequencies of nanoparticles show a strong dependence on the size, shape, and material, allowing us to monitor nanoparticle growth (mainly the size and distribution change) in situ. In this chapter, we use the FWM technique as an accurate and effective in situ monitoring method by synthesizing gold spherical nanoparticles using both the sodium borohydride reduction and the citrate reduction methods. The acoustic vibrations of nanoparticles are probed in situ with FWM and the size and distribution information are calculated based on the vibrational frequencies. The gold nanoparticles are also analyzed by SEM. The results obtained from FWM and SEM agree well, validating the accuracy of the FWM method as an in situ monitoring tool for nanoparticle growth.

5.2 Experiments

5.2.1 Gold Nanoparticle Synthesis

Gold nanoparticles were synthesized by reduction of tetrachloroauric acid at room temperature using sodium borohydride [126] and trisodium citrate [127], respectively. For the sodium borohydride reduction, 20 mL of 0.5 mM tetrachloroauric acid ($HAuCl_4.3H_2O$, 99.9+%, Aldrich) aqueous solution and 20 mL of 7.5 mM sodium borohydride ($NaBH_4$, 99.9+%, Aldrich) aqueous solution were prepared, respectively. The $HAuCl_4$ solution was stirred vigorously by a Teflon-coated magnetic bar at 1000 rpm speed. The $NaBH_4$ solution was quickly added to the $HAuCl_4$ solution. An immediate color change of the solution could be observed. The solution was stirred for 3 min until the color of the solution turned wine red. The sample was labeled as Sample 1 for further analysis. In order to tune the size of the nanoparticles, we adjusted the concentration of the $NaBH_4$ solution by preparing another two 20 mL $NaBH_4$ solutions with concentrations of 10 mM and 20 mM (labeled as Sample 2 and Sample 3, respectively), followed by the same synthesis process described above. Gold nanoparticles were immediately characterized in aqueous solution by the UV-vis spectroscopy and FWM after the synthesis completed.

For the trisodium citrate reduction, 20 mL of 0.5 mM $HAuCl_4$ solution and 20 mL of 5 mM trisodium citrate (Na_3Ct, 99+%, Biotech) solution were mixed as the growth solution and stirred by a Teflon-coated magnetic bar at 1000 rpm speed. The initial PH of the growth solution was adjusted to 7.2 by adding diluted NaOH solution. The color of the growth solution (pale yellow) gradually turned transparent, light pink after 2 h, and ruby-red after 24 h. FWM and UV-vis measurements were performed at certain intervals during the synthesis. In the meantime, samples from the growth solution were also drop-coated and quickly dried under nitrogen flow on a gold-coated slide (EMF Corp.) for SEM characterization.

5.2.2 Instrumentation

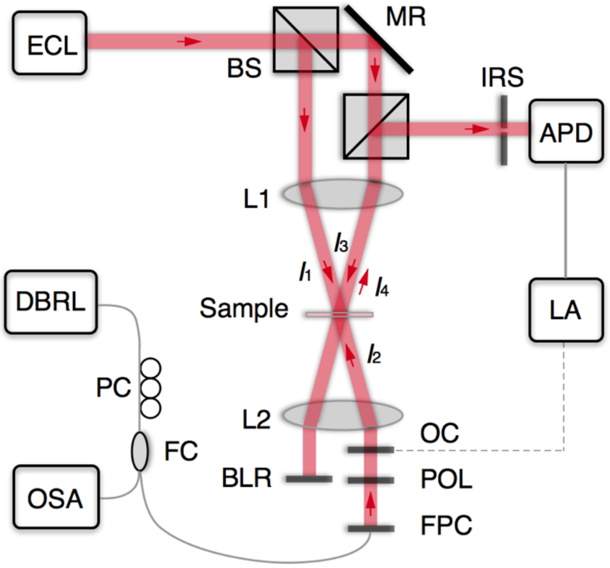

Figure 5.1. FWM setup. ECL: external cavity laser; DBRL: distributed Bragg reflector laser; OSA: optical spectrum analyzer; PC: polarization controller; FC: fiber coupler; BS: beam splitter; MR: mirror; IRS: iris; APD: avalanche photodetector; BLR: blocker; OC: optical chopper; PR: polarizer; FPC: fiber-port collimator.

Figure 5.1 shows the FWM setup. The gold nanoparticle solution was placed in a quartz cuvette. The sample was illuminated by two counter-propagating laser beams: a continuous-wave (CW) tunable external-cavity laser (ECL) (DL100, Topica Photonics) and a CW tunable distributed Bragg reflector laser (DBRL) (DBR852P, Thorlabs). The setup has been fully described in section 3.2. Therefore, for simplicity, we do not give another description here.

The UV-vis spectrum was obtained by measuring the transmission spectrum of the nanoparticle solution placed in the quartz cuvette using a white light source (LS-1-LL, Ocean Optics Inc.) and a spectrometer (a spectrometer (QE65000, Ocean Optics Inc.). It should be noted that the path length is the thickness of the quartz cuvette (1 mm), not the common path length (10 mm) in a standard UV-vis spectrometer. The SEM images of the nanoparticles were obtained by a Hitachi S-4800 field emission SEM at 2kV. Nanoparticles were drop-coated and dried on a gold-coated slide for SEM imaging.

5.3 Results and Discussion

5.3.1 $NaBH_4$ Reduction

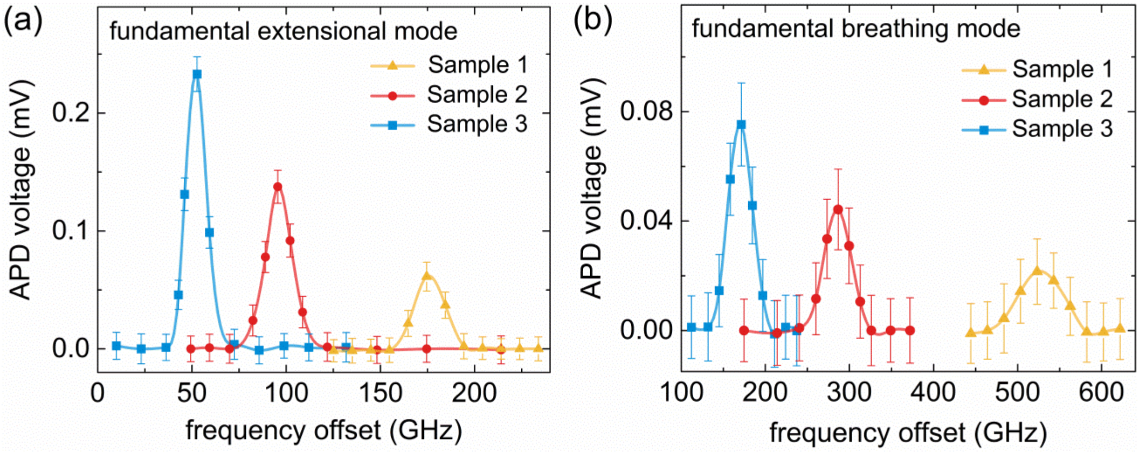

Figure 5.2. FWM signal of gold nanoparticles synthesized by $NaBH_4$ reduction as a function of the beat frequency between the ECL and the DBR lasers. (A) Fundamental extensional modes of gold nanoparticles with mode frequencies shifting from 174.6 GHz to 52.7 GHz as the average size of gold nanoparticles increases; (B) Fundamental breathing modes of gold nanoparticles with mode frequencies shifting from 523.1 GHz to 157.9 GHz as the average size of gold nanoparticles increases. The error bar represents the standard deviation calculated by 148 data points at each beat frequency.

Figure 5.2 shows the FWM signal of gold nanoparticles synthesized by $NaBH_4$ reduction as a function of the beat frequency between the ECL and the DBR lasers. The background signal from Rayleigh scattering of the DBR laser was subtracted. Two acoustic vibrations of gold nanoparticles were observed: a fundamental extensional mode with longitudinal extension and transverse contraction as shown in Figure 5.2(a); a fundamental breathing mode with radial extension and contraction as shown in Figure 5.2(b). We can estimate the nanoparticle diameter D and distribution based on the fundamental extensional mode frequency υ_{ext} and the fundamental breathing mode frequency υ_{br} [76]:

$$D = \frac{\xi v_l}{\pi \upsilon_{ext}} \tag{5.1}$$

$$D = \frac{\eta v_l}{\pi \upsilon_{br}} \tag{5.2}$$

where v_l (3240 m/s) is the longitudinal sound velocity in gold [77]. ξ (0.985 for the fundamental extensional mode) and η (2.945 for the fundamental breathing mode) are proportionality factors under the free boundary condition [76]. For example, the 52.7 GHz extensional mode corresponds to nanoparticles with a 19.3 nm average diameter according to Equation 5.1 while the 157.9 GHz breathing mode gives the similar result of a 19.2 nm average diameter according to Equation 5.2. The size distribution can be estimated from the full width at half maximum (FWHM) of the extensional mode $FWHM_{ext}$ and the FWHM of the breathing mode $FWHM_{br}$ based on Equations 5.1 and 5.2 and assuming a Gaussian size distribution:

$$\Delta D = \frac{\Delta \upsilon_{ext} \xi v_l}{\pi \upsilon_{ext}^2} = \frac{FWHM_{ext}}{\upsilon_{ext}} D \tag{5.3}$$

$$\Delta D = \frac{\Delta \upsilon_{br} \eta v_l}{\pi \upsilon_{br}^2} = \frac{FWHM_{br}}{\upsilon_{br}} D \tag{5.4}$$

where $\Delta D = 2.355\sigma$ and σ is the standard deviation. Table 5.1 summarizes the size and distribution results calculated based on the extensional and breathing modes, respectively.

	extensional (GHz)		size (nm) based on extensional modes	breathing (GHz)		size (nm) based on breathing modes
	peak	FWHM		peak	FWHM	
Sample 1	174.6	21.2	5.8 ± 0.3	523.1	51.6	5.8 ± 0.2
Sample 2	95.5	13.5	10.6 ± 0.6	286.4	39.0	10.6 ± 0.6
Sample 3	52.7	12.3	19.3 ± 1.9	157.9	35.0	19.2 ± 1.8

Table 5.1. Size information of nanoparticles synthesized by $NaBH_4$ reduction

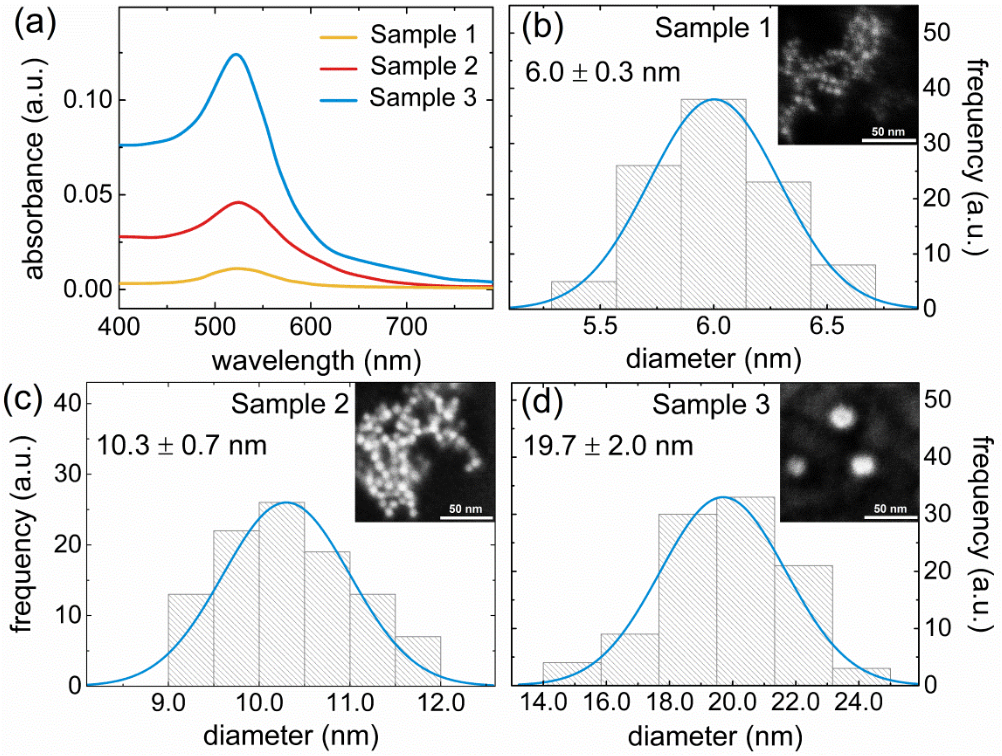

Figure 5.3. Gold nanoparticle (synthesized by $NaBH_4$ reduction) characterization by UV-vis spectroscopy and SEM. (a) Extinction spectra of different samples. All spectra show the same LSPR band at 524 nm. (b) Gaussian size distribution of Sample 1 with an average diameter of 6.0 nm and standard deviation of 0.3 nm. (c) Gaussian size distribution of Sample 2 with an average diameter of 10.3 nm and standard deviation of 0.7 nm. (d) Gaussian size distribution of Sample 3 with an average diameter of 19.7 nm and standard deviation of 2.0 nm. The size distribution is obtained by measuring 100 gold nanoparticles in each sample and fitted by the Gaussian distribution function. The insets are the SEM images of the corresponding samples obtained at 600k× magnification. The scale bar represents 50 nm length.

Figure 5.3 shows the characterization results of different samples synthesized by $NaBH_4$ reduction from UV-vis spectroscopy and SEM for verifying the accuracy of the FWM method for in situ monitoring gold nanoparticles' size and distribution. Figure 5.3(a) shows the extinction spectra of different samples. The extinction spectra show that the LSPR band does not shift with the nanoparticle size and remains at around 524 nm. It indicates that the UV-vis spectroscopy is not suitable for monitoring nanoparticle's size change during nanoparticle growth, especially for monitoring spherical nanoparticle growth. Figures 5.3(b)-(d) show the nanoparticle size distribution obtained by measuring 100 nanoparticles in each sample from the SEM images and fitted by the Gaussian distribution function. The results obtained from the SEM analysis agree well with the results obtained from the FWM characterization. This verifies the accuracy of the FWM method for in situ monitoring of both nanoparticle size and distribution.

5.3.2 Na_3Ct Reduction

The reduction of $HAuCl_4$ by $NaBH_4$ is a fast process for nanoparticle synthesis. Colloidal growth can complete within a few minutes and gold nanoparticles can remain stable during the following FWM characterization. To demonstrate the FWM method's applicability to slower synthesis monitoring, we performed in situ monitoring of nanoparticle growth using Na_3Ct reduction at room temperature. Figure 5.4 shows the FWM signal of the growth solution using Na_3Ct reduction as a function of the beat frequency between the ECL and the DBR lasers at certain intervals. The background signal from Rayleigh scattering of the DBR laser was subtracted. Both extensional modes (Figure 5.4(a)) and breathing modes (Figure 5.4(b)) shift as the growth time increases, indicating the gradual size growth of gold nanoparticles. The synthesis completed after

24 h as both extensional and breathing modes became stabilized with time. Table 5.2 summarizes the size and distribution results calculated based on the extensional and breathing modes, respectively.

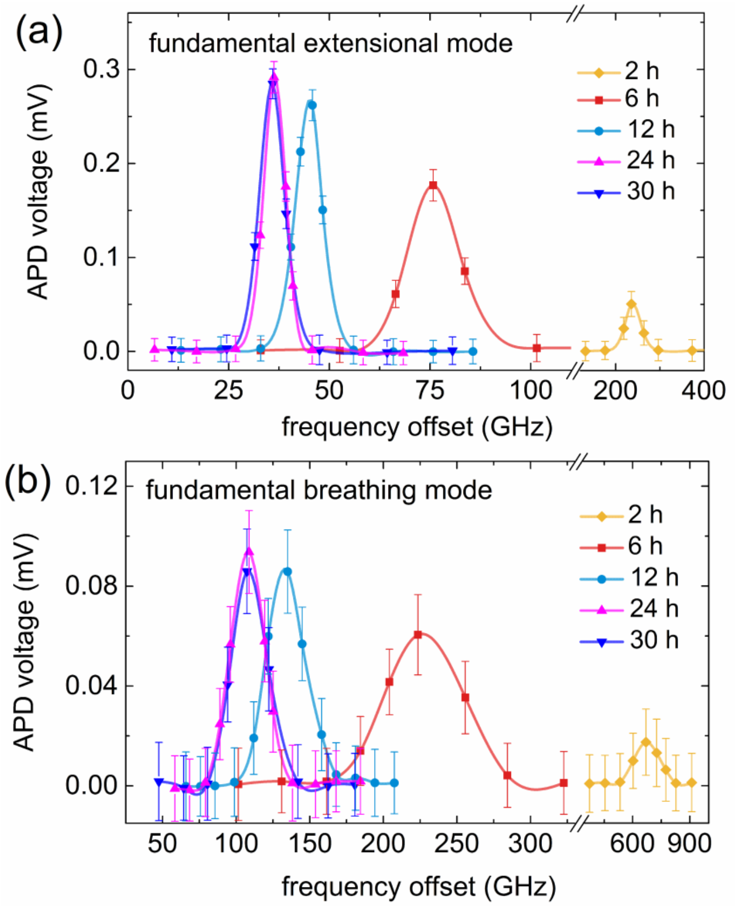

Figure 5.4. FWM signal of gold nanoparticles synthesized by Na_3Ct reduction as a function of the beat frequency between the ECL and the DBR lasers. (A) Fundamental extensional modes of gold nanoparticles with mode frequencies shifting from 236.1 GHz to 36.0 GHz as the average size of gold nanoparticles increases; (B) Fundamental breathing modes of gold nanoparticles with mode frequencies shifting from 675.2 GHz to 107.3 GHz as the average size of gold nanoparticles increases. The error bar represents the standard deviation calculated by 148 data points at each beat frequency.

growth time (h)	extensional (GHz)		size (nm) based on extensional modes	breathing (GHz)		size (nm) based on breathing modes
	peak	FWHM		peak	FWHM	
2	236.1	48.9	4.3 ± 0.4	675.2	162.9	4.5 ± 0.4
6	75.8	17.6	13.4 ± 1.3	223.9	56.0	13.6 ± 1.4
12	45.4	9.0	22.4 ± 1.9	135.1	31.1	22.5 ± 2.1
24	36.2	8.0	28.1 ± 2.6	108.7	27.5	28.0 ± 3.0
30	36.0	7.4	28.2 ± 2.5	107.3	27.4	28.3 ± 3.1

Table 5.2. Size information of nanoparticles synthesized by Na_3Ct reduction

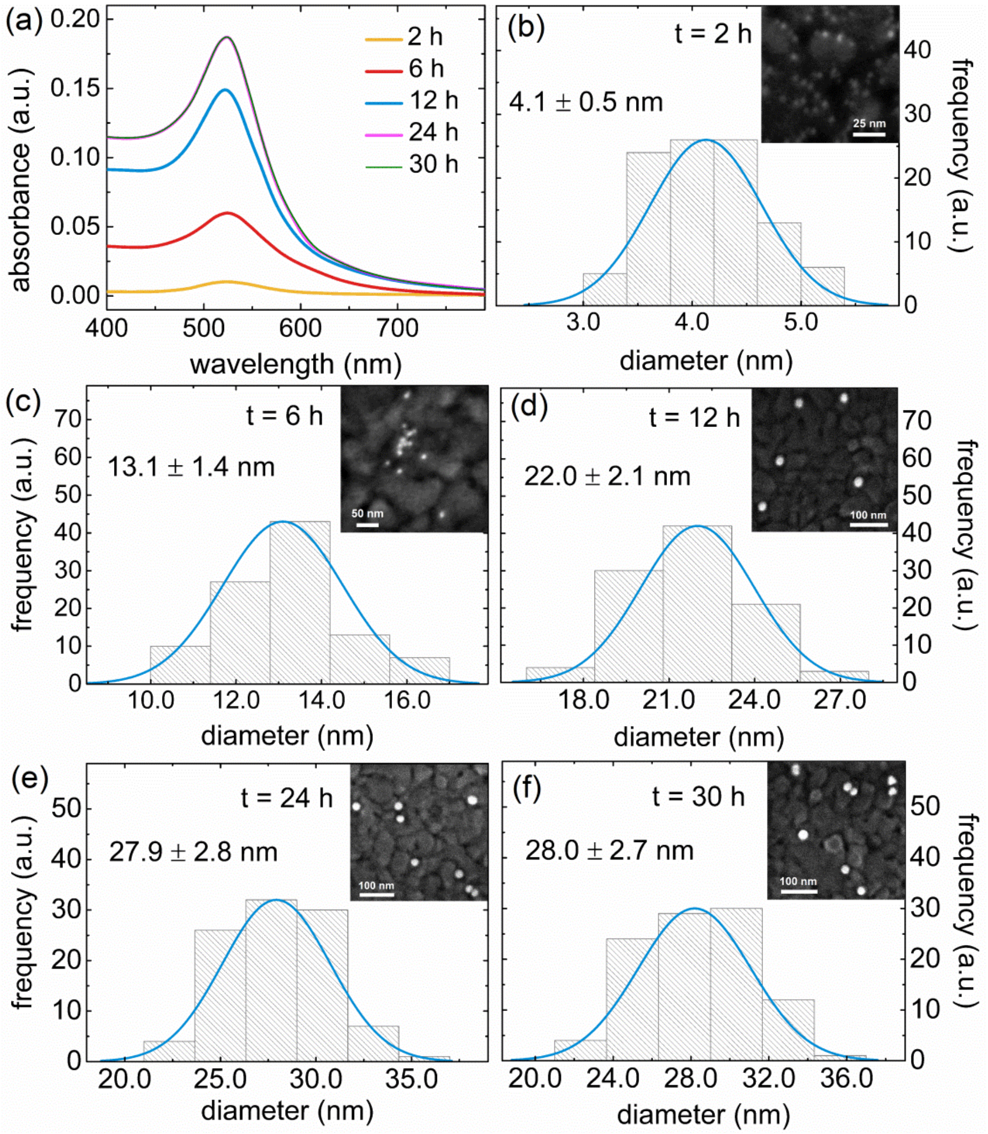

Figure 5.5. Gold nanoparticle (synthesized by Na_3Ct reduction) characterization by UV-vis spectroscopy and SEM. (a) Extinction spectra of the growth solution at certain intervals. (b)–(f) Gaussian size distribution of gold nanoparticles. The insets are the SEM images obtained at magnifications of 500k× for (b), 400k× for (c), 250k× for (d), 200k× for (e) and (f), respectively.

Figure 5.5 shows the UV-vis and SEM characterization of gold nanoparticles from the growth solution at certain intervals. The extinction spectra (Figure 5.5(a)) do not show an appreciable shift during the entire synthesis. Figures 5.5(b)-(f) show the nanoparticle size distribution obtained by measuring 100 nanoparticles from the SEM images and fitted by the Gaussian distribution function. Figure 5.6 shows that the nanoparticle size information obtained from the SEM analysis agrees well with the results obtained from the FWM measurements, verifying the accuracy of the FWM method for in situ monitoring of slow nanoparticle synthesis.

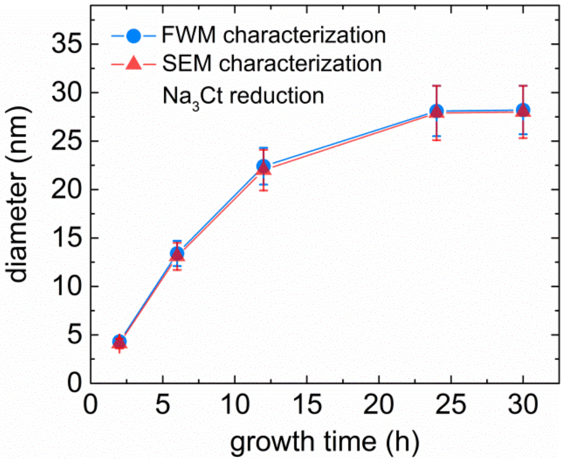

Figure 5.6. Nanoparticle size as a function of the growth time using Na_3Ct reduction at room temperature. The error bar stands for the standard deviation. Nanoparticle size

information obtained from the SEM analysis agrees well with the results obtained from the FWM measurements.

Although the acoustic vibrations of nanoparticles could be probed by other methods such as the low-frequency Raman [128] and the time-resolved spectroscopy [129], the FWM technique shows advantages in terms of resolution with regard to Raman, and simplicity with regard to the time-resolved spectroscopy (no ultrafast lasers or delay stages required). Compared to the limited applicability of Raman and time-domain methods in analysis of colloidal synthesis, our work establishes the use of the FWM technique for in situ monitoring of both fast and slow colloidal growth by probing the acoustic vibrations of nanoparticles. The FWM technique also presents features such as high accuracy and low cost with regard to the common characterization methods (extinction and TEM/SEM). The FWM technique provides not only the advantages of the accuracy of TEM/SEM, but also can be carried out in-situ with an optical arrangement similar to extinction measurements, with orders of magnitude higher accuracy in monitoring particle size.

5.4 Summary

Using a FWM setup to probe the acoustic vibrations of gold nanoparticles, the synthesis by the reduction of $HAuCl_4$ using $NaBH_4$ and Na_3Ct was monitored in situ, respectively. Two acoustic vibrational modes of gold nanoparticles were observed: an extensional mode with longitudinal expansion and transverse contraction; a breathing mode with radial expansion and contraction. The size and distribution information was calculated based on the two modes. We also characterized the gold nanoparticles by SEM. The results obtained from the SEM analysis agree well with the results from the FWM measurements, validating the FWM method as an accurate technique for in situ colloidal growth monitoring.

Chapter 6 Metallic Nanoparticles for Trace Cancer Biomarker Quantification Using Surface-Enhanced Raman Scattering

This chapter summarizes the work on developing metallic-nanoparticle-based substrates using surface-enhanced Raman scattering (SERS) for quantification of an exogenous cancer biomarker Acetyl Amantadine. The goal is to achieve high sensitivity and low limit of detection (LOD) (below 1 ng/mL [130]) with relatively low cost. This chapter presents the developing process step by step towards the goal. We first explore and investigate the commercial SERS substrates available in the market to check if these substrates could meet our requirement. By comparing the sensitivity and LOD, we conclude that the optimum substrate should be of large enhancement as well as high surface affinity to the analyte. Based on these two guidelines, we develop our own substrates using different nanoparticles combined with different surface functionalization methods. At the end of this chapter, we can achieve 0.4 ng/mL LOD.

6.1 Introduction

This section describes the process of synthesizing Acetly Amantadine (AcAm), experimental setup for extinction and Raman spectra acquisition, and methods for quantitative analysis of Raman spectra.

6.1.1 AcAm Synthesis

AcAm was synthesized by Wei Li following a previously developed protocol [131]. 2 g Amantadine (Tokyo Chemical Industry) was dissolved in 30 mL dichloromethane under nitrogen atmosphere. 3.77 g triethylamine was then added to the Am solution and stirred for 5 min. 2.17 g acetic anhydride was added to the mixture solution and stirred for 1 h. Water was added, and the aqueous layer was extracted using a separatory funnel. The combined organic extracts were dried over sodium sulfate, and then filtered. The mixture was concentrated to dryness on a rotary evaporator. High vacuum was applied to obtain AcAm as white solid form determined to be greater than 98% pure by 1H NMR analysis [132].

6.1.2 Experimental Setup

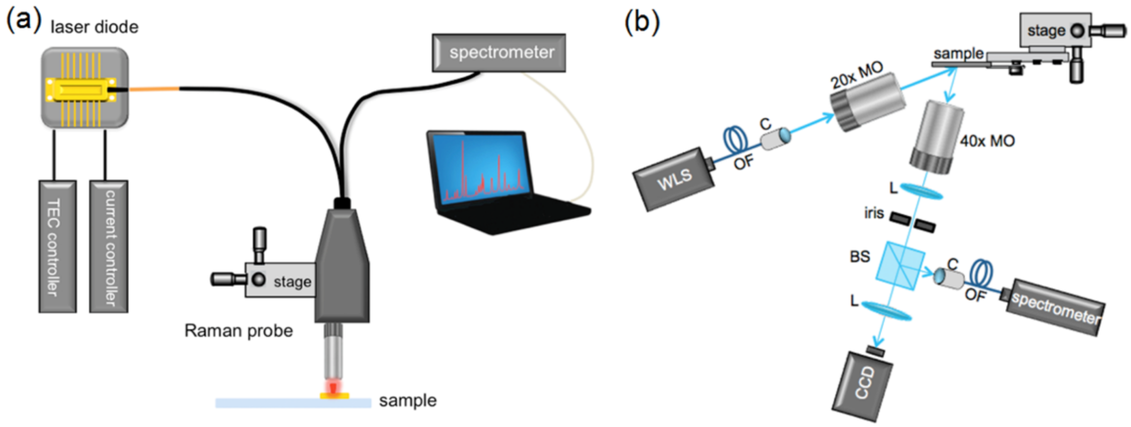

Figure 6.1. (a) Raman measurement setup. (b) DF scattering measurement setup. WLS = white light source, OF = optical fiber, C = collimator, MO = microscope objective lens, L = lens, BS = beam splitter.

Figure 6.1(a) shows the Raman measurement setup. A 785-nm fiber-coupled laser diode (Innovative Photonic Solution, 30 mW) was used for excitation. A portable Raman probe (InPhotonics) was used for excitation, collection, and filtering. A spectrometer (QE65 pro, Ocean Optics Inc.) was used for detection. The Raman probe was mounted on a 3-axis linear translation stage for fine adjustment. 16 spectra were acquired for each sample at different random locations with 30 s integration time and 5 scans-to-average for each spectrum.

Figure 6.1(b) shows the dark-field (DF) scattering measurement setup. A collimated white light source (LS-1-LL, Ocean Optics Inc.) was focused onto the sample by a 20 × microscope objective (0.42 NA, Mitutoyo Plan Apo) at 70° to the surface normal. The off-normal configuration has been used to excite the LSPR of the nanoparticle-metal film [133]. The scattered light from the sample was collected at 15° to the surface normal by a 40 × microscope objective (0.68 NA, Zeiss). The scattered beam was split into two beams by a 50-50 beam splitter. One beam was directed into a CCD camera (GC660, Allied Vision Technologies) to take the DF scattering image. The other beam was directed into a spectrometer (QE65000, Ocean Optics Inc.) to take the DF scattering spectrum.

A scanning electron microscopy (SEM) image of the sample was obtained using a Hitachi S-4800 field emission SEM. UV-visible extinction measurements of the gold nanorods solution were acquired using a SpectraMax M5 multi-mode microplate reader.

6.1.3 Methods for Quantitative Analysis of Raman Spectra

We follow the standard procedure to post-process Raman spectra. The fluorescent background should be subtracted first to obtain the real Raman signal. The sum of all characteristic peak intensities of the analyte represents the final Raman intensity at certain concentration. We plot Raman intensity vs. concentration curve to calculate the sensitivity and LOD.

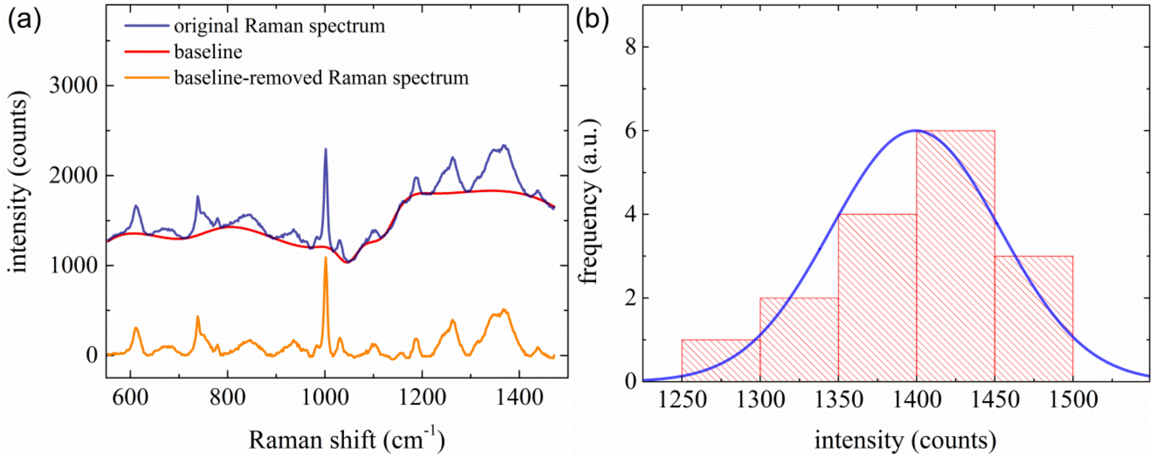

Figure 6.2. (a) Baseline subtraction of Raman spectra. (b) Raman intensity distribution.

Figure 6.2(a) shows the baseline subtraction process. The fluorescence background is subtracted by the spline interpolation method, which generates the background curve by the cubic spline interpolation along the dip points in the original Raman spectrum. It can be seen that baseline subtraction effectively reduces the background signal. Figure 6.2(b) shows the summed Raman intensity distribution. We use Gaussian distribution to approximate this distribution and calculate the mean value and the standard error for further quantitative analysis.

6.2 Commercial SERS Substrates Investigation

6.2.1 Klarite Substrates

Figure 6.3 shows the SEM images of the commercial Klarite substrate. The substrate is essentially an array of gold-coated inverted pyramids fabricated on a silicon wafer. The inverted pyramid structure has a ~ 2 μm period and ~ 1 μm depth. Strong enhancement can be achieved due to the localized surface plasmon resonance (LSPR) in the pits.

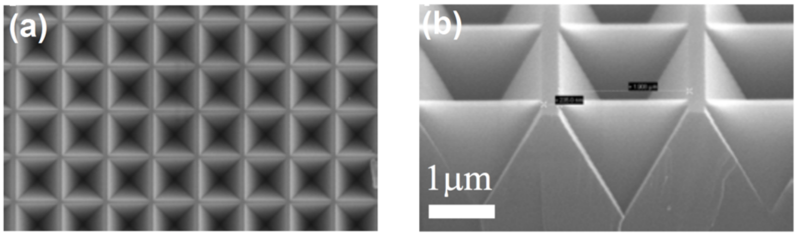

Figure 6.3. SEM images of Klarite substrates. (a) Top view. (b) Cross section [134].

We performed SERS measurements on AcAm solutions using Klarite substrates. AcAm was dissolved in methanol solution (10% methanol with 90% water, volume ratio) at varying concentrations from 0 ng/mL (the blank control) to 10000 ng/mL. The Klarite substrate was dipped in the AcAm solution for 0.5 h, then dipped in DI water for a quick wash, and dried in the air for further measurements.

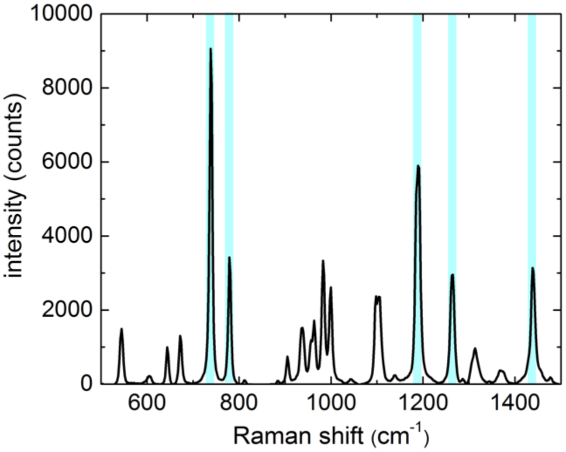

Figure 6.4. Raman spectrum of AcAm powder. The characteristic peaks are highlighted in cyan.

Figure 6.4 shows a representative Raman spectrum of AcAm powder. The characteristic peaks of AcAm (738 cm^{-1}, 779 cm^{-1}, 1189 cm^{-1}, 1265 cm^{-1}, and 1438 cm^{-1}) are highlighted in cyan. We focus on these five strongest Raman peaks for quantitative analysis through this chapter.

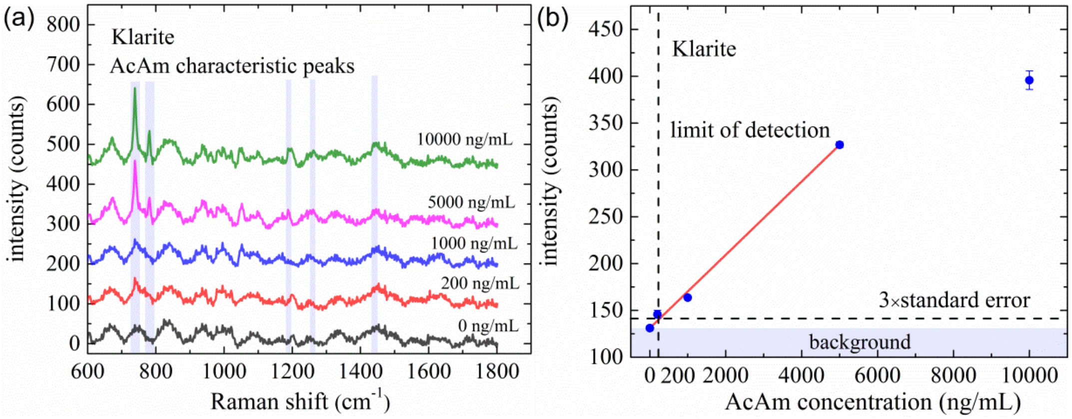

Figure 6.5. (a) Averaged Raman spectra of samples prepared with different AcAm concentrations. AcAm characteristic peaks are highlighted in purple. (b) Raman intensity (summed over the 5 selected AcAm peaks) as a function of the AcAm concentration.

Figure 6.5(a) shows the averaged Raman spectra of samples prepared with different AcAm concentrations. AcAm characteristic peaks are highlighted in purple. Figure 6.5(b) shows the Raman intensity (summed over the 5 selected AcAm peaks) as a function of the AcAm concentration. The noise level highlighted in purple is the intensity of the blank sample. The red line is the linear fit of the linear region. The sensitivity is the slope of the straight line which is 0.04 counts/(ng/mL). 200 ng/mL of LOD is indicated by the dashed line. The intensity level of LOD equals the noise level plus three times of the standard error of the blank sample. The error bar of each data point stands for the standard error of the mean.

6.2.2 Metal-Coated Silicon Nanopillar Substrates

Figure 6.6 shows the SEM images of the metal-coated silicon nanopillar substrates. These substrates are fabricated using maskless reactive ion etching on silicon wafers, followed by metal (gold or silver) deposition. After immersion in the analyte solution, leaning effect occurs when the solvent evaporates as shown in Figure 6.6(b). Analyte molecules adsorbed on the tips can experience large enhancement due to the hot spots where the pillars lean together.

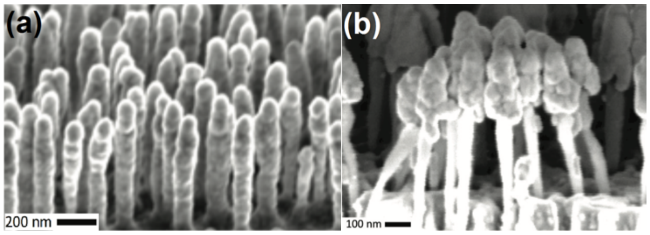

Figure 6.6. SEM images of metal-coated silicon nanopillar substrates. (a) Before immersion in the analyte solution. (b) Pillars leaning together after the solvent evaporates [135].

We performed SERS measurements on AcAm solutions with varying concentrations from 0 ng/mL (the blank control) to 10000 ng/mL. The substrate was dipped in the AcAm solution for 0.5 h, then dipped in DI water for a quick wash, and dried in the air for further measurements.

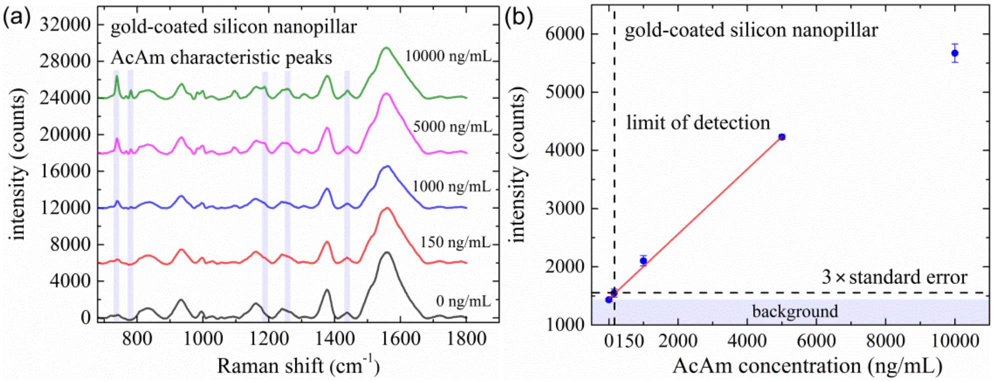

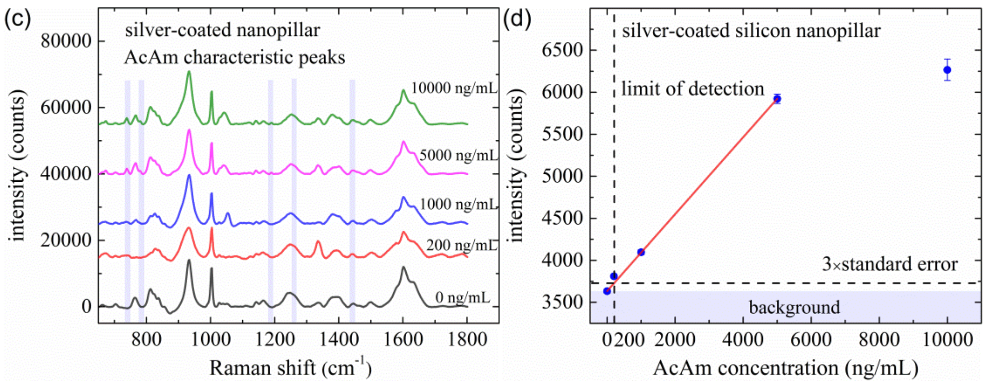

Figure 6.7. (a) Averaged Raman spectra of samples prepared with different AcAm concentrations using gold-coated silicon nanopillar substrates. AcAm characteristic peaks are highlighted in purple. (b) Raman intensity (summed over the 5 selected AcAm peaks) as a function of the AcAm concentration. (c) Averaged Raman spectra of samples prepared with different AcAm concentrations using silver-coated silicon nanopillar substrates. AcAm characteristic peaks are highlighted in purple. (d) Raman intensity (summed over the 5 selected AcAm peaks) as a function of the AcAm concentration.

Figure 6.7(a) shows the averaged Raman spectra of the sample prepared with different AcAm concentrations using gold-coated silicon nanopillar substrates. AcAm characteristic peaks are highlighted in purple. Figure 6.7(b) shows the Raman intensity (summed over the 5 selected AcAm peaks) as a function of the AcAm concentration. The noise level highlighted in purple is the intensity of the blank sample. The red line is the linear fit of the linear region. The sensitivity is the slope of the straight line which is 0.56 counts/(ng/mL). 150 ng/mL of LOD is indicated by the dashed line. Figure 6.7(c) shows the averaged Raman spectra of the sample prepared with different AcAm concentrations using silver-coated silicon nanopillar substrates. AcAm characteristic peaks are highlighted in purple. Figure 6.4(d) shows the Raman intensity (summed over the 5 selected AcAm peaks) as a function of the AcAm concentration. The noise level highlighted in purple is the intensity of the blank sample. The red line is the linear fit of the linear region. The sensitivity is the slope of the straight line which is 0.46 counts/(ng/mL). 200 ng/mL of LOD is indicated by the dashed line.

6.2.3 Comparison

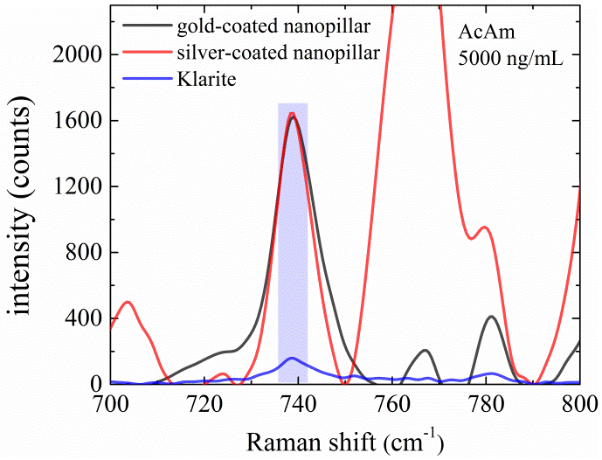

Figure 6.8. Comparison of the enhancement between different SERS substrates. The AcAm characteristic peak is highlighted in purple.

Figure 6.8 compares the enhancement between different SERS substrates. For simplicity, we only focus on the strongest AcAm peak which is highlighted in purple. The intensity shows that the enhancement from the metal-coated nanopillar substrates is 10 times larger than the Klarite substrate, which is consistent with the result that the sensitivity of the metal-coated nanopillar substrates is 10 times larger than the Klarite substrate. However, LODs of these substrates are similar because LOD is also determined by the noise level which relates to the uniformity of the substrate. Thus, we can conclude a general guideline for designing good SERS substrates. To increase the sensitivity, enhancement from the substrate should be improved as well as the surface affinity for more analyte adsorption. To decrease the LOD, increase the sensitivity and maintain or even improve the uniformity of the substrate. Nonetheless, sensitivity improvement is always of top priority.

6.3 Polystyrene-Functionalized Gold Nanorods

Although the metal-coated nanopillar substrates can provide high enhancement, it is impractical to functionalize the metal surface due to the leaning effect, hence hindering the further sensitivity improvement. Inspired by the mechanism of the enhancement from the LSPR of metal nanostructures, we therefore consider using gold nanorods since they are suitable as SERS substrates [136, 137]. In this section, we investigate the use of gold nanorods to quantify AcAm in solution. We functionalize nanorods' surface with polystyrene, and use the hydrophobicity of the polystyrene as a more general binding agent that effectively collects AcAm from solution. We present quantitative analysis of the Raman spectra and the LOD of the platform.

6.3.1 Gold Nanorods Synthesis

Gold nanorods were synthesized by Ariella Lukach using the seed-mediated growth method [138]. Briefly, seed nanoparticles were synthesized by mixing $HAuCl_4$ solution (0.12 mL, 15 mM) with an aqueous solution of hexadecyltrimethylammoniumbromide (CTAB) (2.5 g, 0.20 M), 1 mL of deionized water, and 0.60 mL of ice-cold 0.010 M $NaBH_4$. The growth solution was prepared by mixing CTAB solution (5.36 g, 0.20 M), 4 mL deionized water, $AgNO_3$ (0.4 mL, 4 mM), $HAuCl_4$ (0.5 mL, 15 mM), ascorbic acid (0.124 mL, 0.0788 M), and 0.1 mL of the 45-min aged seed solution. The growth solution turned from colorless to reddish brown following incubation overnight at 27 °C. The concentrated nanorods were then sonicated with 0.2 mg thiol-terminated polystyrene (Polymer Source Inc.) in 1 g tetrahydrofuran (THF) for 30 min to initiate the exchange of

CTAB ligands starting at the nanorod ends with polystyrene. After incubation overnight at room temperature, nanorods were purified by eight centrifugation cycles at 9000 rpm for 30 min to remove excess polystyrene. The concentrated polystyrene-functionalized gold nanorods were then redispersed in THF to form a stock solution.

6.3.2 Sample Preparation

Gold nanorods were first dried from the stock solution and then re-dissolved in acetone (absorbance 0.92 at 760 nm). AcAm was dissolved in acetone at varying concentrations from 400 ng/mL to 10 μg/mL. 10 μL AcAm solution was added to 240 μL deionized water in a glass insert (300 μL size, Sigma Aldrich) with resultant concentrations from 0 ng/mL to 400 ng/mL. 50 μL NR solution was then added to the diluted AcAm solution. The mixture solution was sonicated for 5 min for thorough mixing. The solution was then incubated for 6 h at room temperature for the AcAm adsorption. After 20 min centrifugation at 6000 rpm, the subnatant was drop-coated onto a commercial gold-coated slide (EMF Corp.) for further characterization and Raman measurement.

6.3.3 Results and Discussion

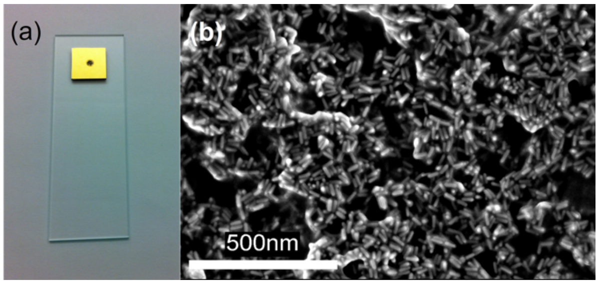

Figure 6.9. (a) The prepared sample picture. The dried gold nanorods are located at the center of the gold-coated slide. The diameter of the spot is about 5 mm. (b) SEM image of the dried gold nanorods.

Figure 6.9(a) shows a picture of the prepared sample for detection. The dried gold nanorods are located at the center of the gold-coated slide. The diameter of the spot is about 5 mm. Figure 6.9(b) shows the SEM image of the dried gold nanorods. SEM imaging was carried out at 2 kV, which is suitable for imaging gold materials. The SEM image shows the nanorods are aggregated with random orientation in the dried spot. Nominally, these nanorods have a length of around 37 nm and a diameter of around 10 nm. The aspect ratio is therefore around 3.7.

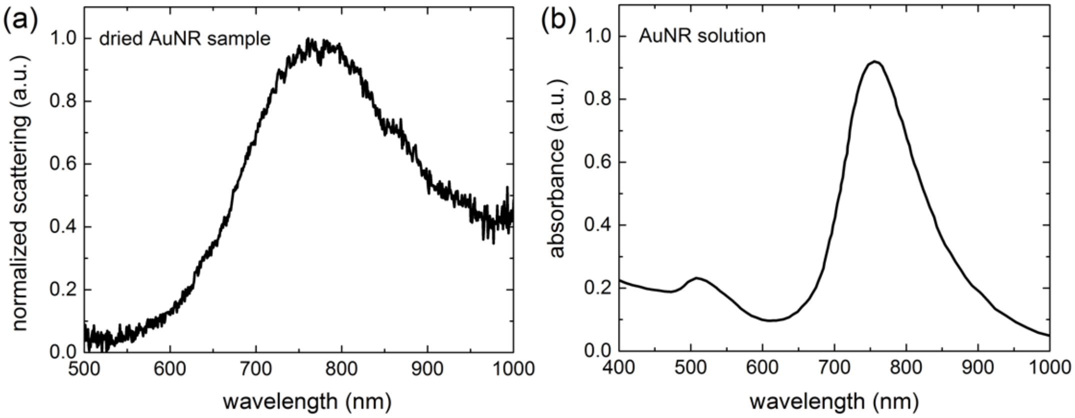

Figure 6.10. (a) Normalized DF scattering spectrum of the dried gold nanorod sample. The LSPR peak is located at 775 nm. (b) UV-visible absorbance spectrum of the gold nanorod solution. The longitudinal LSPR peak is located at 760 nm.

Figure 6.10(a) shows the normalized DF scattering spectrum of the dried nanorod sample. The spectrum shows a LSPR peak around 775 nm. The Raman excitation wavelength 785 nm is close to the LSPR wavelength, thereby enhancing coupling and the Raman signal. Figure 6.10(b) shows the UV-visible absorbance spectrum of the nanorod solution for comparison. The longitudinal LSPR peak is located at 760 nm. There is a 15-nm red shift of the LSPR peak of the dried nanorod sample compared to the dispersed nanorod solution. The shift may come from the coupling between the nanorods in the aggregate and the presence of the gold-coated slide [139]. The aspect ratio of individual nanorods is the key parameter in achieving high SERS response from the aggregate. Our SERS study on the CTAB Raman modes of the aggregated CTAB-coated nanorods confirmed that the enhancement of the CTAB Raman signal can be enhanced by tuning the aspect ratio of individual nanorods to the value used in the present work.

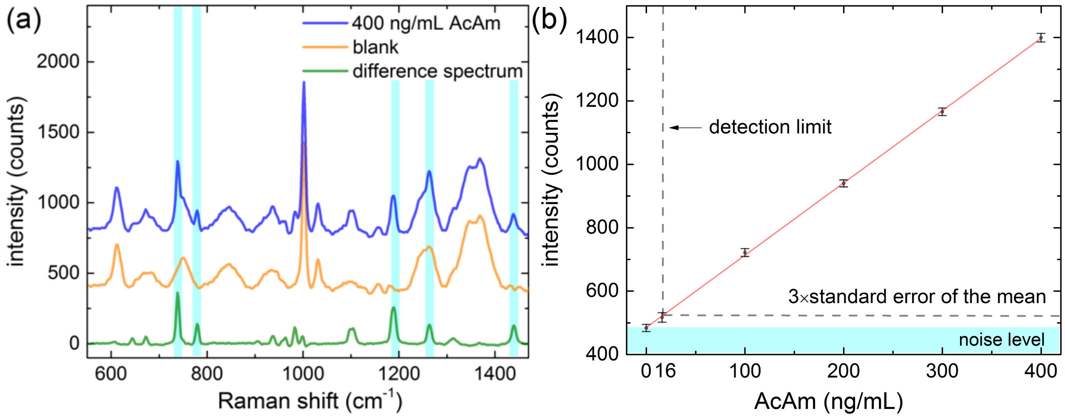

Figure 6.11. (a) Averaged Raman spectra of the sample prepared with 400 ng/mL AcAm, the blank sample without AcAm, and their difference spectrum (400 ng/mL AcAm – blank). (b) Raman intensity (summed over the 5 selected AcAm peaks) as a function of the AcAm concentration.

Figure 6.11(a) shows the averaged Raman spectra of the sample prepared with 400 ng/mL AcAm, the blank sample without AcAm, and their difference spectrum (400 ng/mL AcAm – blank). Baselines of the Raman spectra were corrected by the spline interpolation method described in section 4.1.3. The characteristic peaks (e.g., 1002 cm^{-1}) in the blank spectrum belong to the polystyrene. The ripple-like features (e.g., 700 cm^{-1} to 900 cm^{-1}) come from the etaloning effect caused by a cavity formed between the CCD detector in the spectrometer and the substrate and therefore are spurious features [140].

The difference spectrum shows a good match to the spectrum of the AcAm powder, which reduces the etaloning and the background signal from the polystyrene.

Figure 6.11(b) shows a linear relation of the Raman intensity versus the AcAm concentration. The Raman intensity was calculated by summing the intensity values of the five characteristic peaks. The error bar of each data point stands for the standard error of the mean. Since each spectrum is averaged by 5 scans, it should have its own uncertainty. However, we did not implement the propagation of uncertainty in the final error calculation and relied solely on statistical analysis over multiple spectra. There are clear advantages of using more than one peak in quantification: more photon signal is acquired by multiple Raman peaks and the signal is spectrally distributed (i.e., less susceptible to local spectral artifacts – such as the polystyrene in this case). This supervised quantification method is effective for our application because the AcAm is the only analyte in our case. More sophisticated and unsupervised methods such as principal component analysis (PCA) and partial least squares (PLS) can be applied to multi-analyte situations [141, 142], but we do not attempt those here. The noise level highlighted in cyan is the intensity of the blank sample. The intensity level of the detection limit (16 ng/mL) equals the noise level plus three times of the standard error of the blank sample, which is close to the clinical threshold value (10 ng/mL) for a positive test in urine of North American subjects [143]. We use the standard error as opposed to the standard deviation in deducing the detection limit because each time we measure 16 spectra and use the mean value of the intensity to determine the AcAm concentration, rather than just measuring one single spectrum. Our analysis has confirmed that the data samples are well-fit to Gaussian distributions (shown in section 6.1.3). Therefore, it is more appropriate to use the standard error of the mean to estimate the degree that the sample mean differs from the population mean than to use the standard deviation, which is used to estimate the degree that an individual value within the sample differs from the sample's mean. It should be noted that the detection limit could be improved by increasing the number of spectra obtained from one sample (equivalent to increasing the integration time), since the noise goes down as the square root of the number of spectra. But there is a trade-off between the detection limit and the acquisition time. For example, in principle the detection limit of 10 ng/mL could be achieved by increasing the number of spectra to 41, but this would almost triple the acquisition time. We chose 16 as the number of spectra to combine the promising detection limit and the reasonable acquisition time.

6.3.4 Conclusion

We presented a method for quantifying an exogenous cancer biomarker AcAm using polystyrene functionalized gold nanorods as a SERS substrate, and multi-peak analysis for quantification. We achieved a detection limit of 16 ng/mL, which is promising for future clinical adoption.

6.4 Beta-Cyclodextrin-Functionalized Gold Nanospheres

In order to increase adsorption of analyte molecules onto the metal surface, surface functionalization with higher affinity to the analyte should be used. In this section, we demonstrate the quantification of AcAm using beta-cyclodextrin (β-CD)-functionalized gold nanospheres as the SERS platform. We utilize the β-CD cavity to capture the hydrophobic AcAm molecule from solution, followed by drying and detection using SERS. This platform shows better sensitivity (7 times higher) and estimated lower per-sample cost (1/10th) than the commercial Klarite platform using the same surface functionalization method. We achieve a detection limit of 0.4 ng/mL (2.1 nM), showing potential for fast and low-cost early cancer detection.

6.4.1 Gold Nanospheres Functionalization and Sample Preparation

1 mL mono-6-thiol-beta-cyclodextrin (HS-β-CD) aqueous solution (Shandong Zhiyuan Bio-Technology, 20 μM) was added to 2 mL gold nanosphere solution (BBI Solutions, 60 nm, 43 pM), followed by 5 min sonication for thorough mixing. The mixture solution was incubated for 12 h in a darkroom at room temperature. During the incubation, the thiolated cyclodextrins attached to the gold nanosphere surface due to the strong sulfur-gold bond [144]. The nanospheres were then purified by three centrifugation cycles at 10000 rpm for 30 min to remove excess HS-β-CD. The concentrated β-CD-functionalized nanospheres were then redispersed in deionized water to 1 mL to form a stock solution.

AcAm was dissolved in methanol solution (10% methanol : 90% water, volume ratio) at varying concentrations from 0 ng/mL to 20 ng/mL. 0.1 mL nanosphere stock solution was added to 1 mL AcAm solution and incubated for 4 h in a darkroom at room temperature for the AcAm adsorption. Different incubation times were investigated in [145]. 4 h was verified to be sufficient to form β-CD inclusion with AcAm in solution, since the Raman intensity of AcAm became saturated when the incubation time exceeded 4 h. After 20 min centrifugation at 6000 rpm, the subnatant (around 5 μL) was drop-coated onto a commercial gold-coated slide (EMF Corp.) and dried in the air at room temperature for further characterization and SERS measurement.

6.4.2 Results and Discussion

Figures 6.12(a) and 6.12(b) show the scanning electron microscopy (SEM) images of the dried *β*-CD functionalized gold nanosphere sample. SEM imaging was carried out at 2 kV, which is suitable for imaging gold materials. The nanospheres have an average diameter of 60 nm. The SEM images show the nanospheres are highly aggregated in the dried sample. Figure 6.12(c) shows the illustration of the dried *β*-CD functionalized gold nanosphere aggregate. Hot spots are formed between the adjacent nanospheres [146-148]. AcAm captured by the *β*-CD encapsulation situated in the hot spots will experience strong Raman enhancement due to the strong coupling resonance. It should be noted that the nanosphere film is not a monolayer. According to the amount of the nanospheres (around 5×10^9) and the size of the dried spot (around 4 mm diameter), we can roughly estimate the film has three layers of nanospheres.

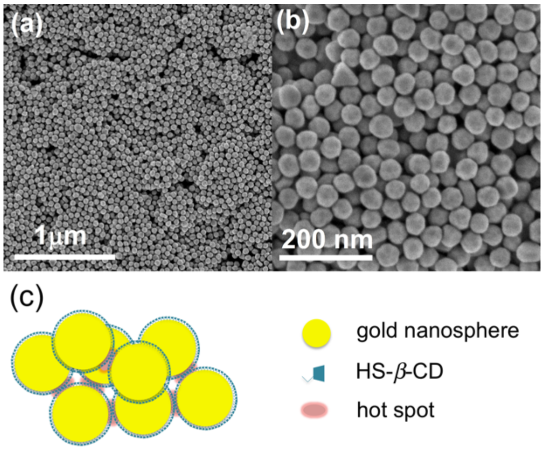

Figure 6.12. SEM images of the dried *β*-CD-functionalized gold nanosphere sample. SEM imaging was carried out at 2 kV. The magnifications are: (a) 30,000×; (b) 110,000×. (c) The illustration of the dried *β*-CD-functionalized gold nanosphere aggregate. Hot spots are formed between the adjacent nanospheres.

Figure 6.13 shows the normalized UV-visible absorbance spectrum of the *β*-CD-functionalized gold nanosphere stock solution and the normalized dark-field (DF) scattering spectrum of the dried *β*-CD-functionalized gold nanosphere sample. The spectra are normalized for convenience of comparison. The dispersed *β*-CD-functionalized nanosphere stock solution shows a LSPR peak at 534 nm. Some guest molecules can cause the nanosphere aggregation due to the interactions with *β*-CD hosts [149]; however, we did not observe the aggregation phenomenon (the LSPR peak remains at 534 nm) after adding the AcAm solution to the nanosphere stock solution, showing the AcAm does not have the linking effect to cause the nanosphere aggregation. The dried *β*-CD-functionalized nanosphere sample shows a LSPR peak at 735 nm. Since we use the 785-nm laser diode as the excitation source for the Raman measurement, the LSPR peak is not at the optimum position. Nonetheless, the large red shift of the LSPR peak is still beneficial for enhancing coupling and the Raman signal.

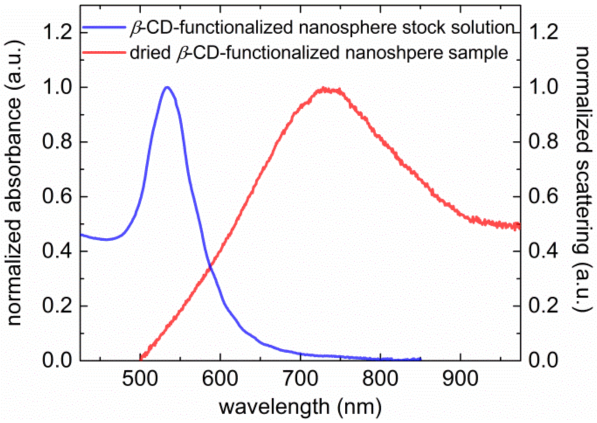

Figure 6.13. Normalized UV-visible absorbance spectrum of the *β*-CD-functionalized nanosphere stock solution and the normalized DF scattering spectrum of the dried *β*-CD-functionalized nanosphere sample. The LSPR peak has a 201-nm red shift from 534 nm to 735 nm.

Figure 6.14(a) shows the averaged Raman spectra (averaged by 16 spectra) of the sample prepared with 20 ng/mL AcAm, the blank sample without AcAm, and their difference spectrum (20 ng/mL AcAm − blank). The fluorescence background is subtracted by the spline interpolation method mentioned in section 6.1.3. The difference spectrum clearly shows the two major AcAm characteristic peaks (highlighted in green) with Raman shifts of 740 and 780 cm^{-1}, respectively. This is consistent with our previous result. Figure 6.14(b) shows the averaged Raman spectra of different AcAm concentrations around the region of the two major AcAm characteristic peaks. The peak intensity increases with the AcAm concentration. It should be noted that the blank spectrum shows a strong peak at 745 cm^{-1}, which may come from the nanosphere substrate. The background intensity is subtracted in the following quantitative analysis.

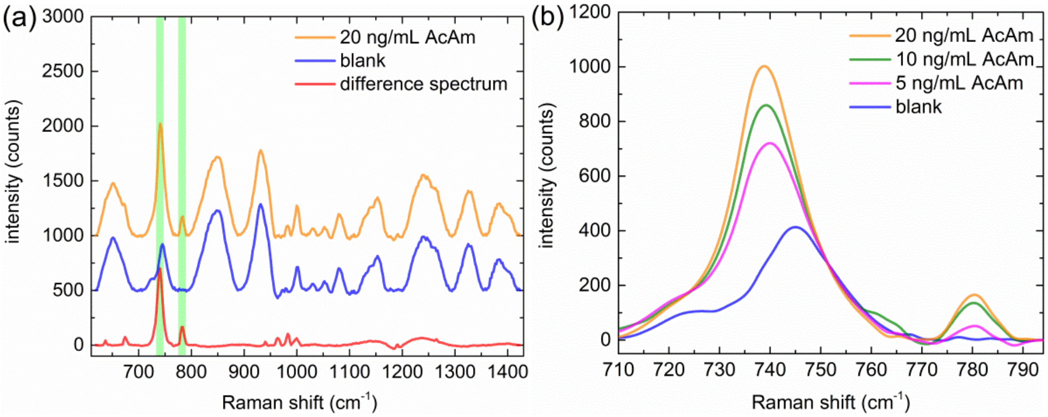

Figure 6.14. (a) Averaged Raman spectra of the sample prepared with 20 ng/mL AcAm, the blank sample without AcAm, and their difference spectrum (20 ng/mL AcAm − blank). The two major AcAm characteristic peaks (740 and 780 cm^{-1}) are highlighted in green. (b) Averaged Raman spectra of different AcAm concentrations around the region of the two major AcAm characteristic peaks.

Figure 6.15(a) shows the Raman intensity as a function of the AcAm concentration. The Raman intensity is calculated by summing the intensity values of the two major AcAm characteristic peaks. The mean background intensity has been subtracted in each concentration. The error bar of each data point stands for the standard error of the mean. The Raman intensity I_{Raman} as a function of the AcAm concentration C_{AcAm} is fitted to the Langmuir equation [150]:

$$I_{Raman} = \frac{I_{\max} K C_{AcAm}}{1 + K C_{AcAm}} \qquad (6.1)$$

in which I_{max} is the maximum Raman intensity (1306 counts) and K (0.10 mL/ng) associates with the binding constant that corresponds to the inverse of the AcAm concentration (10 ng/mL) that is required to obtain one-half of I_{max}. When $KC_{AcAm} \ll 1$, the Langmuir equation regresses to a linear form. In this case, the region of concentrations below 1 ng/mL can be approximated as the linear region. The intensity level of LOD equals three times of the standard error of the background. The detection limit of 0.4 ng/mL (indicated by the dashed line) is calculated by its intensity level and the slope of the linear fit in the approximated linear region.

Figure 6.15(b) compares the linear fits of the β-CD functionalized nanosphere platform and the β-CD-functionalized Klarite platform at low concentrations using the same quantification method. The blank data points are not shown in the logarithmic scale figure. The Klarite substrate was first immersed in the β-CD solution for surface functionalization and then immersed in the AcAm solution, followed by rinsing and drying for detection. The slope of the linear fit associates with the sensitivity of the platform. Therefore, the nanosphere platform clearly has higher sensitivity than the

Klarite platform since it has a larger intercept, which represents the slope of a line in logarithmic scale. The sensitivity of the nanosphere platform (107 counts/(ng/mL)) is 7 times higher than the Klarite platform (15 counts/(ng/mL)). The Klarite platform shows better uniformity (lower standard error). However, the detection limit of the nanosphere platform (0.4 ng/mL) is still lower than the Klarite platform (1 ng/mL) due to the large sensitivity difference.

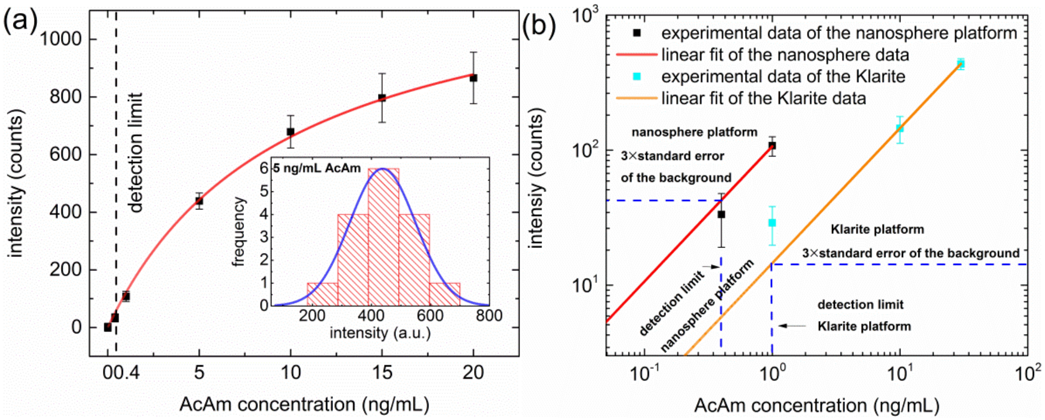

Figure 6.15. (a) Raman intensity (summed over the two major AcAm peaks) as a function of the AcAm concentration (fitted by the Langmuir equation). The detection limit of 0.4 ng/mL is indicated by the dashed line. The inset shows a representative distribution of the 16 data samples obtained in each AcAm concentration. The distribution is well-fit to the Gaussian distribution (shown by the blue curve). (b) Linear fits of the β-CD-functionalized nanosphere platform and the β-CD-functionalized Klarite platform at low concentrations.

6.4.3 Conclusion

In conclusion, we presented a method for quantifying an exogenous cancer biomarker AcAm using β-CD-functionalized gold nanospheres as a SERS substrate. We achieved a detection limit of 0.4 ng/mL. We compared the β-CD-functionalized nanosphere platform with the *β*-CD-functionalized Klarite platform. The nanosphere platform has better sensitivity (7 times higher) and estimated lower per-sample cost (1/10th) than the Klarite platform, which makes the nanosphere platform more promising for future clinical adoption.

6.5 Summary

In this chapter, we quantified an exogenous cancer biomarker AcAm using different metallic nanoparticle based SERS substrates. By investigating the commercial SERS substrates, we concluded that good SERS substrates should provide large field enhancement and high surface affinity. Following this criterion, we designed and tested polystyrene-functionalized gold nanorod and *β*-CD-functionalized gold nanosphere substrates. LODs of 16 ng/mL and 0.4 ng/mL have been achieved respectively. To further increase the sensitivity and decrease the LOD, binding agents with higher affinity to the analyte (e.g., cucurbit[n]urils [87]) can be attempted.

Chapter 7 Summary and Future Works

7.1 Summary of the Thesis

In this thesis, we developed a FWM setup to characterize the shape and size of nanoparticles by acoustic vibrations, and used nanoparticles (and other metal nanostructures) in SERS sensing applications.

For the nanoparticle characterization, we developed a FWM setup to probe nanoparticles' acoustic vibrations. The nonlinear optical response of nanoparticles is resonantly driven by the electrostriction force which couples to the acoustic vibrations of nanoparticles. Information about nanoparticles' shape, size, and size distribution can be obtained by analyzing the resonant peak position and linewidth in the FWM signal. We investigated the performance of the FWM setup on characterizing various nanoparticles (gold nanorods, silver nanoprisms, and gold nano-octahedrons) with different materials, shapes, and sizes. Information about nanoparticles' size and size distribution obtained from the FWM characterization agrees well with the scanning electron microscopic examination, showing the FWM technique's effectiveness and accuracy. We also demonstrated the in situ monitoring of gold nanoparticles' growth using FWM, indicating the FWM technique can be used as an in situ monitoring tool for colloidal growth.

For the sensing application, we demonstrated the quantification of an exogenous cancer biomarker Acetyl Amantadine using the nanoparticle-based SERS platforms. We concluded two design guidelines after exploring various commercial SERS substrates: gap structures formed between nanoparticles should be used instead of discrete nanoparticles in order to achieve higher local field enhancement; molecules should locate within the hot spots of the gap structures to experience the largest enhancement, requiring that molecules should be extracted from volume onto the metallic surface. Based on these guidelines, we developed two SERS platforms using gold nanoparticles (nanorods and nanospheres) combined with different surface functionalization techniques. We investigated the performance of these two platforms by investigating the sensitivity and limit of detection (LOD). 16 ng/mL and 0.4 ng/mL LODs have been achieved for nanorod and nanosphere platforms, respectively.

7.2 Future Works

The FWM technique opens up a new way for colloidal characterization and monitoring by probing the acoustic vibrations. However, the applications of the acoustic vibrations should not be limited in characterization. This section explores some possible future works based on nanoparticles' acoustic vibrations.

7.2.1 Intensity of the FWM Signal

For now, we mainly focus on the FWM signal's peak position and linewidth to probe the analytical properties of nanoparticles without analyzing the intensity of the FWM signal, which obviously dose not exploit the FWM signal thoroughly. It is intuitively to relate the intensity to the concentration of the colloidal solution. However, the intensity would depend on other parameters, such as nanoparticle's volume, mass, shape, elastic properties, and the ambient environment. Therefore, future investigations should separate each influential factor at a time to understand the dependency of the intensity on these factors. The concentration information of the colloidal solution could be eventually obtained from the intensity after thorough investigations on those factors.

7.2.2 Acoustic Vibrations of Nanoparticle Dimers and Trimmers

In this thesis, we mainly investigate discrete nanoparticle's acoustic vibrations. It would be interesting to investigate the acoustic vibrations of nanoparticle dimers and trimmers since new vibrational modes would appear due to the coupling. These vibrational modes may yield the information not only about the nanoparticles themselves, but also about the chemical bonds connecting them (e.g., the strength of the chemical bonds and the "spring constant" of the molecules).

7.2.3 Acoustic Vibrations of Core-Shell Nanoparticles

Core-shell nanoparticles are composite nanoparticles constructed with cores (inner materials) and shells (outer layer materials), e.g., metal nanoparticles encapsulated in a dielectric shell (e.g., $Ag@SiO_2$). The acoustic vibrational modes of these core-shell nanoparticles may differ from the bare core nanoparticles or the shell nanoparticles. These vibrational modes may be affected by the quality of the core-shell nanoparticles (e.g., the inner core nanoparticle has or has not a good mechanical contact with the outer shell layer). Analyzing these vibrational modes could provide a unique way to probe this contact in the core-shell nanoparticles.

7.2.4 Acoustic Mass Sensor

The idea of the acoustic mass sensor is that when new molecules or atoms bond to the surface of the nanoparticle, the vibrational frequency of the nanoparticle would shift due to the local density change. The shift would mainly depend on the molecules' mass or density. Ideally, the acoustic mass sensor could achieve atom-level resolution.

7.2.5 Acoustic Tunneling in Terahertz Regime

We have demonstrated the acoustic vibrations of gold nanoparticles in the terahertz regime [33]. If we can place these gold nanoparticles in a narrow metal slit (e.g., width < 10 nm), the spacing between the nanoparticles and the metal side will alternate periodically due to the oscillating deformation of the nanoparticles caused by the acoustic vibrations. Thus, we can detect the tunnel current if we apply a bias voltage across the slit. The tunnel current should oscillate at the same frequency as the nanoparticle's acoustic vibration, generating a modulation in the terahertz regime. The on and off of the tunnel current can be controlled by the driving laser, which could potentially achieve fast switching.

Appendix A

Additional Information

A.1 Statistical Results for Nanorod Samples with Aspect Ratio of 4.0 and 4.3

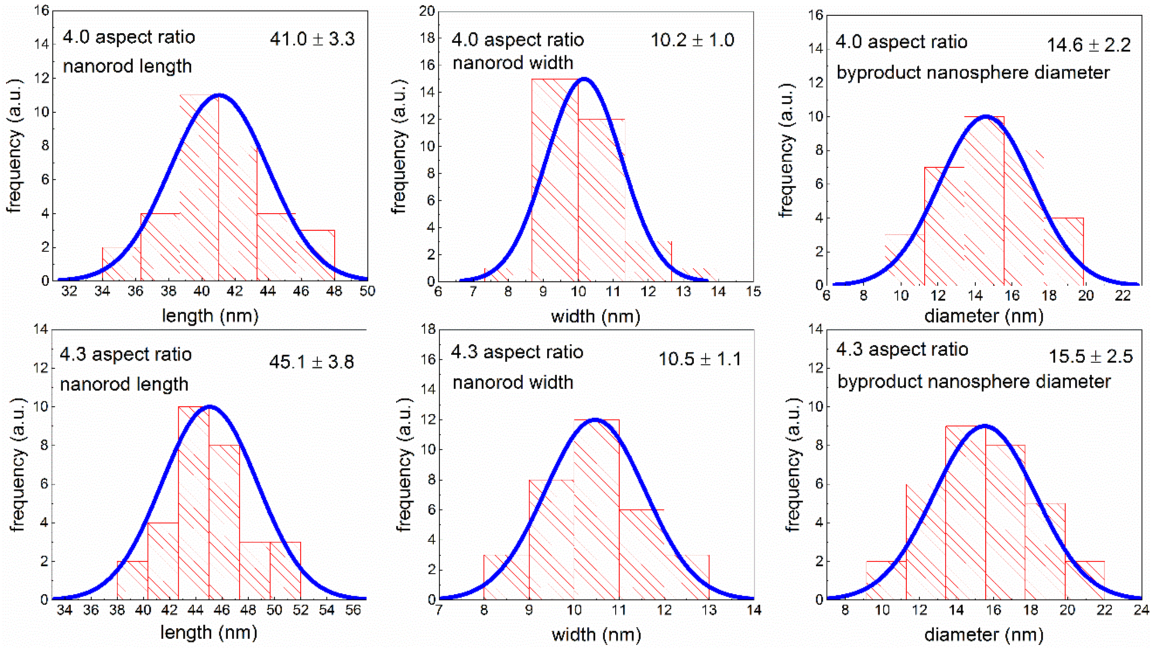

Figure A.1 Statistical results for nanorod samples with aspect ratio of 4.0 and 4.3 obtained by manually measure 32 nanorods and 32 nanospheres from the SEM images. Histograms are fitted by the Gaussian distribution. The errors represent the standard deviation.

Figure A.1 shows the statistical results for nanorod samples with aspect ratio of 4.0 and 4.3 obtained by manually measure 32 nanorods and 32 nanospheres from the SEM images. Histograms are fitted by the Gaussian distribution. The errors represent the standard deviation. These results are included in Table 3.1.

A.2 FWM Results for Nanorod Samples with Aspect Ratio of 4.0 and 4.3

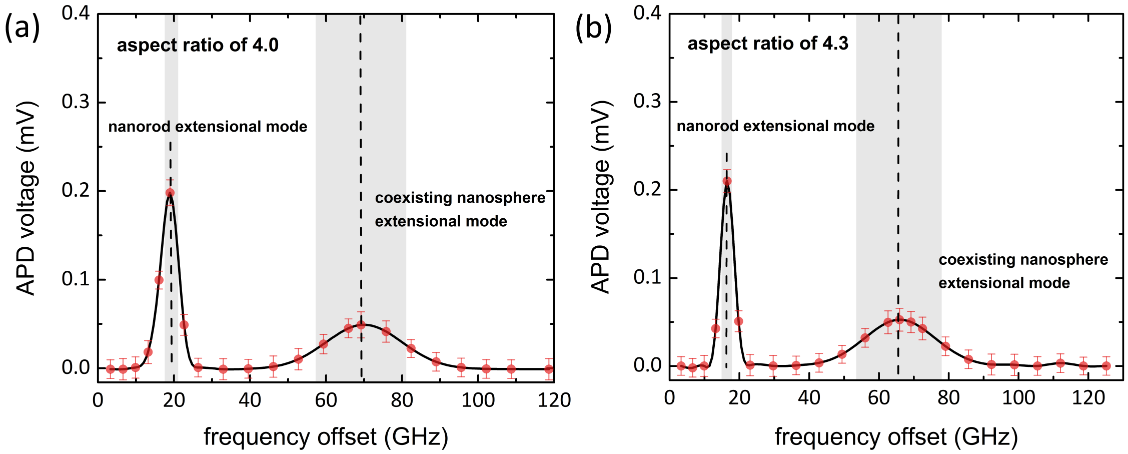

Figure A.2 FWM results for nanorod samples with aspect ratio of 4.0 (a) and 4.3 (b). For 4.0 aspect-ratio sample, the 18.9 and 69.2 GHz resonance peaks correspond to the frequencies of the extensional modes of gold nanorods and nanospheres, respectively. The dashed line indicates the calculated resonant frequencies of 18.0 and 69.6 GHz according to the SEM results. The grey area indicates the broadening (3.4 GHz for the nanorod extensional mode and 24.7 GHz for the nanosphere extensional mode) induced mainly by size distribution. For 4.3 aspect-ratio sample, the 16.5 and 65.9 GHz resonance peaks correspond to the frequencies of the extensional modes of gold nanorods and nanospheres, respectively. The dashed line indicates the calculated resonant frequencies of 16.3 and 65.6 GHz according to the SEM results. The grey area indicates the broadening (3.2 GHz for the nanorod extensional mode and 24.9 GHz for the nanosphere extensional mode) induced mainly by size distribution.

Figure A.2 shows the FWM results for nanorod samples with aspect ratio of 4.0 (a) and 4.3 (b). For 4.0 aspect-ratio sample, the 18.9 and 69.2 GHz resonance peaks correspond to the frequencies of the extensional modes of gold nanorods and nanospheres, respectively. The dashed line indicates the calculated resonant frequencies of 18.0 and 69.6 GHz according to the SEM results. The grey area indicates the broadening (3.4 GHz for the nanorod extensional mode and 24.7 GHz for the nanosphere extensional mode) induced mainly by size distribution. For 4.3 aspect-ratio sample, the 16.5 and 65.9 GHz resonance peaks correspond to the frequencies of the extensional modes of gold nanorods and nanospheres, respectively. The dashed line indicates the calculated resonant frequencies of 16.3 and 65.6 GHz according to the SEM results. The grey area indicates the broadening (3.2 GHz for the nanorod extensional mode and 24.9 GHz for the nanosphere extensional mode) induced mainly by size distribution. These results are included in Tables 3.1 and 3.2.

A.3 Publications and Contributions

1. J. Wu, D. Xiang, and R. Gordon, “Monitoring Gold Nanoparticle Growth in Situ via the Acoustic Vibrations Probed by Four-Wave Mixing,” *Analytical Chemistry*, **89**(4), 2196-2200 (2017).
2. J. Wu, D. Xiang, G Hajisalem, F. C. Lin, J. S. Huang, and R. Gordon, “Probing the acoustic vibrations of complex-shaped metal nanoparticles with four-wave mixing,” *Optics Express*, **24**(21), 23747-23754 (2016).
3. J. Wu, D. Xiang, and R. Gordon, “Characterizing gold nanorods in aqueous solution by acoustic vibrations probed with four-wave mixing,” *Optics Express*, **24**(12), 12458-12465 (2016).
4. J. Wu, W. Li, G. Hajisalem, A. Lukach, E. Kumacheva, F. Hof, and R. Gordon, “Trace cancer biomarker quantification using polystyrene-functionalized gold nanorods,” *Biomedical Optics Express*, **5**(12), 4101-4107 (2014).
5. D. Xiang, J. Wu, and R. Gordon, “Coulomb Blockade Plasmonic Switch,” *Nano Letters*, **17**(4), 2584-2588 (2017).
6. D. Xiang, J. Wu, J. Rottler, and R. Gordon, “Threshold for Terahertz Resonance of Nanoparticles in Water,” *Nano Letters*, **6**(6), 3638-3641 (2016).

Bibliography

---

[1] Lee, K.S. and El-Sayed, M.A., 2006. Gold and silver nanoparticles in sensing and imaging: sensitivity of plasmon response to size, shape, and metal composition. *The Journal of Physical Chemistry B*, **110**(39), 19220-19225.

[2] Pustovalov, V.K. and Babenko, V.A., 2004. Optical properties of gold nanoparticles at laser radiation wavelengths for laser applications in nanotechnology and medicine. *Laser physics letters*, **1**(10), 516-520.

[3] Zheng, N. and Stucky, G.D., 2006. A general synthetic strategy for oxide-supported metal nanoparticle catalysts. *Journal of the American Chemical Society*, **128**(44), 14278-14280.

[4] Atwater, H.A. and Polman, A., 2010. Plasmonics for improved photovoltaic devices. *Nature materials*, **9**(3), 205-213.

[5] Darbha, G.K., Singh, A.K., Rai, U.S., Yu, E., Yu, H. and Chandra Ray, P., 2008. Selective detection of mercury (II) ion using nonlinear optical properties of gold nanoparticles. *Journal of the American Chemical Society*, **130**(25), 8038-8043.

[6] Danckwerts, M. and Novotny, L., 2007. Optical frequency mixing at coupled gold nanoparticles. *Physical Review Letters*, **98**(2), 026104.

[7] Yu, K., Zijlstra, P., Sader, J.E., Xu, Q.H. and Orrit, M., 2013. Damping of acoustic vibrations of immobilized single gold nanorods in different environments. *Nano Letters*, **13**(6), 2710-2716.

---

[8] van Dijk, M.A., Lippitz, M. and Orrit, M., 2005. Detection of acoustic oscillations of single gold nanospheres by time-resolved interferometry. *Physical Review Letters*, **95**(26), 267406.

[9] Petrova, H., Lin, C.H., de Liejer, S., Hu, M., McLellan, J.M., Siekkinen, A.R., Wiley, B.J., Marquez, M., Xia, Y., Sader, J.E. and Hartland, G.V., 2007. Time-resolved spectroscopy of silver nanocubes: Observation and assignment of coherently excited vibrational modes. *Journal of Chemical Physics*, **126**(9), 094709.

[10] Zijlstra, P., Tchebotareva, A.L., Chon, J.W., Gu, M. and Orrit, M., 2008. Acoustic oscillations and elastic moduli of single gold nanorods. *Nano Letters*, **8**(10), 3493-3497.

[11] Hartland, G.V., Hu, M., Wilson, O., Mulvaney, P. and Sader, J.E., 2002. Coherent excitation of vibrational modes in gold nanorods. *Journal of Physical Chemistry* B, **106**(4), 743-747.

[12] Major, T.A., Lo, S.S., Yu, K. and Hartland, G.V., 2014. Time-resolved studies of the acoustic vibrational modes of metal and semiconductor nano-objects. *Journal of Physical Chemistry Letters*, **5**(5), 866-874.

[13] Hartland, G.V., 2004. Measurements of the material properties of metal nanoparticles by time-resolved spectroscopy. *Physical Chemistry Chemical Physics*, **6**(23), 5263-5274.

[14] Wheaton, S., Gelfand, R.M. and Gordon, R., 2015. Probing the Raman-active acoustic vibrations of nanoparticles with extraordinary spectral resolution. *Nature Photonics*, **9**(1), 68-72.

---

[15] Thomas, T. and Thomas, T.J., 2003. Polyamine metabolism and cancer. *Journal of Cellular and Molecular Medicine*, **7**(2), 113-126.

[16] Bras, A.P., Jänne, J., Porter, C.W. and Sitar, D.S., 2001. Spermidine/SpermineN 1-Acetyltransferase Catalyzes Amantadine Acetylation. *Drug Metabolism and Disposition*, **29**(5), 676-680.

[17] Bras, A.P., Hoff, H.R., Aoki, F.Y. and Sitar, D.S., 1998. Amantadine acetylationmay be effected by acetyltransferases other than NAT1 or NAT2. *Canadian Journal of Physiology and Pharmacology*, **76**(7-8), 701-706.

[18] Sitar, D.S., Bras, A.P., Maksymiuk, A., Pabbies, A., Brandes, L. and Blakely, B.W., 2006. PI-12. *Clinical Pharmacology & Therapeutics*, **79**(2).

[19] Sitar, D.S. and Bras, A.P., The University of Manitoba, 2004. *Method for assaying non-spermine/spermidine activity of spermidine/spermine n1-acetyltransferase (ssat)*. U.S. Patent US6811967 B2.

[20] Kneipp, K., Wang, Y., Kneipp, H., Perelman, L.T., Itzkan, I., Dasari, R.R. and Feld, M.S., 1997. Single molecule detection using surface-enhanced Raman scattering (SERS). *Physical Review Letters*, **78**(9), 1667.

[21] Shanmukh, S., Jones, L., Driskell, J., Zhao, Y., Dluhy, R. and Tripp, R.A., 2006. Rapid and sensitive detection of respiratory virus molecular signatures using a silver nanorod array SERS substrate. *Nano Letters*, **6**(11), 2630-2636.

[22] Dasary, S.S., Singh, A.K., Senapati, D., Yu, H. and Ray, P.C., 2009. Gold nanoparticle based label-free SERS probe for ultrasensitive and selective detection of trinitrotoluene. *Journal of the American Chemical Society*, **131**(38), 13806-13812.

[23] Kneipp, K. and Kneipp, H., 2006. Single molecule Raman scattering. *Applied Spectroscopy*, **60**(12), 322A.

[24] Nie, S. and Emory, S.R., 1997. Probing single molecules and single nanoparticles by surface-enhanced Raman scattering. *Science*, **275**(5303), 1102-1106.

[25] Talley, C.E., Jackson, J.B., Oubre, C., Grady, N.K., Hollars, C.W., Lane, S.M., Huser, T.R., Nordlander, P. and Halas, N.J., 2005. Surface-enhanced Raman scattering from individual Au nanoparticles and nanoparticle dimer substrates. *Nano Letters*, **5**(8), 1569-1574.

[26] Lee, S.J., Morrill, A.R. and Moskovits, M., 2006. Hot spots in silver nanowire bundles for surface-enhanced Raman spectroscopy. *Journal of the American Chemical Society*, **128**(7), 2200-2201.

[27] Wei, W.Y. and White, I.M., 2013. Inkjet-printed paper-based SERS dipsticks and swabs for trace chemical detection. *Analyst*, **138**(4), 1020-1025.

[28] Wei, W.Y. and White, I.M., 2013. Chromatographic separation and detection of target analytes from complex samples using inkjet printed SERS substrates. *Analyst*, **138**(13), 3679-3686.

[29] Wu, J., Xiang, D. and Gordon, R., 2016. Characterizing gold nanorods in aqueous solution by acoustic vibrations probed with four-wave mixing. *Optics Express*, **24**(12), 12458-12465.

[30] Wu, J., Xiang, D., Hajisalem, G., Lin, F.C., Huang, J.S., Kuo, C.H. and Gordon, R., 2016. Probing the acoustic vibrations of complex-shaped metal nanoparticles with four-wave mixing. *Optics Express*, **24**(21), 23747-23754.

---

[31] Wu, J., Xiang, D. and Gordon, R., 2017. Monitoring Gold Nanoparticle Growth in Situ via the Acoustic Vibrations Probed by Four-Wave Mixing. *Analytical Chemistry*, **89**(4), 2196-2200.

[32] Wu, J., Li, W., Hajisalem, G., Lukach, A., Kumacheva, E., Hof, F. and Gordon, R., 2014. Trace cancer biomarker quantification using polystyrene-functionalized gold nanorods. *Biomedical Optics Express*, **5**(12), 4101-4107.

[33] Xiang, D., Wu, J., Rottler, J. and Gordon, R., 2016. Threshold for Terahertz Resonance of Nanoparticles in Water. *Nano Letters*, **16**(6), 3638-3641.

[34] Xiang, D., Wu, J. and Gordon, R., 2017. Coulomb Blockade Plasmonic Switch. *Nano Letters*, **17**(4), 2584-2588.

[35] Amendola, V. and Meneghetti, M., 2009. Laser ablation synthesis in solution and size manipulation of noble metal nanoparticles. *Physical Chemistry Chemical Physics*, **11**(20), 3805-3821.

[36] Zhao, P., Li, N. and Astruc, D., 2013. State of the art in gold nanoparticle synthesis. *Coordination Chemistry Reviews*, **257**(3), 638-665.

[37] Kimling, J., Maier, M., Okenve, B., Kotaidis, V., Ballot, H. and Plech, A., 2006. Turkevich method for gold nanoparticle synthesis revisited. *Journal of Physical Chemistry B*, **110**(32), 15700-15707.

[38] Polte, J., Ahner, T.T., Delissen, F., Sokolov, S., Emmerling, F., Thünemann, A.F. and Kraehnert, R., 2010. Mechanism of gold nanoparticle formation in the classical citrate synthesis method derived from coupled in situ XANES and SAXS evaluation. *Journal of the American Chemical Society*, **132**(4), 1296-1301.

---

[39] Brown, K.R., Fox, A.P. and Natan, M.J., 1996. Morphology-dependent electrochemistry of cytochrome c at Au colloid-modified SnO2 electrodes. *Journal of the American Chemical Society*, **118**(5), 1154-1157.

[40] Slot, J.W. and Geuze, H.J., 1985. A new method of preparing gold probes for multiple-labeling cytochemistry. *European Journal of Cell Biology*, **38**(1), 87-93.

[41] Swami, A., Kumar, A. and Sastry, M., 2003. Formation of water-dispersible gold nanoparticles using a technique based on surface-bound interdigitated bilayers. *Langmuir*, **19**(4), 1168-1172.

[42] Chaikin, Y., Leader, H., Popovitz-Biro, R., Vaskevich, A. and Rubinstein, I., 2011. Versatile Scheme for the Step-by-Step Assembly of Nanoparticle Multilayers. *Langmuir*, **27**(4), 1298-1307.

[43] Zheng, Y., Zhong, X., Li, Z. and Xia, Y., 2014. Successive, Seed- Mediated Growth for the Synthesis of Single- Crystal Gold Nanospheres with Uniform Diameters Controlled in the Range of 5–150 nm. *Particle & Particle Systems Characterization,* **31**(2), 266-273.

[44] Nikoobakht, B. and El-Sayed, M.A., 2003. Preparation and growth mechanism of gold nanorods (NRs) using seed-mediated growth method. *Chemistry of Materials*, **15**(10), 1957-1962.

[45] Millstone, J.E., Hurst, S.J., Métraux, G.S., Cutler, J.I. and Mirkin, C.A., 2009. Colloidal gold and silver triangular nanoprisms. *Small*, **5**(6), 646-664.

[46] Wang, Y., Wan, D., Xie, S., Xia, X., Huang, C.Z. and Xia, Y., 2013. Synthesis of silver octahedra with controlled sizes and optical properties via seed-mediated growth. *ACS Nano*, **7**(5), 4586-4594.

---

[47] Zhang, Q., Li, W., Moran, C., Zeng, J., Chen, J., Wen, L.P. and Xia, Y., 2010. Seed-mediated synthesis of Ag nanocubes with controllable edge lengths in the range of 30− 200 nm and comparison of their optical properties. *Journal of the American Chemical Society*, **132**(32), 11372-11378.

[48] Jin, R., Cao, Y., Mirkin, C.A., Kelly, K.L., Schatz, G.C. and Zheng, J.G., 2001. Photoinduced conversion of silver nanospheres to nanoprisms. *Science*, **294**(5548), 1901-1903.

[49] Maier, S.A., 2007. *Plasmonics: fundamentals and applications*. Springer Science & Business Media.

[50] Willets, K.A. and Van Duyne, R.P., 2007. Localized surface plasmon resonance spectroscopy and sensing. *Annu. Rev. Phys. Chem.*, **58**, 267-297.

[51] Pérez- Juste, J., Liz- Marzan, L.M., Carnie, S., Chan, D.Y. and Mulvaney, P., 2004. Electric- field- directed growth of gold nanorods in aqueous surfactant solutions. *Advanced Functional Materials*, **14**(6), 571-579.

[52] Mock, J.J., Barbic, M., Smith, D.R., Schultz, D.A. and Schultz, S., 2002. Shape effects in plasmon resonance of individual colloidal silver nanoparticles. *Journal of Chemical Physics*, **116**(15), 6755-6759.

[53] Wang, F. and Shen, Y.R., 2006. General properties of local plasmons in metal nanostructures. *Physical Review Letters*, **97**(20), 206806.

[54] Jackson, J.D., 1999. *Classical electromagnetics*. J. Wiley & Sons, Inc., Singapore.

[55] Novotny, L. and Hecht, B., 2012. *Principles of nano-optics*. Cambridge university press.

[56] Johnson, P.B. and Christy, R.W., 1972. Optical constants of the noble

metals. *Physical Review B*, **6**(12), 4370.

[57] Bohren, C.F. and Huffman, D.R., 2008. *Absorption and scattering of light by small particles*. John Wiley & Sons.

[58] Kreibig, U. and Vollmer, M., 2013. *Optical properties of metal clusters (Vol. 25)*. Springer Science & Business Media.

[59] Kuwata, H., Tamaru, H., Esumi, K. and Miyano, K., 2003. Resonant light scattering from metal nanoparticles: Practical analysis beyond Rayleigh approximation. *Applied Physics Letters*, **83**(22), 4625-4627.

[60] Meier, M. and Wokaun, A., 1983. Enhanced fields on large metal particles: dynamic depolarization. *Optics Letters*, **8**(11), 581-583.

[61] Hartland, G.V., 2011. Optical studies of dynamics in noble metal nanostructures. *Chemical Reviews*, **111**(6), 3858-3887.

[62] Olson, J., Dominguez-Medina, S., Hoggard, A., Wang, L.Y., Chang, W.S. and Link, S., 2015. Optical characterization of single plasmonic nanoparticles. *Chemical Society Reviews*, **44**(1), 40-57.

[63] Sönnichsen, C., Franzl, T., Wilk, T., von Plessen, G., Feldmann, J., Wilson, O.V. and Mulvaney, P., 2002. Drastic reduction of plasmon damping in gold nanorods. *Physical Review Letters*, **88**(7), 077402.

[64] Novo, C., Gomez, D., Perez-Juste, J., Zhang, Z., Petrova, H., Reismann, M., Mulvaney, P. and Hartland, G.V., 2006. Contributions from radiation damping and surface scattering to the linewidth of the longitudinal plasmon band of gold nanorods: a single particle study. *Physical Chemistry Chemical Physics*, **8**(30), 3540-3546.

---

[65] Kraus, W.A. and Schatz, G.C., 1983. Plasmon resonance broadening in small metal particles. *The Journal of Chemical Physics*, **79**(12), 6130-6139.

[66] Zijlstra, P., Paulo, P.M., Yu, K., Xu, Q.H. and Orrit, M., 2012. Chemical Interface Damping in Single Gold Nanorods and Its Near Elimination by Tip-Specific Functionalization. *Angew. Chem. Int. Ed.,* **51**(33), 8352-8355.

[67] Haiss, W., Thanh, N.T., Aveyard, J. and Fernig, D.G., 2007. Determination of size and concentration of gold nanoparticles from UV-vis spectra. *Analytical Chemistry*, **79**(11), 4215-4221.

[68] Pandey, S., Goswami, G.K. and Nanda, K.K., 2013. Green synthesis of polysaccharide/gold nanoparticle nanocomposite: An efficient ammonia sensor. *Carbohydrate Polymers*, **94**(1), 229-234.

[69] Fenger, R., Fertitta, E., Kirmse, H., Thünemann, A.F. and Rademann, K., 2012. Size dependent catalysis with CTAB-stabilized gold nanoparticles. *Physical Chemistry Chemical Physics*, **14**(26), 9343-9349.

[70] Kanmani, P. and Lim, S.T., 2013. Synthesis and structural characterization of silver nanoparticles using bacterial exopolysaccharide and its antimicrobial activity against food and multidrug resistant pathogens. *Process Biochemistry*, **48**(7), 1099-1106.

[71] Gebregeorgis, A., Bhan, C., Wilson, O. and Raghavan, D., 2013. Characterization of silver/bovine serum albumin (Ag/BSA) nanoparticles structure: morphological, compositional, and interaction studies. *Journal of Colloid and Interface Science*, **389**(1), 31-41.

---

[72] Hu, M., Wang, X., Hartland, G.V., Mulvaney, P., Juste, J.P. and Sader, J.E., 2003. Vibrational response of nanorods to ultrafast laser induced heating: theoretical and experimental analysis. *Journal of the American Chemical Society*, **125**(48), 14925-14933.

[73] Bonacina, L., Callegari, A., Bonati, C., van Mourik, F. and Chergui, M., 2006. Time-resolved photodynamics of triangular-shaped silver nanoplates. *Nano Letters*, **6**(1), 7-10.

[74] Pelton, M., Sader, J.E., Burgin, J., Liu, M., Guyot-Sionnest, P. and Gosztola, D., 2009. Damping of acoustic vibrations in gold nanoparticles. *Nature Nanotechnology*, **4**(8), pp.492-495.

[75] Lamb, H., 1882. On the vibrations of a spherical shell. *Proceedings of the London Mathematical Society*, **1**(1), 50-56.

[76] Saviot, L., Champagnon, B., Duval, E., Kudriavtsev, I.A. and Ekimov, A.I., 1996. Size dependence of acoustic and optical vibrational modes of CdSe nanocrystals in glasses. *Journal of Non-Crystalline Solids*, **197**(2), 238-246.

[77] Lide, D.R., 2004. CRC *Handbook of Chemistry and Physics* (Vol. 85). CRC Press.

[78] Burgin, J., Langot, P., Del Fatti, N., Vallée, F., Huang, W. and El-Sayed, M.A., 2008. Time-resolved investigation of the acoustic vibration of a single gold nanoprism pair. *Journal of Physical Chemistry C*, **112**(30), 11231-11235.

[79] Haynes, C.L., McFarland, A.D., and Van Duyne, R.P., 2005. Surface-Enhanced Raman Spectroscopy. *Analytical Chemistry*, **77**(17), 338A-346A.

---

[80] Kneipp, K., Wang, Y., Kneipp, H., Perelman, L.T., Itzkan, I., Dasari, R.R. and Feld, M.S., 1997. Single molecule detection using surface-enhanced Raman scattering (SERS). *Physical Review Letters*, **78**(9), 1667.

[81] Pande, S., Ghosh, S.K., Praharaj, S., Panigrahi, S., Basu, S., Jana, S., Pal, A., Tsukuda, T. and Pal, T., 2007. Synthesis of normal and inverted gold-silver core-shell architectures in β-Cyclodextrin and their applications in SERS. *Journal of Physical Chemistry C*, **111**(29), 10806-10813.

[82] Dey, P., Blakey, I., Thurecht, K.J. and Fredericks, P.M., 2013. Self-assembled hyperbranched polymer–gold nanoparticle hybrids: understanding the effect of polymer coverage on assembly size and SERS performance. *Langmuir*, **29**(2), 525-533.

[83] Zheng, G., Polavarapu, L., Liz-Marzán, L.M., Pastoriza-Santos, I. and Pérez-Juste, J., 2015. Gold nanoparticle-loaded filter paper: a recyclable dip-catalyst for real-time reaction monitoring by surface enhanced Raman scattering. *Chemical Communications*, **51**(22), 4572-4575.

[84] Wei, W.Y. and White, I.M., 2013. Inkjet-printed paper-based SERS dipsticks and swabs for trace chemical detection. *Analyst*, **138**(4), 1020-1025.

[85] Ng, C.H.B., Yang, J. and Fan, W.Y., 2008. Synthesis and self-assembly of one-dimensional sub-10 nm Ag nanoparticles with cyclodextrin. *Journal of Physical Chemistry C*, **112**(11), 4141-4145.

[86] Taylor, R.W., Coulston, R.J., Biedermann, F., Mahajan, S., Baumberg, J.J. and Scherman, O.A., 2013. In situ SERS monitoring of photochemistry within a nanojunction reactor. *Nano Letters*, **13**(12), 5985-5990.

---

[87] Jones, S.T., Taylor, R.W., Esteban, R., Abo- Hamed, E.K., Bomans, P.H., Sommerdijk, N.A., Aizpurua, J., Baumberg, J.J. and Scherman, O.A., 2014. Gold Nanorods with Sub-Nanometer Separation using Cucurbit [n] uril for SERS Applications. *Small*, **10**(21), 4298-4303.

[88] Xu, N., Bai, B., Tan, Q. and Jin, G., 2013. Accurate geometric characterization of gold nanorod ensemble by an inverse extinction/scattering spectroscopic method. *Optics Express*, **21**(18), 21639-21650.

[89] Xu, N., Bai, B., Tan, Q. and Jin, G., 2013. Fast statistical measurement of aspect ratio distribution of gold nanorod ensembles by optical extinction spectroscopy. *Optics Express*, **21**(3), pp.2987-3000.

[90] Hu, X., Cheng, W., Wang, T., Wang, Y., Wang, E. and Dong, S., 2005. Fabrication, characterization, and application in SERS of self-assembled polyelectrolyte-gold nanorod multilayered films. *Journal of Physical Chemistry* B, **109**(41), 19385-19389.

[91] Jana, N.R., Gearheart, L. and Murphy, C.J., 2001. Wet chemical synthesis of high aspect ratio cylindrical gold nanorods. *Journal of Physical Chemistry* B, **105**(19), 4065-4067.

[92] Hu, M., Wang, X., Hartland, G.V., Mulvaney, P., Juste, J.P. and Sader, J.E., 2003. Vibrational response of nanorods to ultrafast laser induced heating: theoretical and experimental analysis. *Journal of the American Chemical Society*, **125**(48), 14925-14933.

---

[93] Ni, W., Kou, X., Yang, Z. and Wang, J., 2008. Tailoring longitudinal surface plasmon wavelengths, scattering and absorption cross sections of gold nanorods. *ACS Nano*, **2**(4), 677-686.

[94] Ruijgrok, P.V., Zijlstra, P., Tchebotareva, A.L. and Orrit, M., 2012. Damping of acoustic vibrations of single gold nanoparticles optically trapped in water. *Nano Letters*, **12**(2), 1063-1069.

[95] Tchebotareva, A.L., Ruijgrok, P.V., Zijlstra, P. and Orrit, M., 2010. Probing the acoustic vibrations of single metal nanoparticles by ultrashort laser pulses. *Laser & Photonics Reviews*, **4**(5), 581-597.

[96] Hartland, G.V., 2002. Coherent vibrational motion in metal particles: Determination of the vibrational amplitude and excitation mechanism. *Journal of Chemical Physics*, **116**(18), 8048-8055.

[97] Nelayah, J., Gu, L., Sigle, W., Koch, C.T., Pastoriza-Santos, I., Liz-Marzán, L.M. and Van Aken, P.A., 2009. Direct imaging of surface plasmon resonances on single triangular silver nanoprisms at optical wavelength using low-loss EFTEM imaging. *Optics Letters*, **34**(7), 1003-1005.

[98] Min, Q., Pang, Y., Collins, D.J., Kuklev, N.A., Gottselig, K., Steuerman, D.W. and Gordon, R., 2011. Substrate-based platform for boosting the surface-enhanced Raman of plasmonic nanoparticles. *Optics Express*, **19**(2), 1648-1655.

[99] Kulkarni, A.P., Noone, K.M., Munechika, K., Guyer, S.R. and Ginger, D.S., 2010. Plasmon-enhanced charge carrier generation in organic photovoltaic films using silver nanoprisms. *Nano Letters*, **10**(4), 1501-1505.

---

[100] Munechika, K., Chen, Y., Tillack, A.F., Kulkarni, A.P., Plante, I.J.L., Munro, A.M. and Ginger, D.S., 2010. Spectral control of plasmonic emission enhancement from quantum dots near single silver nanoprisms. *Nano Letters*, **10**(7), 2598-2603.

[101] Chen, Z., Dai, H., Liu, J., Xu, H., Li, Z., Zhou, Z.K. and Han, J.B., 2013. Dipole plasmon resonance induced large third-order optical nonlinearity of Au triangular nanoprism in infrared region. *Optics Express*, **21**(15), 17568-17575.

[102] Anker, J.N., Hall, W.P., Lyandres, O., Shah, N.C., Zhao, J. and Van Duyne, R.P., 2008. Biosensing with plasmonic nanosensors. *Nature Materials*, **7**(6), 442-453.

[103] Bloemer, M.J., Haus, J.W. and Ashley, P.R., 1990. Degenerate four-wave mixing in colloidal gold as a function of particle size. *J. Opt. Soc. Am. B*, **7**(5), 790-795.

[104] Chiu, C.Y., Chung, P.J., Lao, K.U., Liao, C.W. and Huang, M.H., 2012. Facet-dependent catalytic activity of gold nanocubes, octahedra, and rhombic dodecahedra toward 4-nitroaniline reduction. *Journal of Physical Chemistry C*, **116**(44), 23757-23763.

[105] Dreaden, E.C., Alkilany, A.M., Huang, X., Murphy, C.J. and El-Sayed, M.A., 2012. The golden age: gold nanoparticles for biomedicine. *Chemical Society Reviews*, **41**(7), 2740-2779.

[106] Cao, Z., Chen, Z. and Escoubas, L., 2014. Optical, structural, and electrical properties of PEDOT: PSS thin films doped with silver nanoprisms. *Optical Materials Express*, **4**(12), 2525-2534.

[107] Staleva, H. and Hartland, G.V., 2008. Transient absorption studies of single silver nanocubes. *Journal of Physical Chemistry C*, **112**(20), 7535-7539.

---

[108] Xiang, D. and Gordon, R., 2016. Nanoparticle Acoustic Resonance Enhanced Nearly Degenerate Four-Wave Mixing. *ACS Photonics*, **3**(8), 1421-1425.

[109] Jin, R., Cao, Y., Mirkin, C.A., Kelly, K.L., Schatz, G.C. and Zheng, J.G., 2001. Photoinduced conversion of silver nanospheres to nanoprisms. *Science*, **294**(5548), 1901-1903.

[110] Wu, H.L., Tsai, H.R., Hung, Y.T., Lao, K.U., Liao, C.W., Chung, P.J., Huang, J.S., Chen, I.C. and Huang, M.H., 2011. A comparative study of gold nanocubes, octahedra, and rhombic dodecahedra as highly sensitive SERS substrates. *Inorganic Chemistry*, **50**(17), 8106-8111.

[111] Chang, C.C., Wu, H.L., Kuo, C.H. and Huang, M.H., 2008. Hydrothermal synthesis of monodispersed octahedral gold nanocrystals with five different size ranges and their self-assembled structures. *Chemistry of Materials*, **20**(24), 7570-7574.

[112] Sherry, L.J., Jin, R., Mirkin, C.A., Schatz, G.C. and Van Duyne, R.P., 2006. Localized surface plasmon resonance spectroscopy of single silver triangular nanoprisms. *Nano Letters*, **6**(9), 2060-2065.

[113] Bonacina, L., Callegari, A., Bonati, C., van Mourik, F. and Chergui, M., 2006. Time-resolved photodynamics of triangular-shaped silver nanoplates. *Nano Letters*, **6**(1), 7-10.

[114] Li, C., Shuford, K.L., Chen, M., Lee, E.J. and Cho, S.O., 2008. A facile polyol route to uniform gold octahedra with tailorable size and their optical properties. *ACS Nano*, **2**(9), 1760-1769.

---

[115] Pan, H.H., Wang, Z.K., Lim, H.S., Ng, S.C., Zhang, V.L., Kuok, M.H., Tran, T.T. and Lu, X.M., 2011. Hypersonic confined eigenvibrations of gold nano-octahedra. *Applied Physics Letters*, **98**(13), 133123.

[116] Grzelczak, M., Pérez-Juste, J., Mulvaney, P. and Liz-Marzán, L.M., 2008. Shape control in gold nanoparticle synthesis. *Chemical Society Reviews*, **37**(9), 1783-1791.

[117] Sun, Y. and Xia, Y., 2002. Shape-controlled synthesis of gold and silver nanoparticles. *Science,* **298**(5601), 2176-2179.

[118] Tyagi, H., Kushwaha, A., Kumar, A. and Aslam, M., 2016. A Facile pH Controlled Citrate-Based Reduction Method for Gold Nanoparticle Synthesis at Room Temperature. *Nanoscale Research Letters*, **11**(1), 362.

[119] Ji, X., Song, X., Li, J., Bai, Y., Yang, W. and Peng, X., 2007. Size control of gold nanocrystals in citrate reduction: the third role of citrate. *Journal of the American Chemical Society*, **129**(45), 13939-13948.

[120] Tao, A.R., Habas, S. and Yang, P., 2008. Shape control of colloidal metal nanocrystals. *Small*, **4**(3), 310-325.

[121] Sau, T.K., Rogach, A.L., Jäckel, F., Klar, T.A. and Feldmann, J., 2010. Properties and applications of colloidal nonspherical noble metal nanoparticles. *Advanced Materials*, **22**(16), 1805-1825.

[122] Chen, S. and Kimura, K., 1999. Synthesis and characterization of carboxylate-modified gold nanoparticle powders dispersible in water. *Langmuir*, **15**(4), 1075-1082.

---

[123] Joseph, Y., Besnard, I., Rosenberger, M., Guse, B., Nothofer, H.G., Wessels, J.M., Wild, U., Knop-Gericke, A., Su, D., Schlögl, R. and Yasuda, A., 2003. Self-assembled gold nanoparticle/alkanedithiol films: preparation, electron microscopy, XPS-analysis, charge transport, and vapor-sensing properties. *Journal of Physical Chemistry B*, **107**(30), 7406-7413.

[124] Peckys, D.B. and de Jonge, N., 2011. Visualizing gold nanoparticle uptake in live cells with liquid scanning transmission electron microscopy. *Nano Letters*, **11**(4), 1733-1738.

[125] Kelly, K.L., Coronado, E., Zhao, L.L. and Schatz, G.C., 2003. The optical properties of metal nanoparticles: the influence of size, shape, and dielectric environment. *Phys. Chem. B*, **10**7, 668-677.

[126] Polte, J., Erler, R., Thunemann, A.F., Sokolov, S., Ahner, T.T., Rademann, K., Emmerling, F. and Kraehnert, R., 2010. Nucleation and growth of gold nanoparticles studied via in situ small angle X-ray scattering at millisecond time resolution. *ACS Nano*, **4**(2), 1076-1082.

[127] Leng, W., Pati, P. and Vikesland, P.J., 2015. Room temperature seed mediated growth of gold nanoparticles: mechanistic investigations and life cycle assesment. *Environ. Sci. Nano*, **2**, 440-453.

[128] Duval, E., Boukenter, A. and Champagnon, B., 1986. Vibration eigenmodes and size of microcrystallites in glass: observation by very-low-frequency Raman scattering. *Physical Review Letters*, **56**(19), 2052.

---

[129] Hodak, J.H., Henglein, A. and Hartland, G.V., 1999. Size dependent properties of Au particles: Coherent excitation and dephasing of acoustic vibrational modes. *Journal of Chemical Physics*, **111**(18), 8613-8621.

[130] Sitar, D.S., Bras, A.P., Maksymiuk, A., Cheng, K.M. and Zhou, H., "Progress in the development of SSAT1 activity as a biomarker for diagnosis of cancer," presented at the BIT Life Sciences' Annual World Cancer Congress, Beijing, 22-25 Jun. 2009.

[131] Takayama, H., Takahashi, S., Moriya, T., Osada, H., Iwabuchi, Y. and Kanoh, N., 2011. Detection of Cytochrome P450 Substrates by Using a Small-Molecule Droplet Array on an NADH- Immobilized Solid Surface. *ChemBioChem*, **12**(18), 2748-2752.

[132] Li, W., 2016. Two supramolecular methods for detecting a cancer metabolite with cucurbituril. M.Sc. Thesis, University of Victoria, Canada.

[133] Hajisalem, G., Min, Q., Gelfand, R. and Gordon, R., 2014. Effect of surface roughness on self-assembled monolayer plasmonic ruler in nonlocal regime. *Optics Express*, **22**(8), 9604-9610.

[134] Perney, N.M., Baumberg, J.J., Zoorob, M.E., Charlton, M.D., Mahnkopf, S. and Netti, C.M., 2006. Tuning localized plasmons in nanostructured substrates for surface-enhanced Raman scattering. *Optics Express*, **14**(2), 847-857.

[135] Schmidt, M.S., Hübner, J. and Boisen, A., 2012. Large area fabrication of leaning silicon nanopillars for surface enhanced Raman spectroscopy. *Advanced Materials*, **24**(10).

---

[136] Smitha, S.L., Gopchandran, K.G., Ravindran, T.R. and Prasad, V.S., 2011. Gold nanorods with finely tunable longitudinal surface plasmon resonance as SERS substrates. *Nanotechnology*, **22**(26), 265705.

[137] Nikoobakht, B., Wang, J. and El-Sayed, M.A., 2002. Surface-enhanced Raman scattering of molecules adsorbed on gold nanorods: off-surface plasmon resonance condition. *Chemical Physics Letters*, **366**(1), 17-23.

[138] Nikoobakht, B. and El-Sayed, M.A., 2003. Preparation and growth mechanism of gold nanorods (NRs) using seed-mediated growth method. *Chemistry of Materials*, **15**(10), 1957-1962.

[139] Noguez, C., 2007. Surface plasmons on metal nanoparticles: the influence of shape and physical environment. *Journal of Physical Chemistry* C, **111**(10),3806-3819.

[140] Palonpon, A.F., Ando, J., Yamakoshi, H., Dodo, K., Sodeoka, M., Kawata, S. and Fujita, K., 2013. Raman and SERS microscopy for molecular imaging of live cells. *Nature Protocols*, **8**(4), 677-692.

[141] Sato- Berrú, R.Y. and Saniger, J.M., 2006. Application of principal component analysis to discriminate the Raman spectra of functionalized multiwalled carbon nanotubes. *Journal of Raman Spectroscopy*, **37**(11), 1302-1306.

[142] Zhang, L., Li, Q., Tao, W., Yu, B. and Du, Y., 2010. Quantitative analysis of thymine with surface-enhanced Raman spectroscopy and partial least squares (PLS) regression. *Analytical and Bioanalytical Chemistry*, **398**(4), 1827-1832.

[143] Sitar, D.S., Bras, A.P., A. Maksymiuk, Cheng, K.M., and Zhou, H. “Progress in the development of SSAT1 activity as a biomarker for diagnosis of cancer,”

---

presented at the BIT Life Sciences' Annual World Cancer Congress, Beijing, 22-25 Jun. 2009.

[144] Jadzinsky, P.D., Calero, G., Ackerson, C.J., Bushnell, D.A. and Kornberg, R.D., 2007. Structure of a thiol monolayer-protected gold nanoparticle at 1.1 Å resolution. *Science*, **318**(5849), 430-433.

[145] Cao, G., Hajisalem, G., Li, W., Hof, F. and Gordon, R., 2014. Quantification of an exogenous cancer biomarker in urinalysis by Raman Spectroscopy. *Analyst*, **139**(21), 5375-5378.

[146] Wang, H.H., Liu, C.Y., Wu, S.B., Liu, N.W., Peng, C.Y., Chan, T.H., Hsu, C.F., Wang, J.K. and Wang, Y.L., 2006. Highly Raman-enhancing substrates based on silver nanoparticle arrays with tunable sub-10 nm gaps. *Advanced Materials*, **18**(4), 491-495.

[147] Alexander KD, Hampton MJ, Zhang S, Dhawan A, Xu H, Lopez R., 2009. A high-throughput method for controlled hot-spot fabrication in SERS-active gold nanoparticle dimer arrays. *Journal of Raman Spectroscopy*, **40**(12), 2171-5.

[148] Prado, A.R., Oliveira, J.P., Pereira, R.H., Guimarães, M.C., Nogueira, B.V., Castro, E.V., Almeida, L.C., Ribeiro, M.R. and Pontes, M.J., 2015. Surface-Enhanced Raman Plasmon in Self-Assembled Sulfide-Coated Gold Nanoparticle Arrays. *Plasmonics*, **10**(5), 1097-1103.

[149] Liu, J., Mendoza, S., Román, E., Lynn, M.J., Xu, R. and Kaifer, A.E., 1999. Cyclodextrin-modified gold nanospheres. Host-guest interactions at work to control colloidal properties. *Journal of the American Chemical Society*, **121**(17), 4304-4305.

---

[150] Brewer, S.H., Glomm, W.R., Johnson, M.C., Knag, M.K. and Franzen, S., 2005. Probing BSA binding to citrate-coated gold nanoparticles and surfaces. *Langmuir*, **21**(20), 9303-9307.